UNIVERSITÀ
DEGLI STUDI
DI PADOVA

Sede amministrativa: *Università degli Studi di Padova*

CISAS - Centro d'Ateneo di Studi e Attività Spaziali "G. Colombo"

CORSO DI DOTTORATO DI RICERCA IN: Scienze Tecnologie e Misure Spaziali (STMS)

CURRICOLO: Misure Meccaniche per l'Ingegneria e lo Spazio (MMIS)

CICLO: XXXII

Development of a quantitative measurement procedure for defect size and morphological characterization in composite materials by Shearography

Coordinatore del Corso: *Ch.mo Prof. Giampiero Naletto*
Supervisore: *Ch.mo Prof. Gianluca Rossi*

Dottorando: *Gloria Allevi*

Measure the measurable,
and make measurable what is not so.

— Galileo Galilei

To my friends.

Abstract

In the last decades, new materials and solutions were deeply studied in the field of aerospace industry in order to reach important objectives such as weight reduction of structures, reliability, durability, cost efficiency and mechanical strength. In this scenario, composite materials play a very important role, since they are supposed to provide all the mentioned requirements. Other solutions, such as Additive Manufactured components are increasingly under investigation since they are considered capable of reaching these objectives too, despite the still lack of standards. Both composite and Additive Manufactured materials used for aerospace industry must comply with the sector's stringent acceptability requirements and, for this purpose, the study of suitable Non-Destructive-Testing (NDT) procedures is crucial. In this dissertation, the focus is mainly put on composite materials inspection by using an optical, interferometric technique, called Shearography, being a highly sensitive Non-Destructive method whose main application is defect and damage detection in composite materials, in fact. Despite its high potential, the use of Shearography is still qualitative, meaning that the user is only capable of stating if a defect is present or if it is not (a very little attention is paid to its size and morphology), by observing typical interference fringes appearing in case of defect. This phenomenon is due to the fact that Shearography measures the first derivative of the out-of-plane displacement of an observed surface, by considering variations in the phase relation between separated points of the surface itself. Consequently, a fringe pattern, i.e. a variation in the phase relation between these points is detected if, and only if, a differential deformation occurs between different regions of the surface. This is exactly what happens when a structure is damaged: the defect region of influence will be more warped with respect to the rest of the structure, making fringes appear. Therefore, the need of observing deformations implies the inspected structure to be loaded. Typically, three kinds

of load can be exploited for Shearography inspection: mechanical load, vacuum load and thermal load. Of course, mechanical and vacuum load provide a higher level of repeatability with respect to thermal one, but they cannot be considered completely Non-Invasive and require a higher complexity in the measurement setup. On the other hand, thermal load is much easier to set up (typically one or two halogen lamps are exploited to heat the structure), but it implies a series of effects difficult to forecast and/or simulate, such as environmental absorption, air turbulence, propagation of the radiation inside the material in cases where material properties are unknown, etc. For all these reasons, no standard procedures were given even now, especially for thermal load applications. In addition, Shearography performances and results are highly dependent on measurement conditions and parameters themselves. In particular, the first influencer parameter is the shear distance, i.e. the distance between points used for evaluating phase relations, determining the system sensitivity and resolution. The second one is the distance between the inspected surface and the Shearocamera, affecting spatial resolution, and increasing or decreasing environmental effects on thermal radiation, in case of thermal load, of course. The third one is the load to apply to the structure: the higher the load, the more warped the defect, the higher the overestimation of its size. On the other hand, the lower the load, the lower the Signal-to-Noise Ratio (SNR), the less precise the measurement. Other influencer conditions are the defect characteristics themselves, being the defect depth and size, whose combination affects the needed load to make defect sufficiently visible and the sensitivity required (i.e. the shear amount) for the same purpose. Therefore, the aim of this work is to provide a deep study of Shearography technique in order to overcome its two great limits, i.e. the lack of algorithms capable of accurately determining defect size and morphology, and the lack of a repeatable procedure for thermal load applications to be carried out by any operator, giving as output both the actual defect size and the optimal shear distance for given defect size, observation distance, defect depth. The first goal was reached by designing an algorithm that studies the phase maps by a hybrid method involving both image analysis tools and signal processing ones. This was fundamental since it was demonstrated that analyzing the phase maps only by standard image processing methods for morphological study, i.e. filters, automatic thresholds, erosion and dilatation operations, does not lead to good quantitative estimations neither for simple nor for complex damages. Consequently,

a series of phase profiles to be treated as pure signals are extracted each time a phase map has to be processed. At this point, the defect shape is reconstructed by localizing the boundaries of each phase profile. This was obtained by the use of Wavelet Transform method for singularity estimation, in addition with another function, called Structural Intensity, that enables to select only the dominant singularities actually corresponding to the searched boundaries, discarding all the noise-generated ones. Finally, the second goal was achieved by two different steps. At first, a synchronized and automatic test bench was designed and prototyped, making the acquisition repeatable and reducing uncertainty sources like turbulence occurring after lamps switch-off. This effect was avoided by adding a proper structure to the measurement setup, able to screen lamps after their switch-off. From this moment, the software starts the acquisition of phase maps, storing the cooling phase as well. The acquisition process is then repeated for different combinations of measurement parameters. The second step lies in the elaboration of all the acquired data defining, for example, criteria for choosing the right load step. Furthermore, results of all combinations are matched together showing a parabola, whose vertex gives information about defect size and optimum shear distance for the given case. This procedure can be implemented either on a test panel of a specific material in order to have an idea about optimal conditions for given defect size and depth, or it can be carried out each time an inspection has to take place, in order to avoid errors generated by differences between the test panel and the actual structure to inspect.

Sommario

Negli ultimi decenni sono stati studiati nuovi materiali e soluzioni nel settore dell' industria aerospaziale al fine di raggiungere importanti obiettivi come la riduzione del peso delle strutture, elevata affidabilità, durata, efficienza dei costi e resistenza meccanica. In questo scenario, i materiali compositi svolgono un ruolo molto importante, essendo stati sviluppati per fornire tutti i requisiti menzionati. Altre soluzioni, come componenti realizzati in manifattura additiva, sono sempre più sotto inchiesta poiché anch'essi considerati in grado di raggiungere questi obiettivi, nonostante la attuale mancanza di standard. I materiali compositi e realizzati in manifattura additiva utilizzati per l'industria aerospaziale devono rispettare gli stringenti requisiti di accettabilità del settore e, per questo scopo, lo studio di idonee procedure di test non distruttivi (NDT) è cruciale. In questa tesi, l'attenzione si concentra principalmente sull'ispezione dei materiali compositi mediante una tecnica ottica e interferometrica, chiamata Shearografia, un metodo caratterizzato da alta sensibilità e non distruttivo, il cui principale campo di applicazione è proprio il rilevamento di difetti e/on danneggiamenti in materiali compositi. Nonostante il suo elevato potenziale, l'utilizzo della Shearografia è ancora oggi qualitativo, il che significa che l'utente è solo in grado di affermare se è presente un difetto o se non lo è (viene prestata poca attenzione al rilevamento delle sue dimensioni e della sua morfologia), osservando le tipiche frange di interferenza che appaiono, appunto, in presenza di un difetto. Questo fenomeno è dovuto al fatto che la Shearografia misura la derivata prima dello spostamento fuori dal piano di una superficie osservata, considerando variazioni nella relazione di fase tra diversi punti, separati da una certa distanza, della superficie stessa. Di conseguenza, una distribuzione di frange, cioè una variazione nella relazione di fase tra questi punti viene rilevato se, e solo se, si verifica una deformazione differenziale tra regioni diverse della superficie. Questo è esattamente ciò che accade quando una struttura è danneggiata: la

regione di influenza del difetto sarà più deformata rispetto al resto della struttura, causando l'insorgenza di frange di interferenza. Pertanto, la necessità di osservare deformazioni implica che la struttura ispezionata debba essere in qualche modo sollecitata. In genere, tre tipi di carico possono essere sfruttati per l'ispezione mediante Shearografia: carico meccanico, vuoto e carico termico. Naturalmente, il carico meccanico e il vuoto forniscono un livello superiore di ripetibilità rispetto a quello termico, ma non possono essere considerati completamente non invasivi e richiedono una maggiore complessità del setup di misura. D'altra parte, il carico termico è molto più semplice da realizzare (in genere una o due lampade alogene sono sfruttate per riscaldare la struttura), ma implica una serie di effetti difficili da prevedere e/o simulare, come l'assorbimento ambientale, turbolenze, propagazione della radiazione all'interno del materiale nei casi in cui le proprietà del materiale non siano note, ecc. Per tutti questi motivi, non esistono ad oggi procedure standard, specialmente per applicazioni che coinvolgano il carico termico. Inoltre, le prestazioni ed i risultati della Shearografia dipendono fortemente dalle condizioni e dai parametri di misura stessi. In particolare, il primo parametro condizionante è la distanza di shear, ovvero la distanza tra i punti utilizzati per valutare le relazioni di fase, che determina la sensibilità e la risoluzione del sistema. Il secondo parametro è la distanza tra la superficie ispezionata e la Shearocamera, che determina la risoluzione spaziale e l'entità degli effetti ambientali sulle radiazioni termiche, in caso di carico termico. Il terzo è il carico da applicare alla struttura: maggiore è il carico, più deformato è il difetto, maggiore è la probabilità di sovrastimarne le dimensioni. D'altra parte, più basso è il carico, più basso è il rapporto segnale-rumore (SNR), meno precisa è la misurazione. Altre condizioni che influenzano la misura sono le caratteristiche stesse del difetto, quali la profondità e la dimensione del difetto, la cui combinazione determina la richiesta di carico necessario per rendere sufficientemente visibile il difetto, e la sensibilità necessaria (ossia la distanza di shear) per lo stesso scopo. Pertanto, l'obiettivo di questo lavoro è quello di fornire uno studio approfondito della tecnica Shearografica al fine di superare i suoi due grandi limiti: la mancanza di algoritmi in grado di determinare con precisione la dimensione del difetto e la sua morfologia, e la mancanza di una procedura ripetibile per le applicazioni di carico termico che possa essere eseguita da qualsiasi operatore, fornendo in uscita sia la dimensione effettiva del difetto, sia la distanza di shear ottimale per date dimensioni del difetto, distanza di osservazione,

profondità del difetto. Il primo obiettivo è stato raggiunto progettando un algoritmo che studiasse le mappe di fase con un metodo ibrido, che coinvolgesse cioè sia strumenti di analisi delle immagini, sia strumenti di elaborazione del segnale. Ciò è stato fondamentale poiché è stato dimostrato che l'analisi delle mappe di fase realizzata esclusivamente con metodi standard di elaborazione delle immagini per l'analisi morfologica, vale a dire filtri, soglie automatiche, operazioni di erosione e dilatazione, non risulta affidabile per analisi quantitative né su difetti semplici né su difetti complessi. Di conseguenza, una serie di profili di fase da analizzare come segnali puri viene estratta ogni volta che una mappa di fase deve essere elaborata. A questo punto, viene ricostruita la forma del difetto localizzando i bordi di ciascun profilo di fase. Questo è stato ottenuto tramite il metodo della Wavelet Transform per la stima delle singolarità, utilizzato in combinazione ad un altra funzione, denominata Intensità Strutturale, che consente di selezionare solo le singolarità dominanti che corrispondano effettivamente ai confini cercati, scartando tutte quelle generate dal rumore di fondo. Infine, il secondo obiettivo è stato raggiunto con due diversi passaggi. Inizialmente, è stato progettato e prototipato un banco di prova sincronizzato e automatico, in modo da rendere ripetibile l'acquisizione e ridurre le fonti di incertezza come le turbolenze che si verificano dopo lo spegnimento delle lampade. Questo effetto è stato evitato aggiungendo una apposita struttura al setup di misura usuale, in grado di schermare le lampade dopo il loro spegnimento. Da questo momento, il software avvia l'acquisizione e il salvataggio delle mappe di fase durante la fase di raffreddamento successiva all'applicazione del carico termico. Il processo di acquisizione viene quindi ripetuto per diverse combinazioni di parametri di misura. Il secondo passaggio prevede, invece, l'elaborazione di tutti i dati acquisiti che definiscono, ad esempio, i criteri per la scelta del carico. Alla fine, i risultati di tutte le combinazioni vengono uniti e comparati, mostrando un comportamento parabolico al variare della distanza di shear. Il vertice di tale parabola fornirà dunque informazioni sulla dimensione del difetto e sullo shear ottimale per l'ispezione corrente. Questa procedura può essere o implementata su un pannello campione dello stesso materiale della struttura che dovrà poi essere ispezionata (in modo da avere un'idea delle condizioni ottimali per data dimensione e profondità del difetto), oppure può essere eseguita ogni volta che è necessario un controllo su un componente, al fine di evitare errori generati dalle differenze tra il pannello campione e la reale struttura da ispezionare.

Contents

List of Figures

List of Tables

Chapter 1

Introduction

In recent years, composite materials are increasingly gaining ground as chosen structural materials for construction of aircrafts and spacecrafts. In fact, they are proving to be suitable to meet the principal requirements of aerospace industry, that can be classified in [1]:

- light weight due to high specific strength and stiffness;
- high reliability;
- aerodynamic performances;
- multi-role or functionality;
- suitability for all-weather operations;
- fatigue and corrosion resistance;
- high static strength: some parts of the structures, for example aircraft wings, should be resistant to extreme forces due to wind shear and other high transient forces;
- high fracture toughness and damage [2];
- high-impact energy to resist against sudden impacts of various types (bird strikes, foreign objects, etc.) [2];

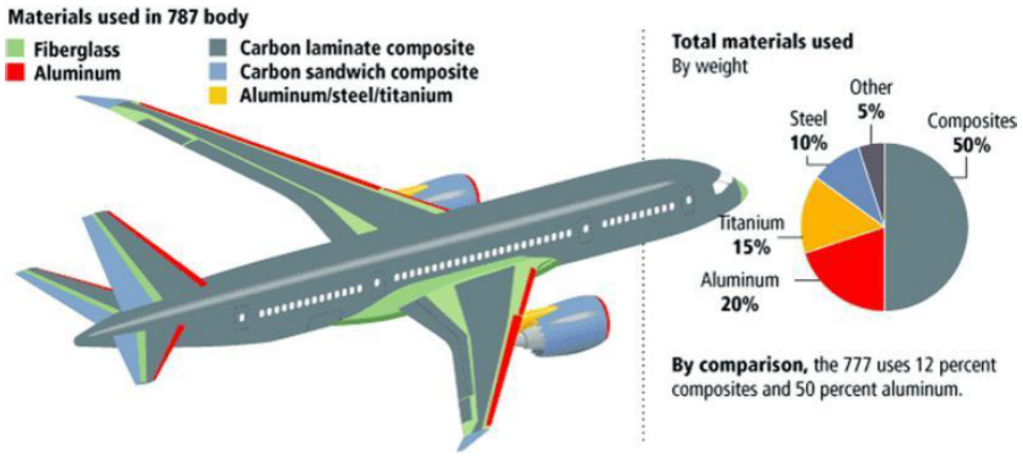

Figure 1.1: Composite parts in Boeing 787

- capability of high level of optimization: tailoring the directional strength and stiffness;
- capability of maintaining dimensional and alignment stability in space environment.

In this scenario, the term *advanced aerospace composites* refers to materials obtained by binding high-strength and high-stiffness continuous fibers with various types of polymeric resins and consolidating the resulting bi-material (composite) into finished parts under a predescribed cycle of temperature and pressure [3]. In Fig. 1.1 it is possible to note that the 50% of Boeing 787 is made by using composite parts, demonstrating those materials to have the above mentioned skills. Even in space applications composite components are largely exploited: Fig. 1.2 shows, for example, the main stages of the VEGA launcher, where upper stage, interstage section, fairing and adapter are composite-made. This confirms the suitability of these kind of materials to withstand even harsh environmental conditions. In [2], [4] and [5] the main types of advanced composites for aerospace engineering are described. Here they will be briefly summarized in order to just have an idea of the classification:

1. Laminated composites: fabricated by assembling a number of fibrous layers, arrangeable in various orientations with respect to the axis of the composites,

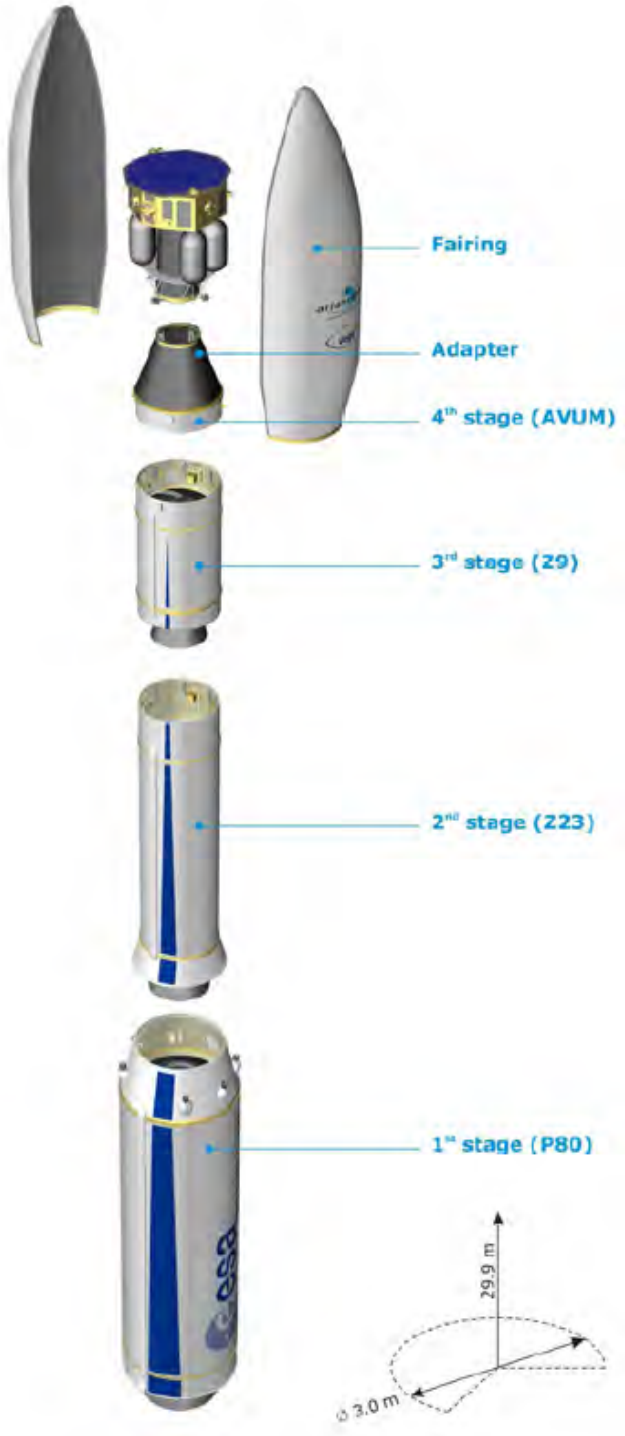

Figure 1.2: Principal stages of Vega launcher. Composite parts are: upper stage, inter-stage section, fairing and adapter.

and combing them with the matrix materials. In this way, their in-plane properties can be tailored in different directions.

2. Sandwich composites: fabricated by combining two thin and strong skins with thick and light-weight core materials. Generally, the faces are high strength composites bonded to different types of core materials (honeycombs, balsa wood, foams, etc.) using adhesives. With respect to laminate composites, sandwich ones present various advantages in terms of: light weight, high bending stiffness, thermal insulation, noise insulation, vibration damping.

3. Braided composites: braided structures are produced by intertwining two or more yarns and are distinguished from other fibrous architectures by the yarns aligned diagonally to the structure axis [2].

4. Auxetic composites: they possess a negative Poisson's ratio, thus providing the following advantages: high shear modulus,synclastic curvature, high damping resistance, high fracture toughness, enhanced crack growth resistance and high energy absorption capability [2].

However, the choice of using these materials must face some weaknesses, such as [1]:

- laminated structures may have weak interfaces and delaminations causing poor resistance to out-of-plane tensile loads;
- debondings in sandwich structures;
- susceptibility to impact damage and strong possibility of internal damage going unnoticed;
- moisture absorption and consequent degradation of high temperature performances;
- multiplicity of possible manufacturing defects.

In order to control and to limit the mentioned weaknesses, a deep analysis must be conducted starting from the design phase with the very choice of the composite constituents and processing of the basic building block, often in the form of preimpregnated layers of fibers in polymeric resin, commonly referred to as prepregs

[3]. The consolidation of parts and structures from such basic building blocks, known as cure cycle, requires another careful quality control aiming to ensure that the final product meets the strict quality requisites for its intended use [3]. The entire quality control process must take into account the cumulative effects of the various raw materials' processing phases on the quality of the final product. For this purpose, both destructive and nondestructive tests are conducted at various stages of the qualification process. In [3] the principal quality control procedures defined by the standards provided by the American Society for Testing and Materials (ASTM) are summarized in:

- constituent materials control;
- resins quality control;
- fibers quality control;
- prepregs quality control;
- procured materials control.

In addition, monitoring procedures of the manufacturing process itself are usually performed, such as:

- cure monitoring;
- post-cure verification.

At the end, the inspection of the final product is performed by means of Destructive and/or Non-Destructive Tests. For the first category, it is worth to mention: micro structural examination, usually performed by Scanning Electron Microscopy (SEM) and Mechanical Testing [3]. On the other hand, for the second group it is possible to find: liquid penetrant methods, Ultrasonic techniques, Infrared Thermography, Laser-Ultrasonics techniques and Shearography. These control techniques and procedures are crucial since one of the main problem of composite materials is the limited information about the behavior of composite air frame structures due to less experience on composite air frames as compared to metallic designs. Composite materials are, in fact, anisotropic, inhomogeneous and may deal with different fabrication and working methods, requiring new and complicated analysis tools

[1]. However, their behavior is not always predictable by computer technology and analysis methods, thus the need of performing reliable quality control procedures. This work is then contextualized in this scenario, putting the focus on one of the mentioned Non-Destructive Techniques for aerospace composites inspection: Shearography.

Shearography is a highly sensitive interferometric technique, measuring the first derivative of the out-of-plane displacement of an inspected, loaded, object surface, illuminated by a coherent light, usually produced by laser diodes. It is capable of detecting superficial and sub-superficial defects, approximately up to 5 mm depth, by exploiting the difference of deformation patterns occurring between a damaged region and the rest of the structure. This information is stored as variation in the phase relation of the back scattered light between points of the object surface, separated by a quantity called *shear*. The variation in the phase relation can be successively related to the first derivative of the out-of-plane displacement by means of the shear amount itself and the wavelength of the coherent light illuminating the surface. Since the interferometric effect between points is exploited, a fringe pattern typically called *butterfly pattern* appears in case of defects. Therefore, Shearography is able to detect a great part of the above mentioned weaknesses that may be present in a composite structure, such as:

- delaminations;
- debondings;
- impact damages.

However, Shearography is still generally used as a qualitative method, with the only aim of stating if the structure is damaged or not. Actually, in order to comply with aerospace industry's stringent acceptability requirements, attention should be paid even to defect size and morphology but, in this regard, no algorithm can be found up to now in literature. In addition to this, the lack of standard procedures and precise indications about the measurement setup and procedures themselves, contributes to make Shearography far from being a quantitative method capable to comply with the discussed requisites. This Ph.D. thesis aims at overcoming this two limits both by providing a suitable algorithm for defect size estimation and morphological reconstruction, and a repeatable procedure for applications where

thermal load is used to load the structure. In addition to this, a further code was developed to be used in conjunction with the first one, in order to process the data outcoming from the procedure for determining the actual defect size corresponding to the optimal measurement parameters. This is necessary because the resulting defect size is influenced by measurement conditions, as:

1. Shear amount: it changes the instrument sensitivity and the resolution in the deformation estimation.

2. Distance of observation: it changes the spatial resolution and has an effect on turbulence phenomena produced by the heating radiation.

3. Applied load: the higher the load, the more warped the defect, the higher its overestimation. On the contrary, the smaller the load, the lower the Signal to Noise Ratio, the less reliable the results. Criteria for choosing the right load intensity must be provided.

4. Defect depth: the inner the defect, the lower the difference between the defect deformation and the background deformation, the lower the Signal to Noise Ratio.

5. Defect size: the smaller the defect, the lower the difference between the defect deformation and the background deformation, the lower the Signal to Noise Ratio.

The main idea is then to implement a procedure where different load steps are imposed to the structure, whose cooling phase is successively stored in the form of phase maps. This is successively repeated for different shearing amounts and, if needed, for different observation distances. The developed code processes results and combines those obtained for each variables combination, describing a parabola whose vertex corresponds to the actual defect size and the optimal shear amount for given observation distance and defect.

Chapter 2

Shearography: theoretical background

2.1 Speckle Patterns

A Speckle Pattern is a random intensity distribution that is formed when fairly coherent light is either reflected from a rough surface or propagates through a medium with random refractive index fluctuations. Such patterns are easily visible even to the casual observer when highly coherent laser light is used. In general the statistical properties of the speckle patterns depend both on the coherence of the incident light and the detailed properties of the random surface or medium, although for perfect coherent light this dependence on the random scatterer is almost negligible if the scatterer introduces path differences greater than one wavelength [6].

2.1.1 Speckle pattern phenomenon

The earliest observation of the phenomenon of speckling appears to have been by Exner in 1877 [8], in connection with a study of the Fraunhofer rings formed when a beam of coherent light is diffracted by a number of particles of the same size distributed at random. With a sufficiently high magnification, using white light, the central aureole was found to exhibit a fibrous, radial structure, while with a red filter this was replaced by a fine granular structure (Fig. 2.1). Exner pointed

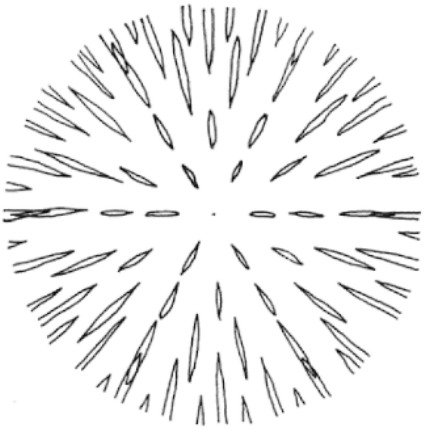

Figure 2.1: Exner's sketch of the radial granular structure in white light [7]

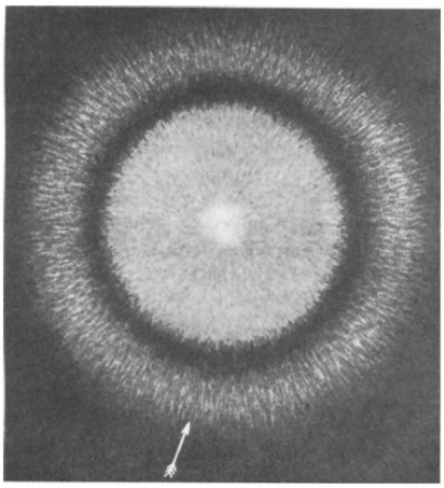

Figure 2.2: Diffraction pattern produced by a glass plate covered with lycopodium powder [7].

out that earlier statements according to which the superimposition of a very large number of identical wavetrains with random phase differences would give rise to a constant illumination were wrong, and it must lead to strong local fluctuations in intensity. Nearly forty years later in 1914 von Laue published a photograph of Fraunhofer rings obtained from a plate covered with lycopodium powder which clearly shows the radially granular structure noted by Exner (Fig. 2.2). Exner attributed the radial nature of the pattern to the fact that the light source was not very monochromatic, and this was later confirmed [6]. Another experiment carried out later to show that the fibrous radial structure was only due to dispersion effects, consisted in observing the pattern through a prism. The original radial structure was then replaced by a granular structure at a point at some distance from its center, where the dispersion due to the prism canceled that due to the diffraction. Some years later, by using strictly monochromatic light ($\lambda = 0.426$ μm), photographs of the diffraction pattern showed only a granular structure up to the second diffraction ring, with no trace of a radial structure. One of the first applications of such a speckle pattern was described by Raman [9], dealing with a very simple demonstration of Brownian movement, based on the fact that movements of the diffracting particles, if sufficiently small and slow, would result in changes in the appearance of the pattern which could be followed visually [10]. In 1962 it was noticed that the Laser Speckle granularity was an interference effect where the speckle size and shape were correlated to the size and shape of the viewing aperture. Approximately during the same period holography was realized to be able to be a powerful instrument for studying object vibration and displacements [7]. Hence, speckle techniques evolved when speckle patterns were compared in order to obtain, again, information about object's vibration and displacements, but at first they did not offer any advantages over holographic interferometry: actually these methods were highly affected by noisy fringes. Only the advent of electronic processing gave the speckle techniques an advantage over holographic interferometry, since it enabled the real-time generation of whole-field speckle interferograms [7]. Now, as it was already mentioned, when a diffusely reflecting (or transmitting) object in laser light, its image has a granular appearance. Hence, it appears covered with a fine, randomly distributed light and dark speckles. If the object moves, the speckle twinkles and moves relative to the object. This phenomenon of speckle is inherent when using highly coherent light. At an observation point in space, the

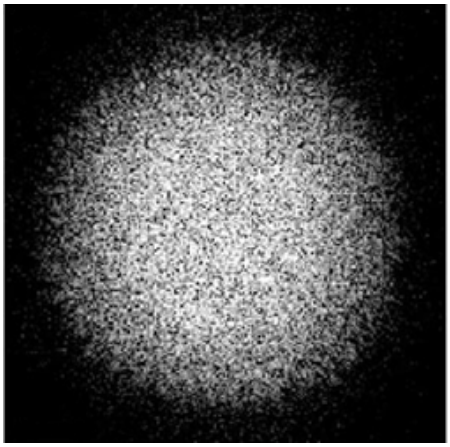

Figure 2.3: Typical Speckle Pattern

complex amplitudes, which scatter toward the point from all illuminated points on an object, interferometrically superimpose to form the intensity and phase at that point. Such a resulting interference pattern in space is called a speckle pattern (Fig. 2.3). Laser speckle existing in free space is known as objective speckle, while when an imaging system is used to observe speckle, the result is a subjective speckle, whose size is related to the viewing aperture, rather than an objective speckle pattern. Subjective speckle is formed by the superimposition of point spread function complex amplitudes at the image plane. Each point of the image plane registers only light beams that are reflected by a small part of the object surface. Therefore, they depend on the scattered light collected by the image aperture, and the speckle size is determined by the spatial frequencies passed through the lens system. An observer who looks at the object's surface perceives the subjective speckle effect because the human eye has similar aperture and lens optics [7].

2.1.2 Exploitation of Speckle Noise

In general,the presence of speckle in an interferogram reduces the ability of the human eye to resolve fine details. This is the reason why speckle reduction has been an important issue in the past decades. By adding together on an intensity basis many statistically independent speckle patterns, the S/N ratio of speckled images can be significantly increased [7]. Statistically independent speckle patterns are generated by changing the angle of illumination, the wavelength of the light,

or the polarization of the object's illumination [7]. Since speckle changes intensity and phase when an object is deformed, the correlation of speckle patterns is either experimentally implicit or statistically explicit. In the first case, the speckle patterns before and after loading coincide completely and exactly except for the change in intensity and phase for producing macroscopic fringes, and the implicity is the main result of the investigations [7]. If the overlapping of the speckle patterns is insufficient, no fringes are visible. Let's now consider the intensity expression of an interference pattern. When two partial waves emitted by a same source, but with different amplitudes a_1, a_2 and phase θ_1 and θ_2, are brought together at the exit of an interferometer, the interference effect occurs and the total light field at the position (x, y) can be described as a linear superimposition of the two waves:

$$U_{tot} = U_1(x, y) + U_2(x, y) \tag{2.1}$$

where

$$\begin{cases} U_1(x, y) = a_1(x, y)e^{i\theta_1(x,y)} \\ U_2(x, y) = a_2(x, y)e^{i\theta_2(x,y)} \end{cases} \tag{2.2}$$

The observed intensity of the interferogram is defined as a product of U_{tot} and its conjugate U^*_{tot} :

$$I = U_{tot} \times U^*_{tot} \tag{2.3}$$

By inserting Equations 2.1, 2.2 and 2.3, the intensity expression will be:

$$I = [a_1(x, y)]^2 + [a_2(x, y)]^2 + 2a_1(x, y)a_2(x, y)\cos\theta_1(x, y) - \theta_2(x, y)] \tag{2.4}$$

Let $\Phi(x, y) = \theta_1(x, y) - \theta_2(x, y)$ be the phase difference between the two waves and $I_1(x, y) = [a_1(x, y)]^2$, $I_2(x, y) = [a_2(x, y)]^2$ be the intensities of light waves 1 and 2. Then, Equation 2.4 will become:

$$I = I_1(x, y) + I_2(x, y) + 2\sqrt{I_1(x, y)I_2(x, y)}\cos\Phi(x, y). \tag{2.5}$$

When the object is deformed, one will have Equation 2.6:

$$I' = I'_1(x, y) + I'_2(x, y) + 2\sqrt{I'_1(x, y)I'_2(x, y)}\cos\Phi'(x, y). \tag{2.6}$$

Now, the interference terms $\sqrt{I_1(x,y)I_2(x,y)}$ and $\sqrt{I_1'(x,y)I_2'(x,y)}$ are treated by the cross-correlation function that demonstrates the explicit processing of the statistically distributed speckle patterns [7].

2.2 Shearography

As anticipated in Chapter 1, over the last few decades the aerospace industry has turned increasingly to carbon composite structural materials to make aircraft lighter and more economical. With this increased use, it has become apparent that conventional nondestructive testing methods are often impractical or unsuitable for tests of these materials. Many current composite designs use concepts similar to the sheet and stringer methods found in conventional aluminum air frames. However, designers today may use long unibundle laminate tape plies (stringers) to reinforce honeycomb composite sandwich panels (sheet or skins). Where conventional aluminum structures may have been riveted or welded in the past, today's modern aerospace composite structures are adhesively bonded [11]. Though, the risk of existence of different flaws in these kinds of materials is generally higher than that in metals, precisely because they are made of combination of two or more materials glued together [12]. These unwanted damages affect the structure and its mechanical properties, hence they must be revealed. Structural Health Monitoring of these kinds of materials can be conducted in different non destructive ways: let's refer, for example, to Digital Image Correlation [13], Fiber Bragg Grating sensors [14] and last but not least, Shearography. Shearography is an interferometric, non-destructive technique exploiting Speckle Noise to reveal very small displacement gradients on the μm^{-1} range, through which it enables small defects detection by comparing a relaxing and a loaded material state. Most commonly, Shearography setups are sensitive to the out-of-plane displacement gradients, but configurations sensitive to the in-plane displacement gradients also exist [15]. Since its first demonstration, speckle shearing interferometry, or Shearography has offered the specific advantages of interferometric full-field displacement gradient sensitivity using an optical configuration inherently more resilient to environmental disturbances and vibrations than other interferometric techniques such as electronic speckle pattern interferometry (ESPI) [16], [17]. Moreover, it can measure, record and interpret data over large areas (up to $2m^2$) with very short inspection times (15 seconds)

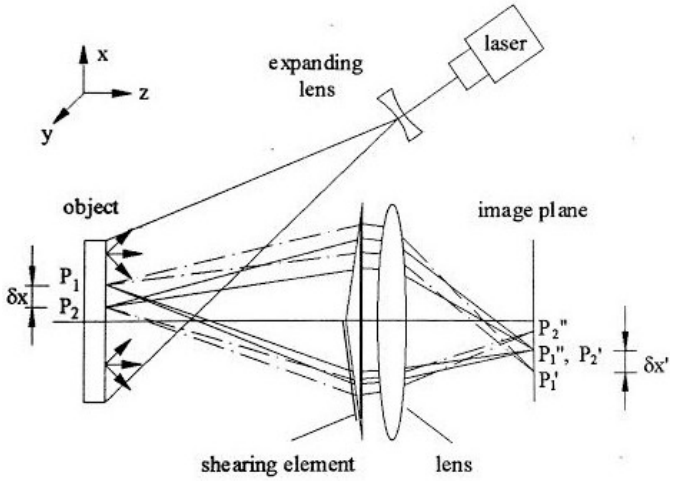

Figure 2.4: Refraction of laser beams by the shearing element [7]

and because of the fact that it measures a displacement derivative, it is completely independent on rigid body motions.

2.2.1 Fundamentals of optical setup

To make a measurement using Shearography the object to be studied is illuminated by a coherent laser light thus generating a Speckle Pattern according to the concepts disclosed in Sec. 2.1. The speckle pattern is imaged through a shearing device which coherently combines the Speckle Pattern with an identical but shifted version of itself [17]. After that, this two superimposed imaged Speckle Patterns are recorded by a camera. Hence, as shown in Fig. 2.4 extracted by [7], the shearing device generates the object points $1' - 2'$ and $1'' - 2''$ in the image plane. More precisely, the rays from $P_1(x, y)$ in the object are mapped into two points $P_1'(x, y)$ and $P_1''(x + \delta x', y)$ in the image plane. The same can be said for point $P_2 = P_2(x + \delta x, y)$ on the object's surface, and so on. Consequently, a given point in the image plane, P_1'' is superimposed to $P2'$, meaning that the shearing element brings the rays scattered from one point of the object's surface to meet with those scattered from a neighboring point in the image plane causing the interfering effect [7]. In a certain way, point P_2 can be seen as the reference beam involved in Holography. This means that Shearography does not need an additional reference beam, since it is "self referencing" thanks to the shearing effect, representing a great advantage with

respect to Holography. Referring again to Fig. 2.4, δx corresponds to the the shear on the object's surface, which is strictly linked to $\delta x'$ which is the shearing amount in the image plane by the Equation:

$$\delta x' = M\delta x \tag{2.7}$$

where $M = D_i/D_o$, being D_i the distance between the lens and the image plane and D_o the distance the lens and the object surface. The interferometric superposition of the two sheared images creates a so called Speckle Interferogram. Since the object is coherently illuminated and the spatial separation of the points P_1 and P_2 possesses a different phase relation $\theta_1 = \theta(x, y)$ and $\theta_2 = \theta(x + \delta x, y)$, the beams interfere with each other by superposition, producing a speckle image [7]. The phase relation difference is equal to:

$$\Phi = \theta(x + \delta x, y) - \theta(x, y) \tag{2.8}$$

The intensity distribution of the unloaded object I is given by:

$$I = 2a^2(1 + \gamma \cos \Phi) \tag{2.9}$$

where a is the light amplitude (equal for the two neighboring points), Φ is a random phase angle, and γ is the modulation of the interference term [18]. When an object undergoes a thermal, mechanical or vacuum load, its surface deformation causes an optical path change, inducing a relative phase change between the two interfering points. Hence, the intensity distribution of the speckle pattern is slightly altered:

$$I' = 2a^2[1 + \gamma \cos(\Phi + \Delta)] \tag{2.10}$$

where I' represents the intensity distribution after deformation and Δ is the relative phase change due to the relative displacement between $P(x, y)$ and $P(x + \delta x, y)$. The total energy recorded is proportional to the sum I_{tot} of the two intensity distributions:

$$I_{tot} = 2a^2[2 + \gamma \cos \Phi + \gamma \cos(\Phi + \Delta)]. \tag{2.11}$$

2.2.2 Components mechanics and shearograms

Let's remind, in the following, the formulations of the strain components characterizing a solid body subjected to a stress field: its shape variation caused by external forces can be modeled as the differences in its lengths and angles before and after load. If the volume element is a small cube, its deformation can be described by the tensile strain ϵ of its three sides and by the changes γ in its originally right angles, i.e. shear strain. The strain components ϵ and γ at a point define a strain dyadic, a strain matrix, and a strain tensor, which are similar to the corresponding quantities for the stress [7]. Equations 2.12 recap all the so called kinematic relations, connecting strains with displacements (u, v, w) along the Cartesian coordinates (x, y, z):

$$\begin{cases} \epsilon_{xx} = \frac{\partial u}{\partial x} \\ \epsilon_{yy} = \frac{\partial v}{\partial y} \\ \epsilon_{zz} = \frac{\partial w}{\partial z} \\ \epsilon_{xy} = 2\gamma_{xy} = 2(\frac{\partial v}{\partial x} + \frac{\partial u}{\partial y}) \\ \epsilon_{yz} = 2\gamma_{yz} = 2(\frac{\partial w}{\partial y} + \frac{\partial v}{\partial z}) \\ \epsilon_{zx} = 2\gamma_{zx} = 2(\frac{\partial u}{\partial z} + \frac{\partial w}{\partial x}) \end{cases} \tag{2.12}$$

Now, in order to understand the relationship between component mechanics and fringe generation by means of Shearography, let's refer to Fig. 2.5 A single object point P on the components surface moves for a small distance. A neighboring point Q moves slightly differently, providing a difference in movement between the two points. As already mentioned, the fringe at an arbitrary point of a shearogram depicts the relative phase change between two corresponding points on the object surface, which meet in the same point of the image plane. Again, the relative phase change is linked to the surface relative deformation between the two points [7]. Therefore, consider an arbitrary point $P(x, y, z)$ which gets into $P'(x + u, y + v, z + w)$ after deformation, with (u, v, w) being the Cartesian components of displacement. The optical path change δl_1 for the beam traveling from the light source $L(x_L, y_{,L}, z_L)$ to the camera at $K(x_K, y_K, z_K)$ via the point P' is:

$$\delta l_1 = (\overline{LP'} + \overline{P'K}) - (\overline{LP} + \overline{PK}). \tag{2.13}$$

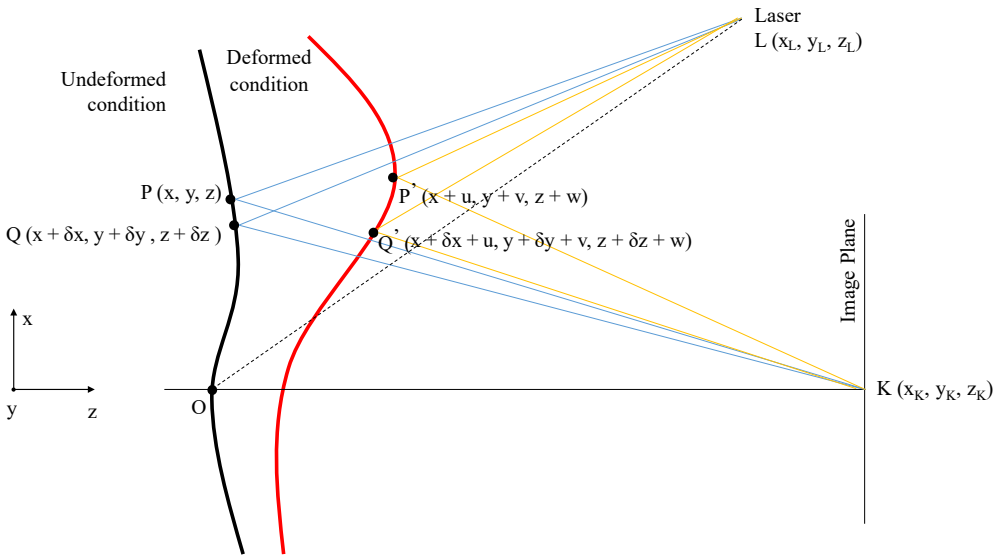

Figure 2.5: Optical path differences

The adjacent point $Q(x+\delta x, y+\delta y, z+\delta z)$ meeting P at the image plane because of the shearing effect moves to $Q(x+\delta x+u, y+\delta y+v, z+\delta z+w)$. Then, the beam coming from $L(x_L, y_{,L}, z_L)$ to $K(x_K, y_K, z_K)$ via Q' undergoes a path difference given by δl_2:

$$\delta l_2 = (\overline{LQ'} + \overline{Q'K}) - (\overline{LQ} + \overline{QK}). \tag{2.14}$$

The relative phase change is related to the relative pathchange between the two points, and it can be expressed by:

$$\Delta_{12} = \frac{2\pi}{\lambda}(\delta l_1 - \delta l_2). \tag{2.15}$$

Now, Equation 2.13 can be rewritten as:

$$\delta l_1 = (\overline{LP'} + \overline{P'K}) - (\overline{LP} + \overline{PK}) = (\overline{LP'} - \overline{LP}) + (\overline{P'K} - \overline{PK}) \tag{2.16}$$

and

$$\begin{cases} (\overline{LP'} - \overline{LP}) = \frac{(\overline{LP'}^2 - \overline{LP}^2)}{\overline{LP'} + \overline{LP}}, \\ (\overline{P'K} - \overline{PK}) = \frac{(\overline{P'K}^2 - \overline{PK}^2)}{\overline{P'K} + \overline{PK}}. \end{cases} \tag{2.17}$$

Moreover:

$$\begin{cases} \overline{LP'}^2 = [(x+u)-x_L]^2 + [(y+v)-y_L]^2 + [(z+w)-z_L]^2 = \\ \qquad = [(x-x_L)+u]^2 + [(y-y_L)+v]^2 + [(z-z_L)+w]^2 \\ \overline{LP}^2 = (x-x_L)^2 + (y-y_L)^2 + (z-z_L)^2 \\ \overline{P'K}^2 = [(x+u)-x_K]^2 + [(y+v)-y_K]^2 + [(z+w)-z_K]^2 = \\ \qquad = [(x-x_K)+u]^2 + [(y-y_K)+v]^2 + [(z-z_K)+w]^2 \\ \overline{PK}^2 = (x-x_K)^2 + (y-y_K)^2 + (z-z_K)^2. \end{cases} \tag{2.18}$$

Now, since we can assume that the distances from the laser to the object's surface and from the camera to the object are much larger than the object size:

$$\begin{cases} \overline{LP} \approx \overline{LP'} \approx \overline{LO} = D_L \\ \overline{PK} \approx \overline{P'K} \approx \overline{OK} = D_K \end{cases} \tag{2.19}$$

By inserting the first two formulations of Equation 2.18 and the first of Equation 2.19 into the first formula of Equation 2.17, one can obtain (since u, v, $w << 1$, $u^2 \approx v^2 \approx w^2 \approx 0$):

$$\begin{aligned} (\overline{LP'} - \overline{LP} &= \frac{\left(\overline{LP'}^2 - \overline{LP}^2\right)}{\overline{LP'} + \overline{LP}} \\ &= \frac{1}{2D_L}[2(x-x_L)u + u^2 + 2(y-y_L)v + v^2 + 2(z-z_L)w + w^2]. \end{aligned} \tag{2.20}$$

Hence, the first formulation of Equation 2.19 simplifies into:

$$(\overline{LP'} - \overline{LP}) = \frac{(x-x_L)}{D_L}u + \frac{(y-y_L)}{D_L}v + \frac{(z-z_L)}{D_L}w. \tag{2.21}$$

Equally, the second statement of Equation 2.17 will become:

$$(\overline{P'O} - \overline{PO}) = \frac{(x-x_K)}{D_K}u + \frac{(y-y_K)}{D_K}v + \frac{(z-z_K)}{D_K}w. \tag{2.22}$$

Now, by substituting Equations 2.21 and 2.22 into Equation 2.16:

$$\begin{aligned}\delta l_1 &= \left[\frac{(x-x_L)}{D_L}u + \frac{(y-y_L)}{D_L}v + \frac{(z-z_L)}{D_L}w\right] + \\ &+ \left[\frac{(x-x_K)}{D_K}u + \frac{(y-y_K)}{D_K}v + \frac{(z-z_K)}{D_K}w\right] = \\ &= \left(\frac{(x-x_L)}{D_L} - \frac{(x-x_K)}{D_K}\right)u + \left(\frac{(y-y_L)}{D_L} - \frac{(y-y_K)}{D_K}\right)v + \left(\frac{(z-z_L)}{D_L} - \frac{(z-z_K)}{D_K}\right)w.\end{aligned} \tag{2.23}$$

By performing the same operations for Equation 2.14 and knowing that δx, δy and δz are much smaller than D_L and D_K ($\delta x/D_L \approx \delta x/D_K \approx \delta y/D_L \approx \delta y/D_K \delta z/D_K \approx 0$) the relative path change δl_2 will be:

$$\begin{aligned}\delta l_2 = &\left(\frac{x-x_L}{D_L} + \frac{x-x_K}{D_K}\right)(u+\delta u) + \left(\frac{y-y_L}{D_L} + \frac{y-y_K}{D_K}\right)(v+\delta v) + \\ &+ \left(\frac{z-z_L}{D_L} + \frac{z-z_K}{D_K}\right)(w+\delta w).\end{aligned} \tag{2.24}$$

By substituting δl_1 and δl_2 into Equation 2.15, one will obtain:

$$\Delta_{12} = \frac{2\pi}{\lambda}(\delta l_1 - \delta l_2) = A_1\delta u + A_2\delta v + A_3\delta w, \tag{2.25}$$

where:

$$\begin{aligned}A_1 &= \frac{2\pi}{\lambda}\left(\frac{(x_L-x)}{D_L} + \frac{(x_K-x)}{D_K}\right) \\ A_2 &= \frac{2\pi}{\lambda}\left(\frac{(y_L-y)}{D_L} + \frac{(y_K-y)}{D_K}\right) \\ A_3 &= \frac{2\pi}{\lambda}\left(\frac{(z_L-z)}{D_L} + \frac{(z_K-z)}{D_K}\right)\end{aligned} \tag{2.26}$$

Now, according to Equation 2.19 it is possible to explicit D_L and D_K - that are two constants depending on the optical shearographic setup - as:

$$\begin{cases} D_L = x_L^2 + y_L^2 + z_L^2 \\ D_K = x_K^2 + y_K^2 + z_K^2 \end{cases} \tag{2.27}$$

Assuming a x - directed shear, Equation 2.25 can be expressed as:

$$\Delta_x = \left(A_1 \frac{\delta u}{\delta x} + A_2 \frac{\delta v}{\delta x} + A_3 \frac{\delta w}{\delta x} \right) \delta x, \tag{2.28}$$

and if the shearing amount δx is small, the relative displacement is approximated by the derivatives of displacements, being:

$$\Delta_x = \left(A_1 \frac{\partial u}{\partial x} + A_2 \frac{\partial v}{\partial x} + A_3 \frac{\partial w}{\partial x} \right) \delta x. \tag{2.29}$$

The same thing can be also written for a shear oriented along the y direction:

$$\Delta_y = \left(A_1 \frac{\partial u}{\partial y} + A_2 \frac{\partial v}{\partial y} + A_3 \frac{\partial w}{\partial y} \right) \delta y. \tag{2.30}$$

Finally, Equations 2.29 and 2.30 express the relationship between components mechanics and the relative phase change Δ [7], being their terms the deformation gradients in the given shear direction.

2.2.3 Generation of a Shearogram

As mentioned in the previous Section, the generation of a Shearogram is given by the meeting, in the image plane, of two light waves coming from two different point belonging to the object plane and separated by a distance δx called *shear*, that will be $\delta x'$ in the image plane. Using the interference of each point in the image plane yields a speckle interferogram [7]. The light waves reflected from the two different

points can be modeled by the following exponential functions, as described in [7]:

$$\begin{cases} U(x,y) = U_1 = a_1 e^{i\theta(x,y)} = a_1 e^{i\theta_1} \\ U(x+\delta x, y) = U_2 = a_2 e^{i\theta(x+\delta x,y)} = a_1 e^{i\theta_2} \end{cases} \tag{2.31}$$

where $\theta(x,y)$ and $\theta(x+\delta x,y)$ represent the random phase relation of the light coming from the two points on the object's surface and a_1 and a_2 are the light amplitudes, assumed equal for the two neighboring points. The total light field given by the interferometric effect will be:

$$U_{tot} = U(x,y) + U(x+\delta x,y) = U_1 + U_2 = a_1 e^{i\theta_1} + a_2 e^{i\theta_2}. \tag{2.32}$$

The intensity I detected in the image plane is:

$$\begin{aligned} I = U_{tot} U_{tot}^* &= (a_e^{i\theta_1} + a_2 e^{i\theta_2})(a_1 e^{-i\theta_1} + a_2 e^{-i\theta_2} = \\ &= (a_1^2 + a_2^2) + a_1 a_2 \left[e^{i(\theta_1-\theta_2)} + e^{-i(\theta_1-\theta_2)} \right], \end{aligned} \tag{2.33}$$

where $\Phi = \theta(x,y) - \theta(x+\delta x,y) = \theta_1 - \theta_2$ represents the phase difference between the two points, that is random since θ_1 and θ_2 are random phase angles too. Now, converting Equation 2.33 by means of the Euler equation $e^{i\theta} + e^{-i\theta} = 2\cos\Phi$, one can obtain:

$$I = (a_1^2 + a_2^2) + 2a_1 a_2 \cos\Phi = 2I_0(1 + \gamma\cos\Phi), \tag{2.34}$$

where $I_0 = (a_1^2 + a_2^2)/2$ is the intensity mean value (background), $\gamma = 2a_1 a_2/(a_1^2 + a_2^2)$ is the modulation of the interference term (contrast), and $\Phi = \theta_1 - \theta_2$ is the random phase difference [7]. When an object undergoes a deformation (statically, dynamically or thermally induced), a change of the optical phase difference Δ takes place (as described in the previous Section), hence in this state, Equation 2.34 becomes:

$$I' = 2I_0(1 + \gamma\cos\Phi') = 2I_0[1 + \gamma\cos(\Phi + \Delta)]. \tag{2.35}$$

In particular, Δ, can be expressed as $\Delta = \Phi' - \Phi$, where $\Phi' = \theta_1' - \theta_2'$ is the random phase difference after loading. It is also possible to write:

$$\Delta = \Phi' - \Phi = (\theta_1' - \theta_2') - (\theta_1 - \theta_2) = (\theta_1' - \theta_1) - (\theta_2' - \theta_2). \tag{2.36}$$

Consequently, the relative phase change Δ can be reduced to the difference of the light path δ_1 and δ_2:

$$\Delta = \frac{2\pi}{\lambda}(\delta_1 - \delta_2), \tag{2.37}$$

where δ_1 and δ_2 represent the phase change of the scattered light beams from the two points on the object's surface, undergoing the load imposition. Let's remind that all the reported formulation are taken from [7].

2.2.4 Phase Shifting Shearography

Numerical evaluation of a shearogram requires the determination of its relative phase change Δ, thus of the phase differences Φ and Φ', corresponding to the unloaded and the loaded state. The so called Phase-Shifting technique enables Digital Shearography to be observed in real time and evaluated quantitatively as well [7]. In particular, there exist two methods for determining the phase distributions Φ and Φ' : time-dependent (or temporal) and spatial-phase shifting techniques. Temporal phase shifting, provides a solvable equations system consisting of at least three unknowns (the mean intensity I_0, the modulation of the interference term γ and the random phase distribution Φ. In order for this system of equations to be solvable, phase-shifted data are acquired in a temporal sequence of camera frames [19] (three, four or five interferograms). Spatial Phase Shifting, on the contrary, has the advantage for the phase distribution to be determined from only a single interferogram, despite being less accurate than the temporal method. The intensity of an interferogram can be modeled by Equations 2.33 and 2.34, but the CCD camera can register only one interferogram, containing three unknowns, as mentioned before, thus the need of a system of at least three equations. For this purpose, a known additional phase ϕ (in general 120° for each of the three equations) is introduced by shifting the interfering light waves one against the other [7]. Hence, shifting ϕ three times and evaluating the intensity I_i, one can obtain the following three equations, as described in [7]:

$$\begin{cases} I_1 = 2I_0[1 + \gamma \cos \Phi] \\ I_2 = 2I_0[1 + \gamma \cos(\Phi + 120°)] \\ I_3 = 2I_0[1 + \gamma \cos(\Phi - 120°)]. \end{cases} \tag{2.38}$$

Consequently, the phase difference distribution Φ can be calculated as:

$$\Phi = \arctan \frac{\sqrt{3}(I_3 - I_2)}{2I_1 - I_2 - I_3}. \tag{2.39}$$

On the contrary, shifting the additional phase ϕ five times, the following system is obtained:

$$\begin{cases} I_1 = 2I_0[1 + \gamma \cos(\Phi - 180^\circ)] \\ I_2 = 2I_0[1 + \gamma \cos(\Phi - 90^\circ)] \\ I_3 = 2I_0[1 + \gamma \cos \Phi] \\ I_4 = 2I_0[1 + \gamma \cos(\Phi + 90^\circ)] \\ I_5 = 2I_0[1 + \gamma \cos(\Phi + 180^\circ)] \end{cases} \tag{2.40}$$

and the resulting phase distribution is computed by:

$$\Phi = \arctan \frac{2(I_2 - I_4)}{-I_1 + 2I_3 - I_5}. \tag{2.41}$$

Now, let's focus on the arrangement of Phase-Shifting Shearography. The generation of the additional phase ϕ is made significantly easy by using a Michelson interferometer as a shearing device (Fig. 2.6). The object to be tested is illuminated by an expanded laser beam. The reflected beam passes the Michelson interferometer and is focused on the CCD array of the image plane [7]. By a small tilting of the shear mirror (Fig. 2.6), two shifted images of the object are generated and the interferometric superimposition of both speckle interferograms yields a new specklegram in the image plane. The Michelson interferometer provides high accuracy in the magnitude and direction of the shearing by rotating the precision screw of the corresponding mirror, however the mirror positioning remains one of the uncertainty sources in the quantitative analysis of shearograms [15], as we will see later. Now, in order to generate the additional phase ϕ, the Phase Shift mirror (Fig. 2.6) performs a linear movement driven by a piezoelectric crystal. When the mirror is shifted for a path δl, the optical path length is changed for $2\delta l$ by the forward and backward path. The additional phase ϕ will be given by:

$$\phi = \frac{2\pi}{\lambda} 2\delta l \tag{2.42}$$

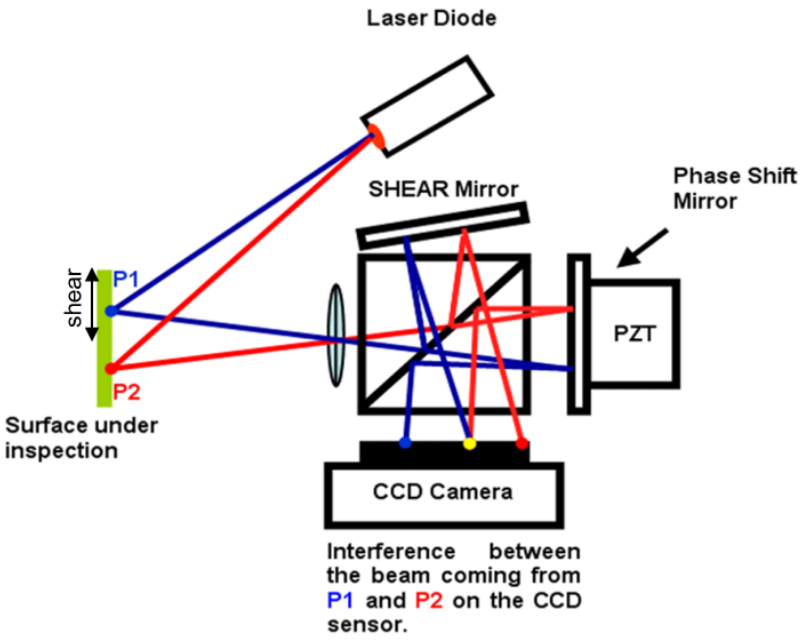

Figure 2.6: Arrangement of Phase-Shifting Shearography based on a Michelson Interferometer

Recording an interferogram takes approximately 20 ms. The movement of the piezoelectric-driven mirror can be completed within 1 ms. However, the recording of the successive interferogram requires a pause of approximately 50 ms to move the Phase Shift mirror in order to stabilize the position. Storing the three intensities requires less than 1 s.

2.2.5 Relative phase change computation in a Shearogram

In the previous Section the need to store three or more images for relative phase calculation was discussed. Many systems use four images as input for evaluation, meaning that each of the four interferogram is obtained after the phase is shifted for $+90°$, i.e., the linear movement of the phase-shift mirror for $\lambda/8$, and it is then

stored. The four images are related to the following four Equations:

$$\begin{cases} I_1 = 2I_0[1 + \gamma \cos \Phi] \\ I_2 = 2I_0[1 + \gamma \cos(\Phi + 90°)] \\ I_3 = 2I_0[1 + \gamma \cos(\Phi + 180°)] \\ I_4 = 2I_0[1 + \gamma \cos(\Phi + 270°)]. \end{cases} \tag{2.43}$$

Converting the formulations in Equation 2.43 the magnitude of the phase can be calculated at each point of the speckle interferogram in the undeformed or for the preloaded state:

$$\Phi = \arctan \frac{(I_4 - I_2)}{(I_1 - I_3)}. \tag{2.44}$$

Now, the sign of the numerator and denominator can be studied separately. At first, the numerator becomes:

$$\begin{aligned} I_4 - I_2 &= 2I_0[1 + \gamma \cos(\Phi + 270°)] - 2I_0[1 + \gamma \cos(\Phi + 90°)] \\ &= 2I_0(1 + \gamma \sin \Phi) - 2I_0(1 - \gamma \sin \Phi) = 4I_0\gamma \sin \Phi, \end{aligned} \tag{2.45}$$

while the denominator:

$$I_1 - I_3 = 2I_0(1 + \gamma \cos \Phi) - 2I_0[1 + \gamma \cos(\Phi + 180°)] = 4I_0 \cos \Phi. \tag{2.46}$$

It appears clear that the signs of the numerator and denominator are established by the signs of $\sin \Phi$ and $\cos \Phi$ where $4I_0\gamma \geq 0$, and the phase relation Φ can be determined in the range $[0; 2\pi]$ accordingly. In particular, when the numerator and the denominator are positive, the phase values are in the first quadrant; for a positive numerator and a negative denominator, they are in the second quadrant; for a negative numerator and a negative denominator, in the third quadrant, and for a negative numerator and a positive denominator, in the fourth one. Now, if the phase value of 2π corresponds to a white point in the phase image, then the phase value 0 is a black point, so if we consider a *uint8* image, 256 gray levels in the range $[0; 255]$ will fill the range $[0; 2\pi]$ [7]. At this point, for the calculation of the relative phase change Δ, additional four images have to be captured after the application of a load, and the relative phase distribution Φ' can be computed as in Equation 2.44 as well. As soon as the phase distributions Φ and Φ' are determined,

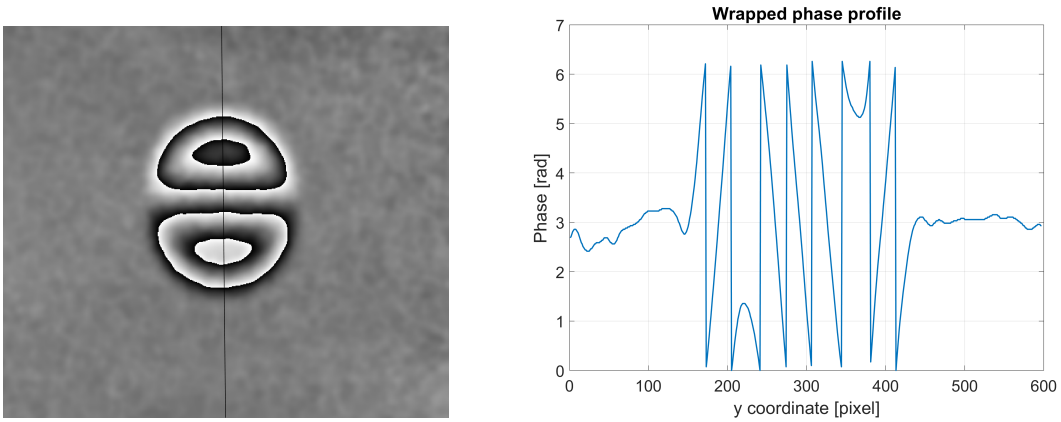

(a) *Wrapped phase map (butterfly fringe pattern)*

(b) *Wrapped phase profile extracted in the middle of the phase map in Fig. 2.7a*

Figure 2.7: Example of a wrapped relative phase change distribution

the relative phase difference Δ can be calculated by digital subtraction using the following equation:

$$\Delta = \begin{cases} \Phi' - \Phi & \text{for } \Phi' \geq \Phi, \\ \Phi' - \Phi + 2\pi & \text{for } \Phi' \leq \Phi. \end{cases} \tag{2.47}$$

Because the phase distributions Φ' and Φ lie between 0 and 2π, the relative phase change Δ will result in a fringe pattern wrapped into the range from 0 to 2π as well. In Fig. 2.7a we can see the typical phase map revealed in presence of a defect in the structure: it is called "butterfly-shaped fringe pattern", where the two lobes represent the positive and the negative side of the out of plane-displacement derivative computed along the shear direction, and in Fig. 2.7b a vertical line of the phase maps is extracted, showing that phase is effectively varying between 0 and 2π.

2.2.6 Interferogram Evaluation

In order to solve the issue revealed in Fig. 2.7, i.e. the fact that the phase map yields only a sawtooth function (showing the phase modulo 2π), these 2π jumps have to be eliminated by the so called *Phase Unwrapping* methods. However, before performing Phase Unwrapping, it becomes necessary to reduce the high frequency noise that, by their very nature, affects Speckle Interferometry techniques [17].

In the following paragraphs different filtering and unwrapping techniques will be discussed.

2.2.6.1 Phase map Filtering

Filtering is a typical operation in image processing consisting in defining a so called *Convolution Kernel*, i.e. a sort of window of dimensions $n \times n$, with $n << imagesize$, scanning and performing operations through the overall image. Typical values for n are: 3, 5, 7. Hence, each pixel inside the image is surrounded by this moving $n \times n$ window, in which the $n \times n$ elements are the weighting factors (coefficients) of the gray values of the window. In particular, the gray values in the original image are multiplied by the corresponding coefficients of the kernel whose resulting $n \times n$ products are added, and finally divided by the sum S of the coefficients $C(x, y)$ of the kernel [7]. Thus, the filtered gray value of the examined pixel $\overline{I}(x, y)$ will be:

$$\overline{I}(x, y) = \frac{1}{S} \sum_{x=1}^{n} \sum_{y=1}^{n} C(x, y) I(x, y). \tag{2.48}$$

The process described in Equation 2.48 usually starts in the upper left of the image, and is iterated to the next pixel to the right, and so on. When the end of the row is reached, the process is resumed at the beginning of the next row. Now, according to the values assumed by the Kernel coefficients, the effect of filtering could be low-pass or high-pass. The latter is usually used for edge detection, as it reveals strong variations in light intensity inside the image. For example, the gradient filter kernel (one of the most used for high-pass filtering) has an antisymmetric structure, as to highlight variations in light intensity occurring in the orthogonal direction with respect to the antisymmetry axis. In [20] a review of the principal high pass filters is presented. However, Shearography revealed that phase maps requires not to be subjected to an edge detection for further processing, but to avoid the high frequency noise caused by Speckle itself. Therefore, low-pass filters will be used for our applications. The simplest low pass filter kernel is the 3×3 average filter:

$$C_{average} = \frac{1}{9} \begin{bmatrix} 1 & 1 & 1 \\ 1 & 1 & 1 \\ 1 & 1 & 1 \end{bmatrix} \tag{2.49}$$

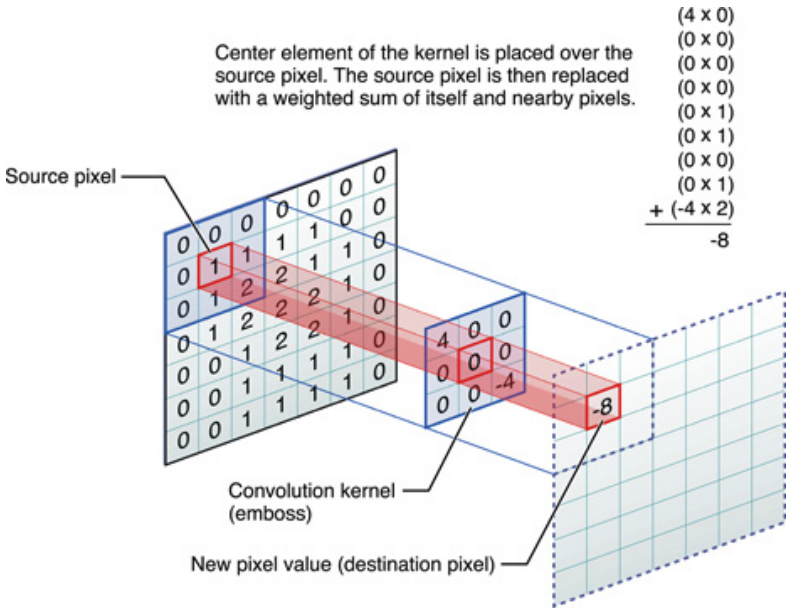

Figure 2.8: Image filtering process

This returns the value of a particular pixel as the average of values within a 3×3 neighborhood centered on the pixel and results in blurring or smoothing of an image [17]. Now, it has not to be forgotten that the analysis deals with sawtooth distributions: applying a low-pass filter not only reduces the noise, but also smears out the 2π discontinuities, see for example the effect of the average filter in Fig. 2.9: by applying a 3×3 kernel all the discontinuities are visible yet, but the image is still pretty noisy (Fig. 2.9a), while if we increase the kernel size up to 15×15, we lose the 2π discontinuities in the center of the phase map (Fig. 2.9b). This issue is treated by applying a sine-cosine filter, in order for the phase information not to be lost. The sine-cosine filter works as shown in Fig. 2.10 taken from [21]. The sine and the cosine of the relative phase change Δ are computed and smoothed (by a low-pass filter) separately. From the filtered sine $\sin \Delta'$ and cosine $\cos \Delta'$ fringe patterns the filtered phase fringe pattern Δ' can be calculated by the four-quadrant inverse tangent of the sine and cosine patterns. This process is usually repeated two or three times, but it's crucial, in order to avoid loss of information, that in-between the single repetition of the filter steps, the filter is always recomputed before the next filter step is initiated. If this rule is observed, then the continuous repetition of the process automatically leads to an adapted filter effect: sparse

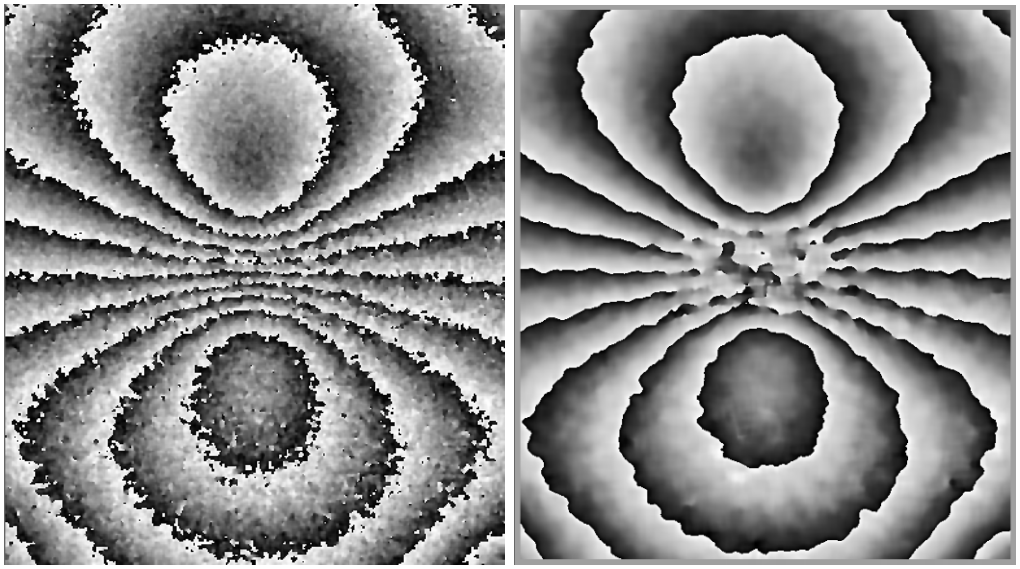

(a) 3×3 *Convolution Kernel* **(b)** 15×15 *Convolution Kernel*

Figure 2.9: Effect of different average kernel sizes on phase discontinuities

fringes are filtered with increasing strength from step to step, whereas dense fringes are not filtered any further after the first few steps and are thus not smeared out [21]. At this point, one has to choose the most appropriate low-pass filter to apply to the sine and cosine fringe patterns. The very first option is certainly the average filter discussed before, but in cases of more complex/noisy phase maps it could be necessary to implement more advanced filtering techniques. The so called *scale-space filter* [22] is one of the most promising, consisting in the combination of image multi-level decomposition and Gaussian kernel based-convolution. In [21] some results relative to the application of this filter to a Shearographic phase map are presented. Another valid possibility is the *partially recursive filter* developed by B. Pfister [21], in which the moving kernel gives more weight to the neighboring pixels that have already been filtered than to the unfiltered ones, being:

$$C_{Pfister} = \begin{bmatrix} 1 & 2 & 3 & 2 & 1 \\ 2 & 3 & 4 & 3 & 2 \\ 3 & 4 & 1 & 1 & 1 \\ 1 & 1 & 1 & 1 & 1 \\ 1 & 1 & 1 & 1 & 1 \end{bmatrix}. \tag{2.50}$$

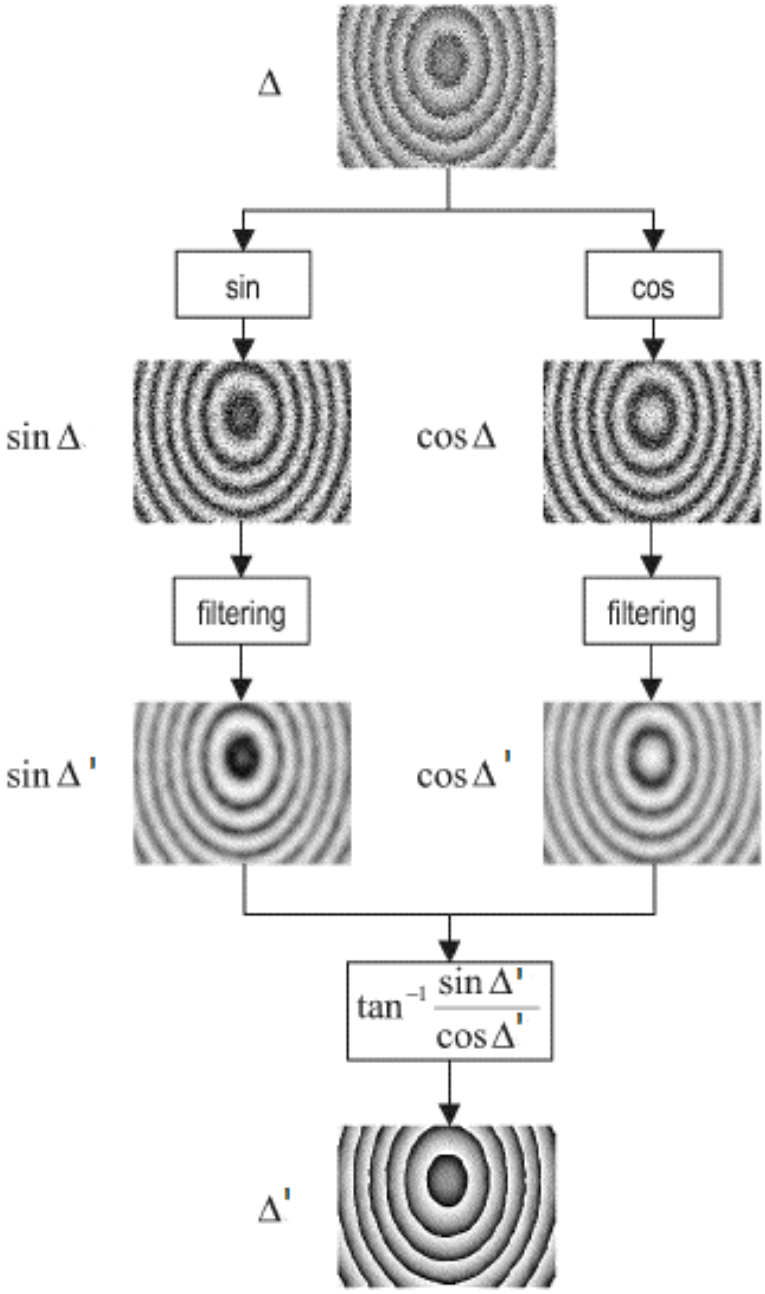

Figure 2.10: Sine-Cosine filter scheme [7]

The last low-pass filter we're going to focus on, is the one developed by the authors in [21], that consists in the choice of an anisotropic kernel ($n \times m$, with $n \neq m$) and in increasing the repetitions. In practice, the filter strength is unequal for the horizontal and vertical directions. If the process of sine and cosine calculation, filtering, and inverse tangent calculation is repeated 20 to 30 times, it is possible to observe the following effect: dense fringes, which are perfectly filtered after a few repetitions, are not affected by the later iterations, but sparse fringes continue to be filtered more strongly from iteration to iteration. In other words, the process produces the effect of an automatic adaptive filter [21]. As for the other filters, each filtering step has to conclude with the phase re-computation. The choice of the direction along which the larger kernel dimension has to stand, depends on the fringe distribution inside the image. For example, let's suppose to have to choice between a 7×3 or a 3×7 kernel: if the fringe density is in the horizontal direction, this will correspond to the minimum kernel dimension (3), while in the vertical direction the shorter side of the kernel will be placed, thus being the moving window a 7×3 matrix. In this way, where the fringes are denser, we obtain a better resolution (minor loss of data) but the other kernel dimension allows a successful filtering process. In Fig. 2.11 it is possible to observe the effects of the partially recursive and the anisotropic filter at the first step of iteration.

2.2.6.2 Phase Unwrapping

Phase Unwrapping, or demodulation, is a process aiming at resolving the 2π discontinuities, adding a step function consisting only of 2π steps. In general,the 2π phase discontinuities can be removed either along one or more of the spatial coordinates, or along the time axis. The two approaches are termed spatial and temporal phase unwrapping, respectively [23]. The one we are interested in is Spatial phase unwrapping, that is often referred to as two-dimensional phase unwrapping. Now, let's consider for a while a one-dimensional case, as the one shown in Fig. 2.12 taken from [24]: the continuous profile is obtained by adding, to each fringe, a $2k\pi$ quantity, where k is a positive or negative integer value. In order to state which one is the phase corresponding to $k = 0$, hence which is the zeroth order fringe, there exist different methods, that we are going to discuss later. In this phase, let's consider that the reference point corresponding to the zeroth

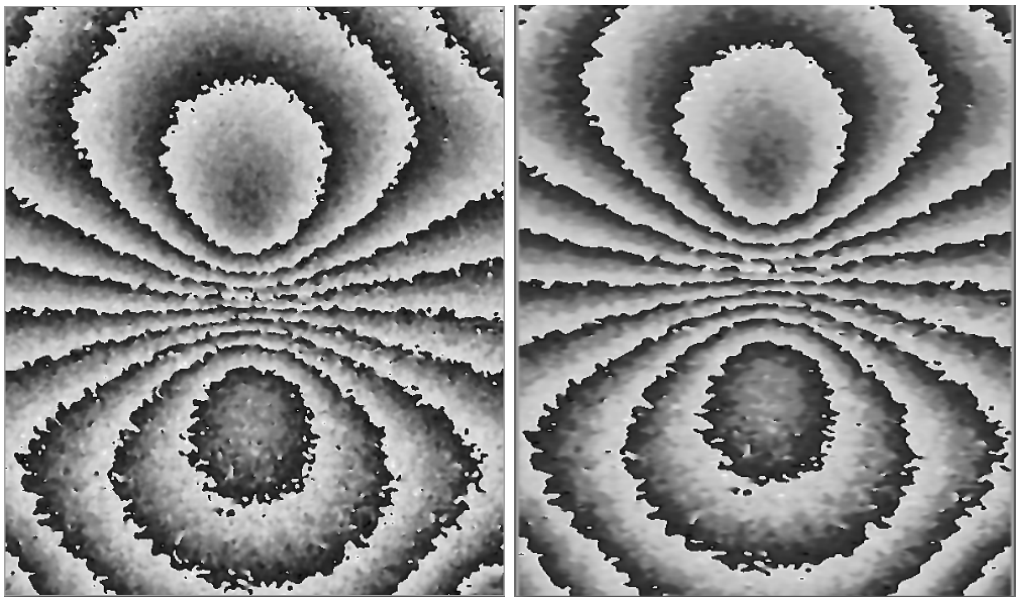

(a) *Partially recursive filter* **(b)** *Anisotropic filter*

Figure 2.11: Advanced low-pass filters results

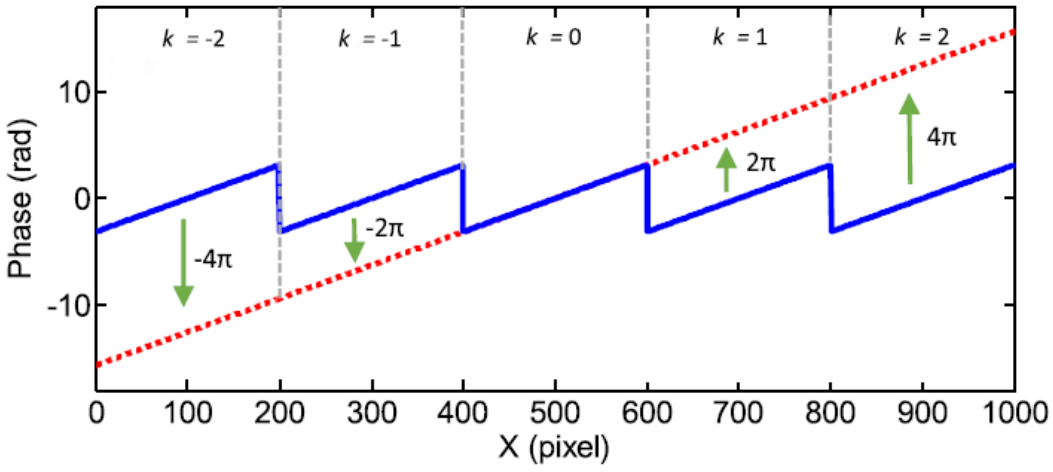

Figure 2.12: Compensation of 2π discontinuities in a sawtooth phase profile without noise

order fringe is arbitrarily chosen, as it often happens, thus the resulting *relative* phase distribution $\Delta_r(x, y)$ will be:

$$\Delta_r(x, y) = \Delta_a(x, y) + C \tag{2.51}$$

where $\Delta_a(x, y)$ is the absolute phase distribution, and C is a positive or negative 2π multiple, representing the *Unwrapping Error* due to the arbitrary choice of the zeroth order fringe. Before discussing the resolution of the unwrapping error, in the following the principal two-dimensional unwrapping algorithms will be presented. Demodulation procedures can be grouped into two classes [7]:

- the path-independent ones, where the order in which the pixels are investigated and unwrapped is predetermined by the process;
- the path-independent ones, where the order of the investigated pixels is determined by the phase value of pixel.

The simple procedure shown in Fig. 2.12 is only suitable in theory, since Speckle Pattern based methods are by definition affected by high frequency noise, thus, in addition to proper filtering algorithms discussed in the previous Section, more sophisticated unwrapping procedures are required. For this purpose, a suitable unwrapping algorithm is the branch cut algorithm [17]. This algorithm involves the detection of phase residues which are found at the points where the breaks in the fringes occur. In Appendix A in [25] the Goldenstein unwrapping method is presented. This is based on the fact that while in the one-dimensional case, the path of the line integral is fixed, two dimensions offer the possibility to get from one point to another by a multitude of possible curves. Ghiglia and Pritt have thus reduced the problem of two-dimensional phase unwrapping to the problem of path invariance of the unwrapping [26]: only when the line integral from one point to another is independent of the path, a correct phase value can be calculated without significant unwrapping errors. This is equivalent to the condition that the integral along any closed path is zero. In the presence of phase noise, such a path integral can yield a non-zero value, also called a *phase residue charge* or *residue*, in analogy to residues encountered in complex analysis [25]. The simplest closed path that can be tested is along a 2×2 pixel path. So a residue of charge $\pm m$ can be attributed to the space in between four adjacent pixels, whenever the

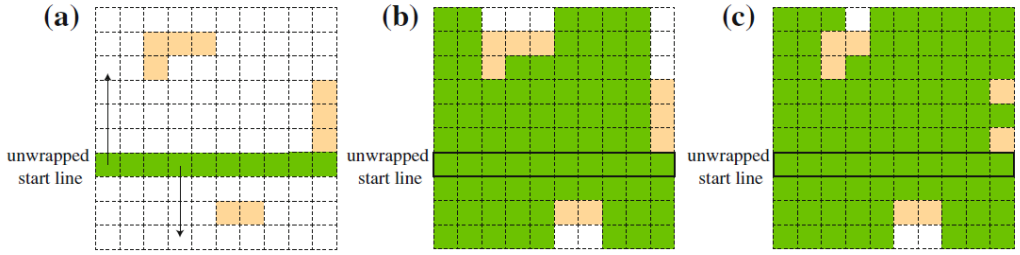

Figure 2.13: Goldenstein Unwrapping procedure taken from [27]

sum of all four gradients differs from zero. If such a residue is detected in the path, a charge of $\pm m$, depending on the magnitude of the residue is assigned to the middle of this pixel cluster. To ensure path invariance for all integration paths, the unwrapping path may never circle such a residue. To eliminate their influence on the unwrapping process, residues of opposite charge are connected (balanced) by so-called branch cuts, i.e. a line of pixels which must not be crossed during the unwrapping procedure. In this way, for any closed integration path, the sum of included residues will always equal zero. Residues that cannot be balanced by residues of opposite charge can be connected to the outer borders of an image matrix by a branch cut [25]. The final task is now to unwrap the phase data for the whole image along a path that never crosses any branch cuts. A very good implementation for Matlab exists, where no special path for unwrapping is designed, but the pixels are unwrapped one at a time, starting from a reference pixel and continuing the unwrapping in a closed path, also termed as *flood filling*. Hence, once having placed all the branch cuts to balance residues, one has to look for a line/column where no branch cuts have been detected, and to choose it as starting line/column to which applying the 1D Itoh's unwrapping [27]. Now, starting from this line/column one has to perform the same operation to all the perpendicular lines/columns to both sides completely or until a brunch cut has been reached. At the end, the phase value of all pixels that have not been unwrapped will be determined by simple flood filling. This process is shown in Fig. 2.13. Moreover, another popular approach unwraps pixel in order of quality, which is determined from the phase gradient within the phase map [17]. The phase is unwrapped along the path of the minimum spanning tree. The latter is a connecting tree that connects all vertices with the minimum total weight in a weighted graph [23]. In

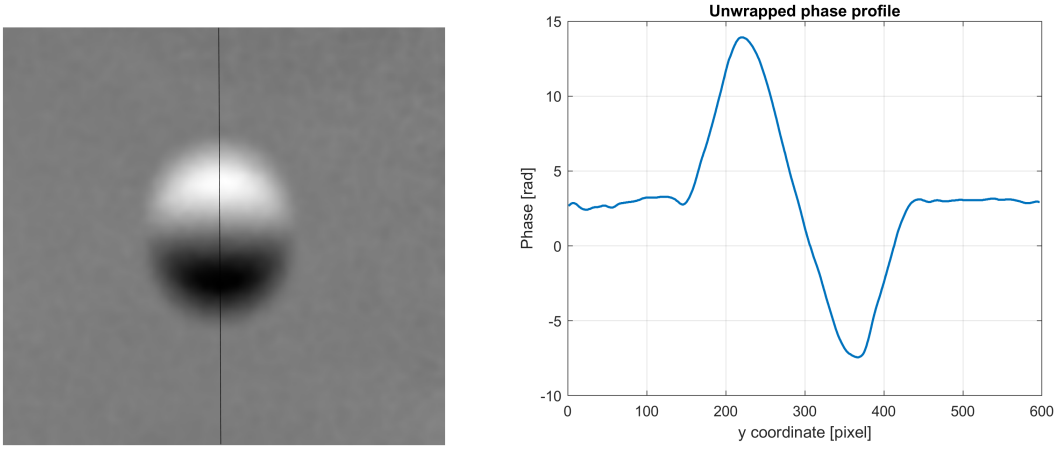

(a) *Unwrapped phase map through Goldenstein method*

(b) *Unwrapped phase profile extracted in the middle of the phase map in Fig. 2.14a*

Figure 2.14: Example of an unwrapped relative phase change distribution

phase unwrapping, the speed of the process can be improved by considering smaller regions of data within the phase map known as tiles [23]. Another method is the one described by Liu and Yang [28]: this approach attempts unwrapping phase in a noise-disturbed phase map, which is characterized by broken fringes induced by different sources. In this method, broken fringes are detected and estimated, and the phase map is segmented into different regions based on the quality of phase. Regions are ranked and arranged to construct a systematic unwrapping sequence. The last method that will be mentioned is the one described in [29]: it consists of unwrapping of phase spatial maps taking only as parameter of reliability-guided the intensity modulation matrix (IMM) of the fringes pattern. Before calculating the IMM, the phase map is filtered appropriately. The elements of this IMM are used to identify the direction of phase unwrapping over the filtered phase map. It means that the pixel with higher parameter value in the parameter map will be phase unwrapped earlier. In this thesis, the chosen unwrapping method is the Goldenstein one due to its good robustness in cases of noisy phase maps and to its good implementation in Matlab environment. Fig. 2.14 shows the results obtained by unwrapping the phase map in Fig. 2.7a.

Now, as already mentioned at the beginning of this Section, the unwrapping process starts from a reference point that is chosen arbitrarily or by some criteria

which, however, is not dependent on the zeroth order fringe position. For this reason, the outcoming phase map contains *relative* phase values. This is not relevant if we want to perform a qualitative analysis of the deformation distribution, or if we only want to check the presence of defects, but if one is interested in the actual strain/deformation values, the determination of the constant C in Equation 2.51, i.e. of the unwrapping error, is compulsory [30]. For this purpose, different possibilities are available:

1. Knowing the boundary conditions of the test case. This would be the easier way, but it is applicable only for simple problems, thus not practical for the complex boundary conditions encountered in industry [7],[30];
2. Using an additional, reference measurement system capable of measuring the absolute displacement of a single object point [31];
3. Two-wavelength method;
4. Fringe carrier method;
5. Zeroth order fringe localization;
6. Linear fitting over small loading sub steps;
7. Adding and subtracting method.

Solutions 1 and 2 are easily understandable, thus let's focus on solutions from 3 to 7.

Two-wavelength method The relative phase change Δ at an arbitrary point (i, j) is equal to $2\pi N(i, j)$, where $N(i, j)$ is the fringe order expressed in decimal number. Moreover, in cases where the illumination angle with respect to the surface is 0, i.e. when Eq. 2.29 becomes $\Delta = \frac{4\pi\delta x}{\lambda}\frac{\partial w}{\partial x}$, it is obtained:

$$\Delta(i,j) = 2\pi N(i,j) = \frac{4\pi\delta x}{\lambda}\frac{\partial w}{\partial x} \Rightarrow N(i,j)\lambda = 2\delta x\frac{\partial w}{\partial x} \tag{2.52}$$

where $\partial w/\partial x$ is the measurement signal, λ is the wavelength and δx is the shearing amount in x direction. In order to determine the fringe order $N(i, j)$, two different shearographic fringe patterns recorded by using two different wavelengths λ_1 and

λ_2 ca be used. When two shearograms are exposed under the same illumination and observation directions and the same shearing amount, the product $\partial w/\partial x$ and δx for different wavelengths but for constant setup geometry is [7]:

$$N_1(i,j)\lambda_1 = 2\delta x \frac{\partial w}{\partial x} = N_2(i,j)\lambda_2. \tag{2.53}$$

This statement requires either that we can assure to repeat exactly the same deformation under to consecutive tests (one for λ_1 and one for λ_2, or that the wavelengths can be shifted back and forth. Now, since $N_2 = N_1 + \delta N$ and $\lambda_2 = \lambda_1 + \delta\lambda$, one can obtain:

$$N_2 = -\delta N/\lambda_1/\delta\lambda) \tag{2.54}$$

thus obtaining the absolute fringe order to use for obtaining the absolute phase values. However, this method requires two lasers emitting two different wavelengths, or one laser unit containing a frequency modulator, which makes the shearographic setup more complex. There exists in literature other applications adopting multi-wavelength solutions for determining all the six in plane strain components, like the one presented in [32], which is based on simultaneous illumination of the object with three diode lasers that emit at different wavelengths between 800 and 850 nm. Wavelength separation and image acquisition are performed with a special optical arrangement, including narrow-band pass filters and three black-and-white cameras.

Fringe carrier method As for the Two-wavelength method, the absolute fringe order is determined by generating a second fringe pattern from the fringe order difference between the two patterns. The additional pattern is generated by a small movement of a single laser source or a lens expanding in a certain direction, which causes the fringe carriers. After the basic interferogram is stored, either the laser source or the expansion lens is moved for a small distance δL along the optical axis. Linear fringe carriers are created where the fringes are directed orthogonally to the shearing direction [7]. The relative phase difference Δ_1 caused by the movement of

the laser source will be:

$$\Delta_1 = \frac{2\pi\delta x}{\lambda} k_1 x \implies N_1(i,j)2\pi = \frac{2\pi\delta x}{\lambda} k_1 x. \tag{2.55}$$

Successively, the object is loaded, causing a new fringe pattern including the fringe carriers due to the movement of the optical element as well as the loading information is generated. The relative phase change Δ_2 is then the sum of Δ_1 which is due to the moved laser source, and Δ_b, which is due to the loading: $\Delta_2 = \Delta_1 + \Delta_b$, where: $\Delta_b = \left(\frac{4\pi\delta x}{\lambda}\right)\frac{\partial w}{\partial x}$. Consequently, Δ_2 is given by:

$$\Delta_2 = \Delta_1 + \Delta_b = \frac{2\pi\delta x}{\lambda}\Big(k_1 x + 2\frac{\partial w}{\partial x}\Big) = N_2(i,j)2\pi. \tag{2.56}$$

It is now possible to obtain Δ_b as:

$$\Delta_b = \frac{4\pi\delta x}{\lambda}\frac{\partial w}{\partial x} = 2\pi[N_2(i,j) - N_1(i,j)]. \tag{2.57}$$

Eq. 2.57 shows that the relative phase change caused by the load is not dependent on the absolute fringe order, but on the difference in the fringe order between the fringe carrier and the loading shearogram superimposed by the fringe carrier [7]. The disadvantage of this method lies in the complexity of the setup necessary for generating carrier fringes in industrial environment.

Zeroth order fringe localization It is now obvious that for determining the absolute phase, at least two different conditions are required. The method presented in this paragraph aims at localizing the zeroth order fringe, i.e. the region of the phase distribution corresponding to a zero surface displacement [33], by the use of different load applications. More precisely, two shearograms showing a very small difference in loading are exposed. The superimposition of such shearograms generates a shift in the fringes. The positions where fringes are not shifted represent the zeroth order fringe. This is because if the zeroth order fringe exists in a fringe pattern, then its position usually stays unchanged for two different loading in the elastic range of the material [7]. From this position, the subsequent fringe orders can be counted. At the end, it is worth to highlight the great constraint of this technique, lying in the assumption of the existence of the zeroth order fringe within

the investigation area. Actually, often this is not happening since it is only a small section of a large object. Therefore, when the fringe pattern does not include the zeroth order and the boundary conditions are unknown, other methods must be applied.

Linear fitting over small loading sub steps This method can be applied in cases when the increase of setup complexity associated to the two wavelength method and the fringe carrier method has to be avoided, and in cases where the zeroth order fringe is not inside the framed area too. The idea is to take the reference image before loading, then the structure is loaded, and a series of images is stored after loading with a given time interval between each other. The great assumption of the method is that the material's behavior is linear. In fact, the algorithm performs a linear fitting over time of the phase values of a chosen coordinate extracted from phase maps, in order to make a prediction of the phase pattern evolution even after the last acquisition instant. The assumption is that, the chosen point (as all the other points within the image), should be very close to the actual zero, as the material is returning to the reference condition. At that point, everything that should be left in the image is the unwrapping error. It is worth to make an example for a better explanation of the problem. In Fig. 2.15 the cooling steps of a PVC plate subjected to a thermal load are shown. In the framed area, two circular defects are present, as can be noticed by the fringe patterns visible from the maps. Consider now, for each image of Fig. 2.15 the interrogation line shown in Fig. 2.16a, for the cooling instants *t=1s, t=10s, t=20s* and consider also the corresponding wrapped and unwrapped phase profiles in Fig. 2.16b and 2.16c. It is possible to note that the peak-to-peak amplitude decreases as the cooling time increases, since the panel is re-approaching the undeformed state. At this point, the coordinate indicated by the black, dashed line in Fig. 2.16c, equal to 400 pixel, is chosen to be followed in time and to perform the linear fitting, as shown in Fig. 2.17. Thanks to the performed linear fit, it is possible to predict the panel behavior even beyond the acquisition time. It is up to the user to choose the last instant to monitor. In this case, for example, the acquisition time was *30 s* and the prediction was made up to four times the acquisition time, i.e. up to *120 s*. At this point, it is necessary to calculate two fundamental values, under the assumption that at the time when the plate is cooled completely, there should

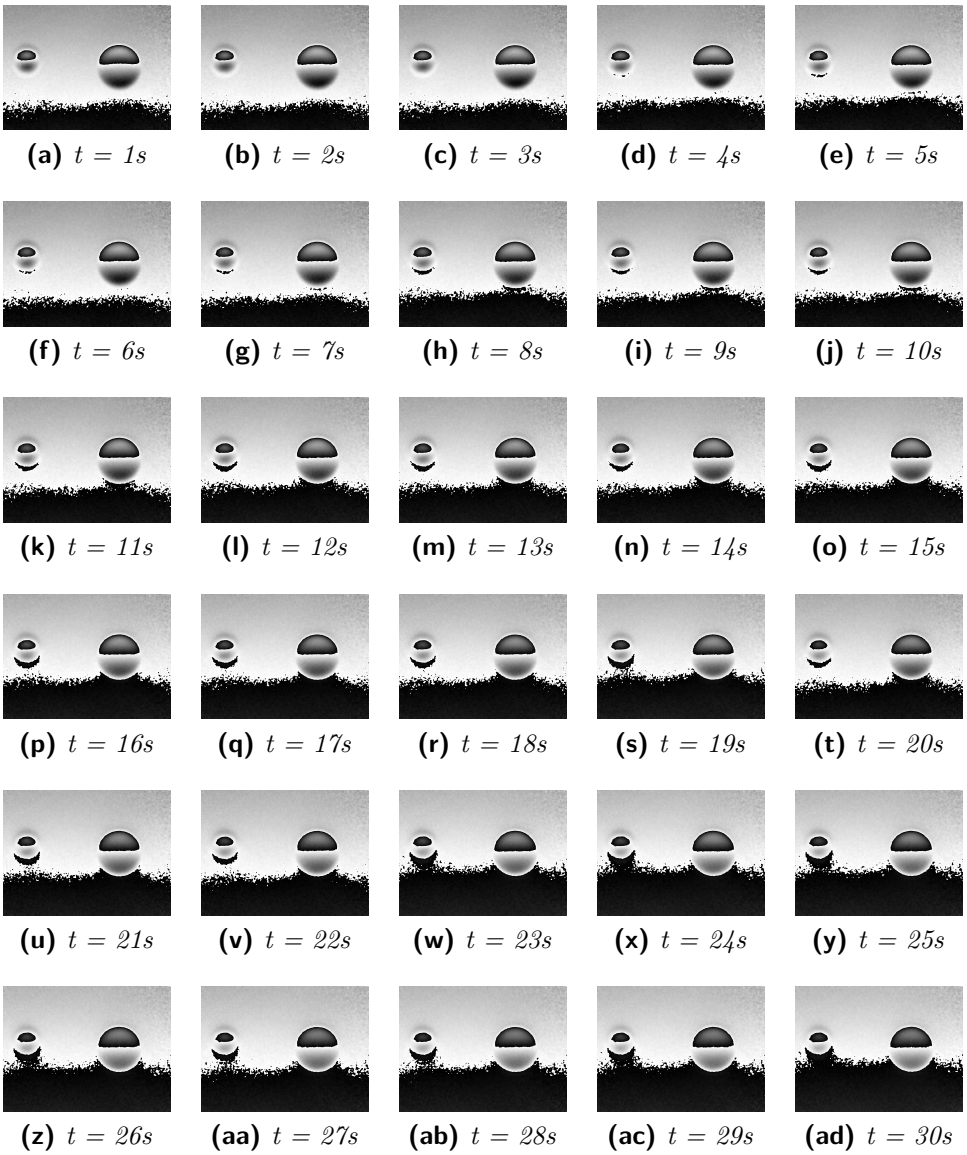

Figure 2.15: Phase maps corresponding to different cooling instants of a PVC test plate

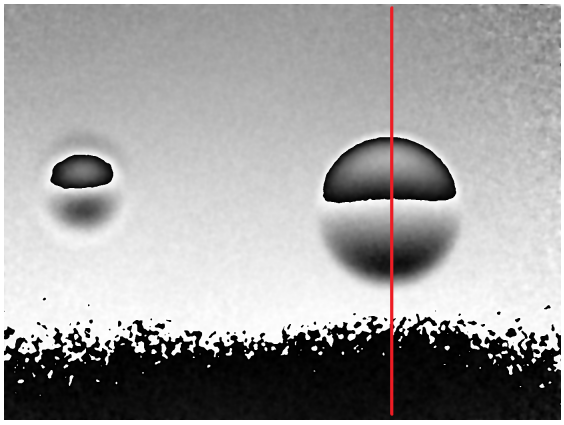

(a) *Line of interest extraction*

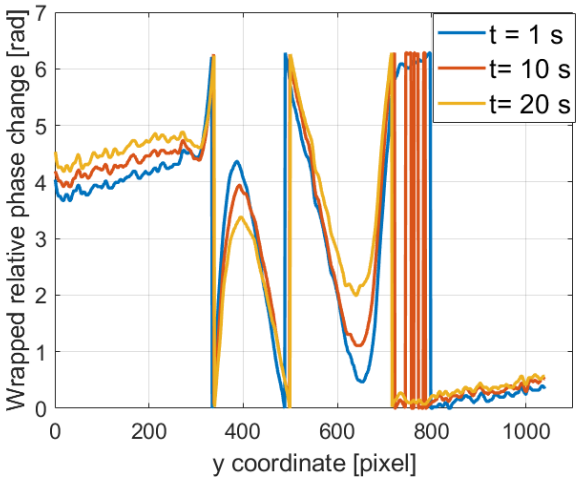

(b) *Wrapped profiles at different cooling instants*

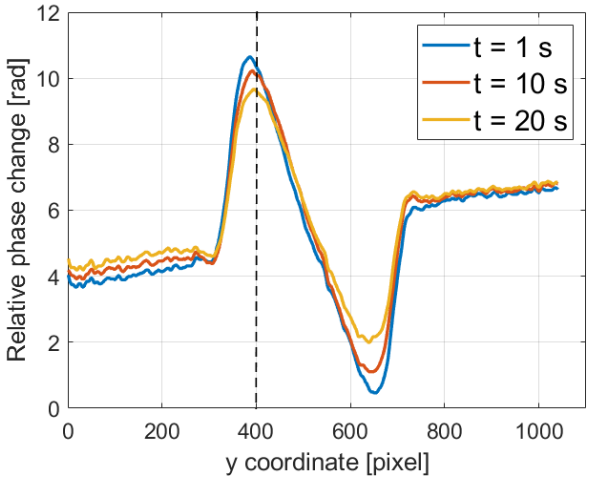

(c) *Unwrapped profiles at different cooling instants*

Figure 2.16: Extraction and unwrapping of phase profiles

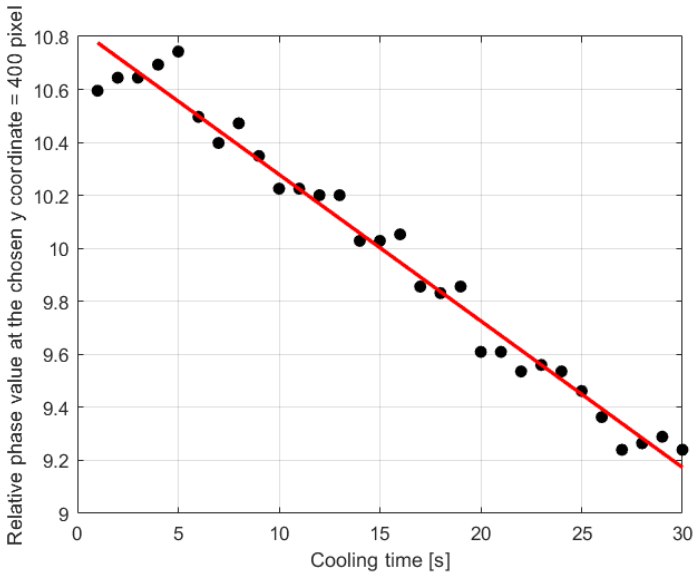

Figure 2.17: Evolution of the relative phase change at y coordinate = 400 pixel along the phase profiles extracted as in Fig. 2.16

be no deformation (as the deformation should go back to the same state as the reference image):

- the *average* value in our section at time t;
- *residuals*, defined as the squared distance between the actual value at a point in time and the *average*.

Now, for the assumption made above, the completely cooled state corresponds to the minimum of residuals. Everything that (in case of no measurement errors) should be left in the image is the unwrapping error. However, there will always be some spurious signals due to the many assumptions that has been taken. However, the average at the point where residual is minimized usually results a robust estimate of the error. This concepts are shown in Fig. 2.18, where the upper graph shows the residuals trend and highlights in red its minimum value, while the lower graph shows the instantaneous averaged in the chosen section. The average value corresponding to the instant when the minimum residual is detected, is a measure of the unwrapping error. In order to obtain the actual unwrapping error as multiple of 2π, the discussed value has to be rounded to the nearest 2π multiple. In this specific case, the detected unwrapping error was 2π.

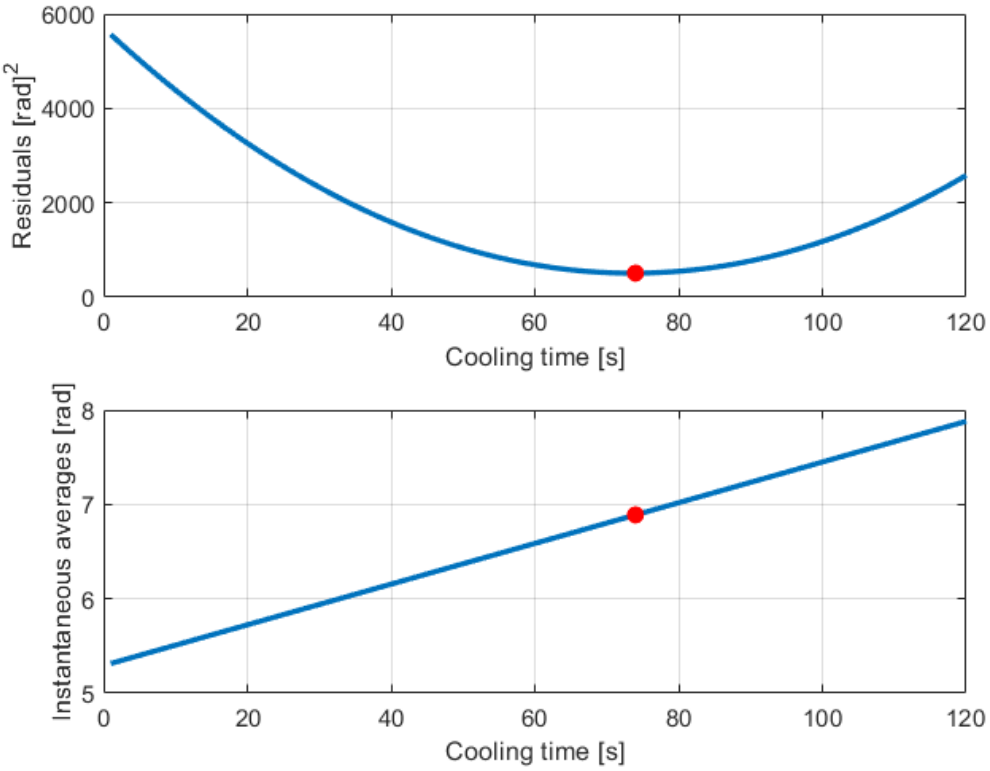

Figure 2.18: Residuals and instantaneous averages for the considered section. The conditions corresponding to the minimum of residuals are marked in red.

Adding and subtracting method The linear fitting method described in the previous paragraph enables to avoid modifications in the measurement setup but, as already mentioned, it has some limitations due to the needed assumptions. In addition to this, taking the reference image before loading, makes the stored phase maps much noisier because of saturation and turbulence phenomena occurring during load. In fact, even if no image is stored during load, those effects enhances differences between the reference map and the images acquired during the cooling phase, thus increasing the noise level inside the final phase maps. In order to overcome this problem, it is useful to take the reference image as soon as possible after loading, such that all the stored images are digitally subtracted to a reference taken in the same environmental condition. This reduces the incoming noise. However, if this strategy is adopted, the Linear Fitting method is excluded because, as cooling time increases, the phase maps become much more different with respect to the reference one that corresponds to the maximum temperature achieved by the structure. Consequently, residuals will be monotonically increasing and no minimum can be found. Therefore, another strategy has to be adopted in order to compute absolute phase when reference image is taken after loading. In this regard, in [34] the so called *Adding and Subtracting Method* is described. Actually, this method does not contribute to compute the constant C, i.e. the unwrapping error, expressed in Eq. 2.51. On the contrary it is a technique that avoids to perform the Unwrapping process itself, thus avoiding the unwrapping error as well. Like the Linear Fitting method, even for the current one the sample has to be loaded in small steps and a sequence of phase maps are calculated by subtracting consecutive maps of phase difference. More precisely, if Φ_i is the phase difference distribution discussed in Sec. 2.2.4 at instant t_i and Φ_{i-1} is the phase difference at instant t_{i-1}, the corresponding phase map can be expressed as:

$$\Delta\Phi_i = \Phi_i - \Phi_{i-1}. \tag{2.58}$$

This phase map is in the range $[-2\pi; 2\pi]$, hence a correction defined by Eq. 2.59 has to be performed to correct the range in $[-\pi; \pi]$:

$$\Delta\Phi_i = \begin{cases} \Delta\Phi_i & \text{if } -\pi \leq \Delta\Phi_i \leq \pi \\ \Delta\Phi_i - 2\pi & \text{if } \Delta\Phi_i > \pi \\ \Delta\Phi_i + 2\pi & \text{if } \Delta\Phi_i < -\pi. \end{cases} \tag{2.59}$$

The corrected phase map is then smoothed by one of the filtering techniques described in Sec. 2.2.6.1 and, after that, the cumulative phase map corresponding to the entire cooling process is obtained by adding all partial phase maps. In this way, phase unwrapping can be avoided if, and only if, the phase does not experience a variation outside the range $[-\pi; \pi]$ in each individual phase map $\Delta\Phi$. The latter statement is the only constraint associated to the method, that can be achieved by properly setting the frame rate in the acquisition of the cooling process.

Chapter 3

Shearography: state of the art

In Chapter 2 the main concepts on which Shearography measurements are founded, were explained. However, a deep literature study reveals that Shearography has still to face some important weaknesses. For example, as discussed in [35], in real applications the loading methods and parameters usually depend on the experience of the operator, which affects the effectiveness and accuracy of the test. Up to now, in fact, no criteria to choose the loading methods and parameters, have been reported in detail. Generally, three loading methods can be exploited to generate a deformation within the structure to inspect:

- mechanical load: exerted, for example, by a micrometer head to apply the force into the center of the specimen. The setup is simple and easy to operate. However, the contact loading method causes deformation of the entire specimen, which makes the defect information weakened and inconvenient to observe [35];

- thermal load: based on the different thermal sensitivity between the defect and the rest of the structure. Usually, high-power drier, infrared heater, halogen lamps, tungsten lamps, blowers, etc [35]-[36], are used, hence the setup is simple as well. However, some materials are not sensitive to temperature changes, making measurement less reliable;

- vacuum load: carried out by putting the specimen into a sealed box. The deformation of the defect will differ from surrounding parts because of pumping vacuum. The air pressure in the vacuum box can be controlled quantitatively

and easily. It is suitable for small specimen, and universal to various materials. The disadvantage is that the equipment is slightly complicated as a sealed box is needed [35].

In addition to loading methods, other parameters influencing Shearography performances about defect detection, have been already reported in Chapter 1 and are mainly: shear distance, observation distance, defect size and defect depth. It is useful to tackle these aspects by dividing the state of the art into three main categories:

1. current procedures;
2. software and models;
3. current devices;

Actually, items 1 and 2 are strictly connected, since a part of the current models for Shearography applications are developed as support for the implementation of procedures themselves, in terms of definition of optimal conditions. However, even now a lot of weaknesses limit their success about this purpose. In the following, the mentioned categories will be discussed individually. For each of these, the focus is put on thermal load applications, since as anticipated in Chapter 1 and as will be better discussed in the following sections, is the one with the highest lack of standard indications, the highest amount of uncertainty sources and, consequently, the lowest level of repeatability. All the work carried out in this Ph.D. thesis is focused on thermal load cases, in fact.

3.1 Current procedures

For the preparation of this Section an investigation about the measurement procedures suggested by the principal producers of these devices (Dantec Dynamics [36], Zeiss [37] , Isi-Sys [38]) was performed. In the following, the main outcoming aspects will be summarized. At first, it is important to highlight that all indications provided by producers about thermal load procedures are still strongly qualitative, while more repeatable systems are available for robotic applications using vacuum load. Here the Shearocamera is mounted on a robotic arm in conjunction with the

sealed box performing vacuum. This kind of systems is often exploited for tyre inspection [37]. On the contrary, for what concerns thermal load, many qualitative indications are provided by Dantec Dynamics that, for example made available on its website a study conducted on an aluminum-honeycomb black sample affected by debondings. The aim of the investigation was to study the effect of three different heating sources on defect detection:

- halogen lamps;
- tungsten lamps;
- blowers.

This study gave an estimation of the needed heating time, as well as the heating source varies:

- halogen emitter: 5 s;
- tungsten emitter: 10 s;
- blower: 20 s.

These indications have two huge limitations: they are related to a specific material and they are stated only considering the load that enabled to see fringes appearing. Thus, other elements have been added by the producer. For example, for metal-to-metal bonds a temperature difference of 0.5° C was enough to get clear defect indications. Higher temperatures resulted in larger deformations and slightly larger affected area (making the defects look bigger). Moreover, a temperature difference of approximately 5° C was enough to get defect indications from 1 mm skin + 0.8 mm doubler to core disbonds. In conclusion, larger panels gave faster cooling and less full body bending which affect the inspection quality in a positive direction. Another issue is the temperature gradient between the inspected object and the surrounding environment. If the temperature difference between the part and the ambient air exceeds 10° C, the measurements are disturbed. The laser fringes get very turbulent, due to air turbulence. Within the 10° C temperature range the increase and decrease of temperature was not affected by the initial temperature of the part. Moreover, the heat from the lamps themselves create air turbulence in front of the lamp even after switching the light off. This makes it necessary

to screen the source after the heating step. In the case of halogen lamps, it is not possible to make measurements while heating, if the involved wavelengths are not filtered out by the optics, making the Shearocamera saturate. Optical filters or lamps with light outside the wavelength area of the laser may allow heating during measurements. A further aspect lies in the reference image. Even in this regard, no standard indication is provided. Dantec Dynamics asserts that their trials showed that a higher sensitivity was achieved by taking the reference image after loading. On the other hand, in [39] the authors stated that it turned out to be essential for maintaining the low noise level, to use the last interferogram from the measurement series as the reference image. In [40], the reference image was taken as soon as possible after loading, while in [41] the following process was implemented: reference interferograms were first recorded, then after ten seconds, heating phase started. During the heating process no image was acquired. After 30 s the lamp was turned off and then every 5 s an image was captured. At the end, on the basis of the above considerations, Dantec Dynamics proposes the following, general, procedure:

1. 20 s heating, giving approximately 5° C temperature increase;
2. reference image immediately after loading;
3. the first measurement approximately 2 s later;
4. the second measurement approximately 10 s later;
5. third evaluated image another 10 s later and so on until no further change in temperature was achieved.

Furthermore, evaluation of when in time defect fringes are clearly visible gave information about the defect depth. In particular, defects between skin and doubler were clearly indicated already at stages 3 or 4. Defects between core and 1 mm skin + 1 mm doubler were not clearly indicated until stage 4 or 5. Defects in bond line between doubler were not indicated until stage 5.

It should be clear to the reader that all these indications are not quantitative at all, and are not enough to define an inspection cycle repeatable and standardized.

3.2 Software and models

Software and models oriented to support and/or complete Shearography inspections, can be classified into two different groups:

1. Numerical models to exploit as a support for measurement procedures in terms of determination of the measurement conditions for the specific test case;

2. Algorithms for defect size computation.

In the following, they will be deeply discussed one at a time.

3.2.1 Numerical models as support for measurement procedures

In literature, the efforts put on revealing the optimal measurement conditions for Shearography, are mostly based on numerical simulations rather than on live experimental data. This is the reason why the great part of the available models are able to make predictions only in cases of vacuum or mechanical load, being these solutions much more repeatable and controllable [35]. Thermal load, in fact, implies a series of effects difficult to simulate and predict, such as heat sensitivity, environmental absorption of the heating radiation, air turbulence generated by the radiation itself, temperature gradient between the inspected surface and the environment, etc. Actually, it is possible to find some works attempting to predict Shearography results and performances in cases of thermal load. In this regard, in [42] a numerical method was developed to simulate Shearographic fringe patterns using Finite Element Analysis (FEA) for the inspection of polymeric materials. This model was finally compared with experimental data. In the mentioned paper, the authors found that the displacement derivatives predicted by FEA are higher than those of experimental data, and this is just because of the attenuation effects exerted by the atmosphere towards heating radiation. This effects, as previously discussed, are hard to put inside a numerical model. Furthermore, another result described in [42] is that, increasing the depth of the defect to 1 mm from the framed surface decreases the fringe pattern quality and creates more mismatches between FEA and experiments. Consequently, FEA can model shearograms only for cases

where the defects are not deeper than 1 mm, and this is a huge limitation of these models. In the same paper, the authors give an estimation of the heating time to apply to the structure in terms of a cut-off line between the regions of visibility or non-visibility of fringes, without any attention to the reliability on the estimation of defect size. Moreover, in [41] a Finite-Element model of an aluminum flat plate is implemented to obtain the dynamic mechanical response of the sample under thermal loading. A very important issue that comes from this work is that, the definition of different boundary conditions for the part of the structure that is going to be framed by the Shearocamera, involves very different simulated fringe patterns. This adds to the model a great uncertainty source. What appears from the just described works is that, the implementation of a model makes the knowledge of the mechanical and thermal properties of the material, compulsory. Another aspect lies in the fact that the models do not search for the optimal measurement conditions basing on the optimization of the goodness of defect size estimation and morphological reconstruction. On the contrary, they work basically on optimizing the defect visibility, for example by increasing the shear distance, responsible of the system's sensitivity [35]. However, in a real case, the shear-distance increase causes an increase of incoming noise as well, making the defect characterization much worse. This element cannot be modeled, obviously. Another important issue that can be deduced is that the Finite Element Analysis available in literature for the prediction of Shearography performances are related to standard materials, rather than composite ones. Only in [35] the authors attempts to provide a model for composite materials, but they succeeded only for the case of vacuum load, so that it can be expected a non-negligible discrepancy with actual conditions in thermal load.

3.2.2 Algorithms for defect size computation

As anticipated in Chapter 1, in order to comply with the stringent acceptability requirements imposed by aerospace industry, Shearography data should be processed by means of robust algorithms able to both compute the defect size and to reconstruct its morphology. This will facilitate repair operations too. The theoretical dissertation provided in Chapter 2 makes it possible to understand that each object in the field of view of the Shearocamera results elongated due to the

shearing effect. The amount of the elongation coincides with the shearing amount. Consequently, the area of a detected defect framed by the Shearocamera will be the sum of the actual defect area and the excess area produced by the shearing effect. Hence, if for simplicity one considers one dimension only, and if this dimension is set along the shear direction, the actual defect size d can be computed as:

$$d = D - \delta x, \tag{3.1}$$

where D is the size of the defect elongated, and δx is the shearing amount. Equation 3.1 shows that, in order to perform a robust defect size estimation, both D and δx must be accurately determined. Obviously, since the most important information is the defect area, rather than its dimension along a certain direction, both the shear components in the image plane must be computed. However, in this regard, Shearography faces some problems. This technique, in fact, is usually used as a qualitative methodology because of the numerous uncertainty sources and the challenge of processing the outcoming phase maps to extract quantitative information about the defect. In particular, Shearography is affected by optical distortions, inaccurate placement of the shearing and phase-shifting mirrors, stability errors of setup components [15], each of these causing a diversification of the shear amount inside the outcoming phase images. In addition, accurately setting the shear along a sole established orientation could be very complicated, since an undesired component in the orthogonal direction always appears, affecting image processing. In the past, some works focused on obtaining more quantitative results, see for example [43]. For the same purpose, in [44], [45], [12] cross-correlation or digital speckle photography were performed to calculate shear dispersion. However, for this kind of techniques an adaptation of the Michelson interferometer is required to be able to divide the sheared and non-sheared specklegrams, which is not commercially feasible. In addition, Xie et al developed a novel polarised dual shearing direction spatial phase-shift digital shearography system to perform NDT along two orthogonal sensitivity directions simultaneously [46]. Furthermore, in [15] the authors developed some correction procedures to consider both the undesired shear contribution and the optical distortions in shear computation. The calibration maps proposed in [15] are well-founded only for a certain collection of Shearography camera parameters, and, as the shear amount varies, a systematic

variability occurs. In addition, they require a precise laboratory setup to obtain a 5% decrease in gradient discrepancies , and in any case no information about amelioration in defect size computation is given. Moreover, with regards to phase map processing aiming at defect characterisation, Michel et al [47] exploited the Wavelet method for identifying defect edges considering a global shear level. In [47] the length of the phase profile crossing the maximum phase value in the dominant shear direction was obtained by means of a Wavelet Transform algorithm. In particular, the profile length was revealed by the convergence of the paths of the external local maxima of the wavelet coefficients . The problem is that, if the line associated with the maximum detected does not coincide with the longer phase profile and the shear does not have a sole fixed direction, the actual defect size cannot be determined. Furthermore, in the case of a complex-shaped defect, the defect will not stand along a favored orientation, therefore, to estimate its area, it is necessary to observe the defect in all directions, independently of the shear one.

3.3 Current devices

The evolution of Shearography systems and devices over time involved mostly software interfaces rather than new hardware solutions. In particular, only the more recent devices possess the possibility of triggering the acquisition with the heating lamps and to determine the acquisition rate. The motivation of this statement does not lie in the complexity of implementing such tools in the past years, but on the typical use of the technique itself. In fact, for a qualitative use, a live observation of the phase maps is sufficient, in conjunction with a manual control of the lamp(s). Thus, the choice in the past of not including unnecessary tools within Shearography software. Another recent update was the possibility of accessing raw data: older devices and corresponding acquisition software permit to save the phase maps as images (.bmp, .jpg, .tiff, .png formats) already smoothed by mostly simple median filters. This causes loss of information and makes a quantitative study more difficult. Nowadays, because of the need of more standardized procedures, these functions are going to be added to current software. However, since over time hardware components were not modified, users already supplied with a Shearography hardware, are not intended to buy newer systems: just a software update would be sufficient. Unfortunately, these updates

are very expensive and not all of them are compatible with older devices.

Chapter 4

Development of a repeatable, quantitative measurement procedure for Shearography Inspection

As anticipated in Chapter 1, the aim of this work is to provide Shearography user with a repeatable procedure able to perform a reliable defect characterization. For doing this, the limits discussed in Chapter 3 for applications involving thermal load, must be overcome. This objective was achieved in this Ph.D. work. In particular, the study was organized according to the following work packages:

1. design and implementation of a proper algorithm for defect size and morphology estimation;

2. design and equipment of a computerized measurement setup, aiming at reducing some of the uncertainty sources described in Chapter 3;

3. definition of a measurement procedure both for data acquisition phase and analysis, that takes into account the variability of the technique's behavior with measurement parameters.

The developed procedure, mentioned in item 3, can be either performed on a test panel of the same material as the one of the structure to be inspected, or repeated

each time an inspection has to take place. In the first case, in the test panel, a series of known defects (in terms of shape, size and depth) will be artificially produced, and the procedure is aimed at defining the optimal conditions for correctly detecting a given defect. Consequently, this is useful only in cases where the user has an idea about the possible defects affecting the structure. In any case, errors can be made because of differences between the test panel and the actual structure. Thus, for applications where the user cannot make predictions about the encountered damages, it is recommended to repeat the procedure on the structure to inspect itself. This will ensure a higher reliability of results. In this work, the methodology was developed by using a PVC test panel with known defects, as PVC has a good thermal behavior, thus facilitating the study. In the next Chapter, then, the methodology will be furtherly applied on real composites. The work packages listed above, will be deeply discussed individually in the following Sections.

4.1 Design and implementation of a proper algorithm for defect size and morphology estimation

Defect size and shape reconstruction were achieved in this work by an algorithm that has been called *Wavelet Transform Angular Scanning*. The issue of shear variability discussed in Sec. 3.2.2 was overcome by calculating the local shear using a sub-pixel interpolation with a certified calibration target, previously "cropped" by selecting the Region Of Interest (ROI) [43] matching the fringe pattern area. The main steps of the algorithm can be categorized in:

1. Data encoding and phase computation;
2. Distortion correction;
3. Local shear computation;
4. Phase-map Filtering and Unwrapping;
5. Phase-map Thresholding;
6. Wavelet Transform Scanning plus Structural Intensity distribution analysis;

7. Defect area evaluation.

4.1.1 Data encoding and phase computation

The Shearography system used for this work is supplied by Dantec Dynamics, and the corresponding acquisition software is Istra4D. As already discussed in Sec. 3.3, only the more recent, expensive solutions provide the user with the possibility of accessing raw data. In order to overcome this problem, some efforts were put in encoding the *.hdf5* files automatically generated by the Istra4D software during acquisition. This was achieved thanks to some Matlab libraries able to read this hierarchical file, that was found to contain a great amount of information. More precisely, the Istra4D software generates a *.hdf5* file for each acquired phase-map. Each file was discovered to contain the four images, corresponding to speckle images I_i necessary for the computation of the phase-relation map Φ_i, as expressed in Eq. 2.44. The possibility of disposing of this upstream data, unlocked the possibility of implementing specific correction methods, like the one presented in Sec. 4.1.2, before phase computation, so that the phase information will be much more reliable than the one saved as image by commercial software. Furthermore, disposing of Φ_i and not directly of Δ, enabled also to implement the Adding and Subtracting method described in Sec. 2.2.6.2.

4.1.2 Distortion correction

The used system revealed to be affected by barrel distortions. It is important to balance this effect no to commit errors in the defect reconstruction. For this purpose, apposite Matlab libraries were used. This libraries require to use a checkboard target and to know the actual size of squares. Hence, such target has to be put within the field of view of the Shearocamera, and the shear has to be set to zero, in order not to bring the distortion tool to commit errors due to the presence of sheared and non-sheared squares. An example of this dewarping is shown in Fig. 4.1. Such a correction has to be performed on each of the four images I_i of Eq. 2.44 because, if it was applied to the final phase map Δ, the dewarping process, involving translations of some part of the image, would introduce dummy fringes. This would certainly cause problems in the successive Unwrapping process and in the integrity of the phase information as well.

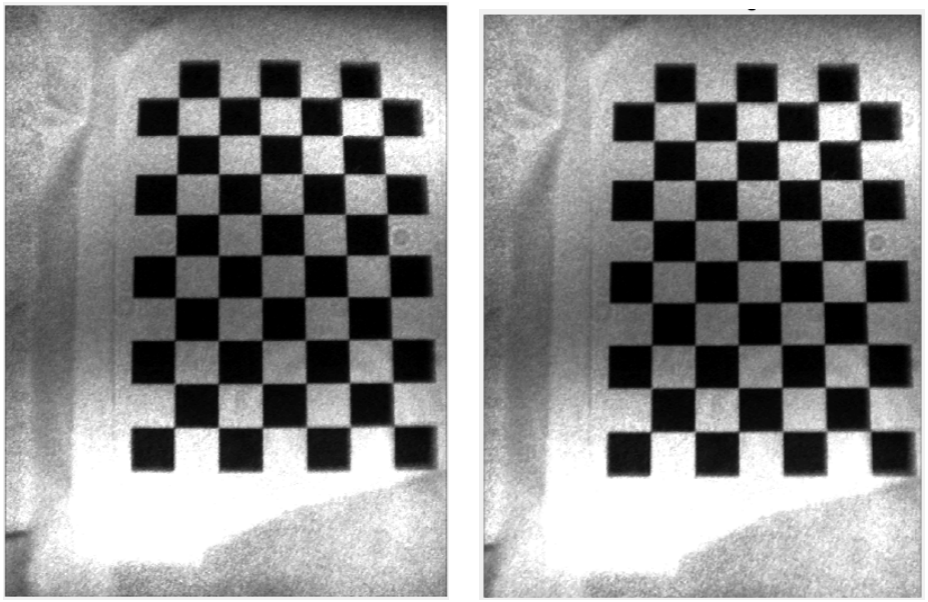

(a) *Distorted image* **(b)** *Undistorted image*

Figure 4.1: Barrel-distortion correction

4.1.3 Local shear computation

The first aspect to tackle is to identify the geometrical contribution of the shear diversification across the image. To this aim and to measure the x and y shear components, a certified pattern of black circles forming a 150 × 150 mm square on a white background (Fig. 4.2a) is used. The certification is made by "Edmund Industrial Optics". Product Number is 46249 and Serial Number is 0000-0231. The target grid accuracy is ±0.2 mm corner to corner, while the dot size accuracy is ±0.13 mm. Dot to dot distance is 6 mm for the bigger dots (Fig. 4.2a), with an accuracy of ±0.008 mm. Hence, once a fringe pattern is detected, it is then necessary to identify, inside the target, a Region of Interest (Fig. 4.2a), lying in correspondence of the above-mentioned fringe pattern (Fig. 4.2b) and compute the shear mean values inside such region, rather than inside the entire image. In this way, the quantity to be subtracted to the phase profile length is more precise. In particular, the sheared target acquired by the Shearocamera is processed in Matlab environment by the use of image analysis tools as: median filtering, Niblack threshold [48] supported by morphological operators (erosion, dilatation, opening, closing) and a circle detection phase. The mean distance between centers

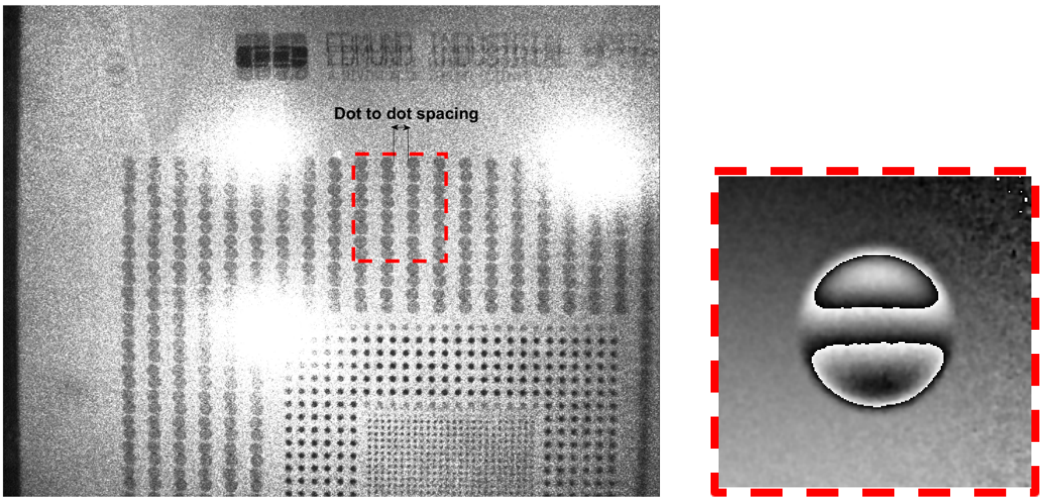

(a) *Certified calibration target framed by Shearography (the shear has already been set to 3 mm) where a Region of Interest is defined in correspondence of the detected fringe pattern*

(b) *Chosen Region of Interest (ROI)*

Figure 4.2: Choice of a localized ROI

of detected pairs of sheared and non-sheared circles corresponds to the shearing amount, both in x and y components. Moreover, the mean radius of the mentioned circles is used for image calibration, i.e. for the computation of the pixel/area ratio, so as to convert from $pixel^2$ to mm^2 for area definition. An example of this circle detection is reported in Fig. 4.3. Here the image is divided in sub-areas, each one characterized by a pair of sheared and non-sheared circles.

4.1.4 Phase-map Filtering and Unwrapping

As discussed in Sec. 2.2.6.1 and 2.2.6.2, a robust filtering process is fundamental for the success of the Unwrapping one, since the performances of the latter are strictly related to the noise level within the image. The assumption for a good Unwrapping, in fact, is that the phase-field has no rotational components. The sine-cosine filter described in Sec. 2.2.6.1 was chosen since it allows to perform a great number of iterations (of the order of 30-50 iterations) without losing the phase information, since the phase itself is recomputed at the end of each iteration, from the smoothed sine and cosine images. In this work, a smoothing kernel of size 4×4 acting for 30 iterations was exploited. Despite knowing the advantages of using anisotropic

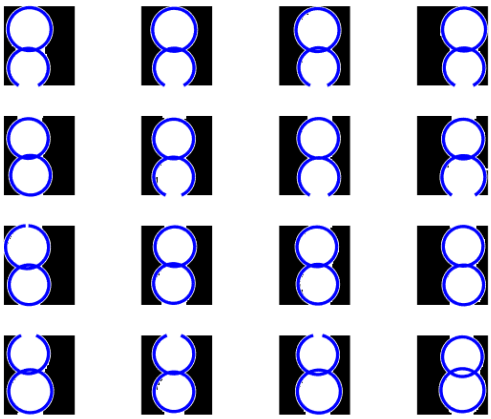

Figure 4.3: Circle detection for image calibration and shear computation

kernels (see Sec. 2.2.6.1) in terms of phase retrieval, it results more suitable to use a squared kernel, if the scope is a robust defect size and morphology reconstruction. The adoption of a rectangular kernel, in fact, would warp the defect because of the anisotropic effect itself. It is better, than, to act in the same way in both directions for not playing a role in geometrical artifacts. An example of a resulting image after the filter application is reported in Fig. 4.4. For what concerns Phase-Unwrapping, the Goldenstein algorithm explained in Sec. 2.2.6.2 was chosen for its robustness in acting even in cases of residual rotational components in the phase field.

4.1.5 Phase-map Thresholding

To carry out the defect scanning discussed in the following Section, a thresholding process for centroid detection was required. The thresholded image is then needed to be further exploited to determine the defect area to be compared with the one obtained by the algorithm developed. It is clear that a manual threshold was not suitable for the study presented, since it would not provide sufficient robustness. The attention was therefore focused on automatic thresholding methods, i.e. the Entropy based [49]-[50], the Inter-Class Variance [51], the Niblack [48] and the Moments [52] methods. The study was conducted on a defect that was artificially created on a PVC specimen by a milling machine with centesimal resolution. Fig. 4.5 shows a comparison between the above-mentioned methods when applied

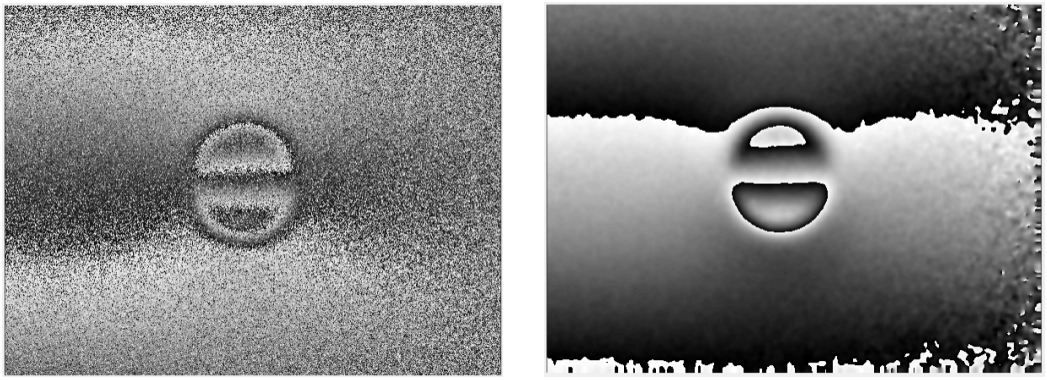

(a) *Original Speckled image*

(b) *Image filtered by a* 4×4 *kernel with 30 iterations*

Figure 4.4: Example of filtering

to a typical Shearography phase map. The first row of Fig. 4.5 contains the raw thresholding results, while the second row shows the final binarised images obtained after the application of morphological operators and/or Lookup tables. This further step is usually essential for deleting spurious detected objects. Since every defect has a dark and a bright side after unwrapping, the thresholding process was carried out in three steps. The first step is to look for the bright side (Fig. 4.5a), then the dark side is detected (Fig. 4.5a) and, finally, the two results are added so as to obtain a logical image containing the two lobes of the defect. The only method that does not require these multiple steps is Inter-class Variance (Fig. 4.5d), since in this case the addition of the complementary thresholded array would provide a completely white image. By applying different image processing techniques for the determination of the defect diameter, the first consideration is that the Entropy based threshold method (Fig. 4.5a) requires less operations (the image in the first row of Fig. 4.5a is identical to the one in the second row) compared to the others, for which background removal (Fig. 4.5b), Lookup Tables (Fig. 4.5c), and high sensitive-circle detection (Fig. 4.5c, Fig. 4.5d) are necessary. A set of 21 phase maps was stored and processed by using all the above- mentioned thresholding methods and the mean diameters for each threshold were calculated by subtracting the shear amount to the dimensions revealed by image processing. Results are shown in Fig. 4.6, where it is possible to observe that all the resulting automatic threshold techniques underestimate the actual defect size, but the degree of underestimation

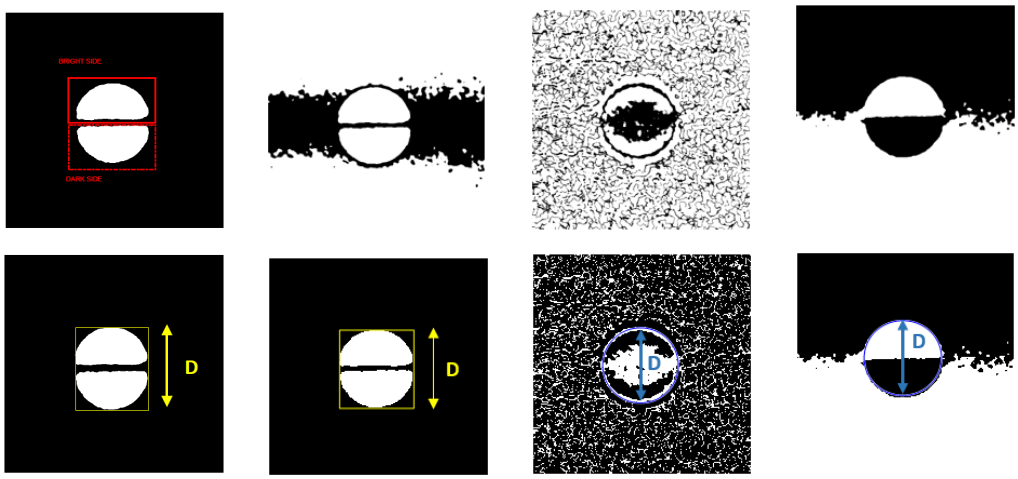

(a) *Entropy-based threshold* **(b)** *Moments-based threshold* **(c)** *Niblack threshold* **(d)** *Interclass-variance threshold*

Figure 4.5: Automatic thresholding methods applied on a typical Shearography phase-map containing a defect.

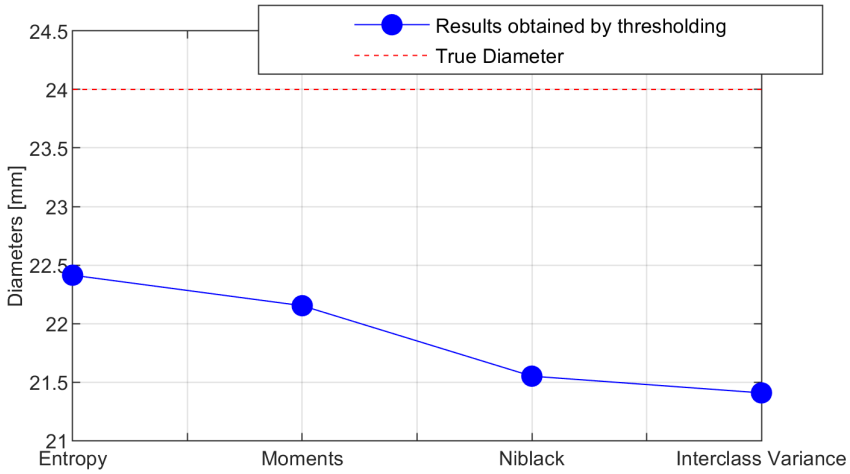

Figure 4.6: Mean diameters evaluated on 21 images by using all automatic thresholding methods

is lower with the entropy based-method. For these reasons, the latter was used both as a support for the Wavelet Transform based-algorithm discussed in the following sections and as a comparative measurement.

4.1.6 Wavelet Transform Scanning plus Structural Intensity distribution analysis

Fig. 2.14b represents a typical defect profile obtained by selecting a line in the middle of Fig. 2.14a. Given this profile, the issue is to find an automatic method to determine the actual position of the defect boundaries. Since, as discussed in Sec. 4.1.5, none of the main automatic thresholding processes is able to correctly estimate actual defect size, another methodology was investigated. In particular, the Wavelet Transform method was implemented on angled phase profiles whose center is the image centroid, thus scanning the overall defect area. As already mentioned in Sec. 3.2.2, defect size is usually computed by extracting the phase profile crossing the maximum phase value along the shear direction [47], since it is associated to the best Signal-to-Noise Ratio (SNR). However, it can be deduced that, iterating the same process for the entire image, i.e. performing a shear-directed scanning, could lead to lower Signal-to-Noise Ratios in correspondence of external phase profiles and cause outliers and loss of data in turn (Fig. 4.7). In particular, 180 lines crossing the centroid with an angular spacing of 1° were extracted and the corresponding grey levels at the intersections with the pixel array were computed by a sub-pixel analysis. The Wavelet Transform was then applied to each profile. This methodology is based on the detection of signal singularities by following the propagation across scales of the modulus maxima of its continuous Wavelet Transform. However, false singularities can be detected due to noise, it is thus necessary to select only the dominant ones. For this purpose, in [47] a cut-off frequency was set to filter the paths of local maxima, while in [53] the filtering process was performed using some Signal to Noise Ratio-based elaborations. For Shearography applications,the insight study performed during this work revealed that such methods are not completely valid for the angularly-extracted sets of phase profiles, due to their inability to univocally threshold the local maxima of the Wavelet coefficients of all the profiles. Hence, it was chosen to exploit the methodology developed by Bigot in [54]. Bigot introduced a new

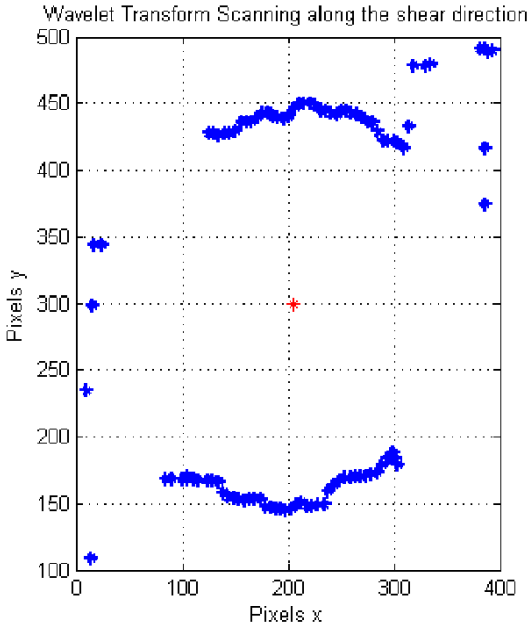

Figure 4.7: Scanning result along the shear direction

tool, named *Structural Intensity*, to identify the singularities of a noise affected signal. This parameter calculates the "density" of the modulus maxima of a wavelet representation along different scales, while the dominant modes of the outcoming structural intensity correspond to the actual signal singularities. In the following, the mathematical formulation of this parameter is shown. The wavelet function corresponding to r vanishing moments is defined supposing that the wavelet γ has a fast decay, which implies that there exists a ρ with a fast decay such that:

$$\gamma(u) = (-1)^r \frac{d^r \rho_(u)}{dt^r} \ and \ \int_{-\inf}^{+\inf} \rho(u)du \neq 0. \tag{4.1}$$

At a given scale $s > 0$, the continuous wavelet transform of a function $\in L^2(\mathbb{R})$ is:

$$W_s(f)(x) = \int_{-\inf}^{+\inf} f(u)\gamma_s(u-x)du. \tag{4.2}$$

It is now assumed that $\gamma = (-1)^r \rho(x)^r, r \geq 1$, such that $\rho(x) \geq 0$, for the coordinate $x \in \mathbb{R}$. If it is supposed that there exist q wavelet maxima lines $n_i(s)$ which converge, respectively, to $x_i \in \mathbb{R}, i = 1..., q$, as s tends to 0, and two constants

$\epsilon > 0$ and $G > 0$, such that $\rho(x) \geq \rho(G+\epsilon) > 0$ for all $x \in [-G-\epsilon; G+\epsilon]$ and that $\mid n_i(s) - x_i \mid \leq G$, $s = 1, ..., q$, for $x \in (R)$, the Structural Intensity of the Wavelet Maxima $SI_n(x)$ is defined as:

$$SI_n(x) = \sum_{i=1}^{q} \int_0^{l_{mi}} \frac{1}{s} \rho\Big(\frac{x - n_i(s)}{s}\Big) ds, \tag{4.3}$$

where $[0; l_{mi}]$ is the support of the lines $n_i(s)$ in the time-scale plane. More details about these definitions can be found in [54]. Despite its non parametric nature, the method developed by Bigot still requires the definition of some hyperparameters, i.e. the number of vanishing moments r and the minimum excess of mass m0 of each mode. To detect the boundaries of the extracted interrogation lines, a Gaussian Wavelet with r=2, equivalent to a Mexican Hat Wavelet, was used, such that the wavelet coefficients were related to the signal curvatures [47]. The definitions of excess mass are, instead, given in [55],[56]. Here it is worth just to precise that the strength of each mode of a generic density distribution (like Structural Intensity) is measured as its mass m, denoted by the areas under the curve lying between the local maxima considered and the corresponding local minima, see Fig. 4.8, extracted from [55]. By imposing a minimum excess mass level m_0, the weaker singularities that are most likely associated to noise are effectively discarded. The effects of choosing a different minimum excess mass for boundary selection are illustrated in Fig. 4.9, where the authors reported an example using m_0 values with an order of magnitude difference between them. In the figure, the square markers represent the singularities with an excess mass higher than the imposed minimum m_0, (where $m_0 = 0.003$ in Fig. 4.9a and $m_0 = 0.01$ in Fig. 4.9b),while the stars represent the singularities with $m < m_0$. The actual defect boundaries are detected as located in correspondence of the outer square-marked peaks. Hence, in Fig. 4.9 it is possible to notice that, by increasing m_0 stronger singularities, characterized by larger areas under the curve between the corresponding local maxima and their own local minima, can be found. To identify the right singularities, the authors set $m_0 = 0.003$, according to [55]. Even if $m_0 = 0.003$ is not the optimal value for the single image, it was verified that this datum is suitable for detection in all test conditions. In particular, to evaluate the m_0 effect on size estimation, a set of fourteen different phase maps obtained by applying different thermal loads to a 24 mm defect, observed from different distances, was considered. The m_0 value

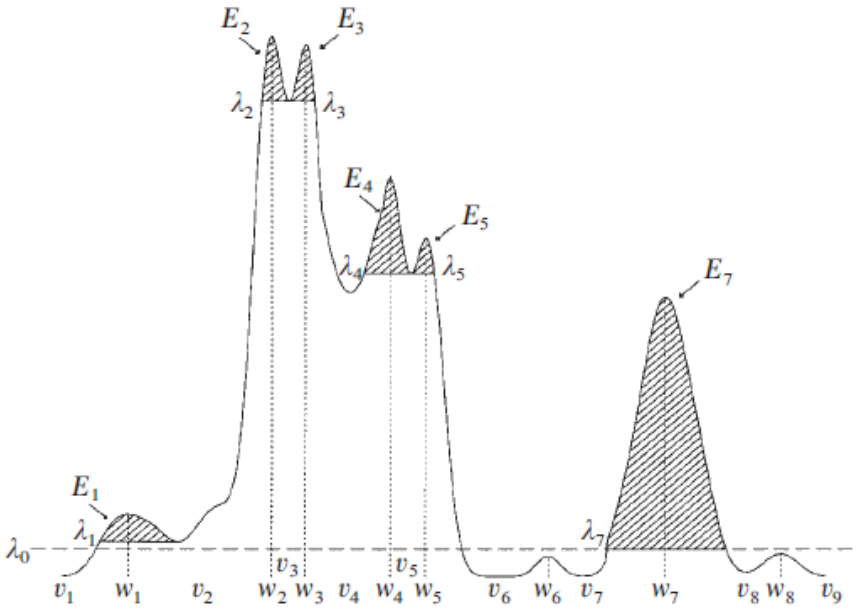

Figure 4.8: Excess mass graphical definition for a generic density distribution

was changed in a range of $[0.001; 0.01]$ using a 0.001 angular distance. In Fig. 4.10 shows the mean diameters and the related error bar evaluated for each m_0. This graph shows not only that, generally, 0.003 is the value corresponding to the best diameter estimation, but also that it is related to the smallest standard deviation of results, providing a higher detection robustness. Thus, it can be used as a standard input value for Shearography phase map elaboration. The goodness of this value were also tested on another material, i.e. a sandwich composite, affected by a sub superficial delamination characterized by an irregular shape. As the delamination size were unknown, an Ultrasound inspection were performed. This case study will be discussed more deeply in the next Chapter. Here we take only the equivalent diameter of the delamination obtained by Ultrasound inspection, as reference value. Fig. 4.11 shows that composite and PVC results have the very same trend with m_0. This means that the choice of this parameter does not depend on the material or on defect geometry. The graphs of Fig. 4.9 and 4.11 can be physically explained too. Taken $m_0 = 0.003$ as general, optimal value, the defect appears overestimated for $m < m_0$ since a more conservative check is being performed, meaning that the chosen boundaries lies in the background. On the

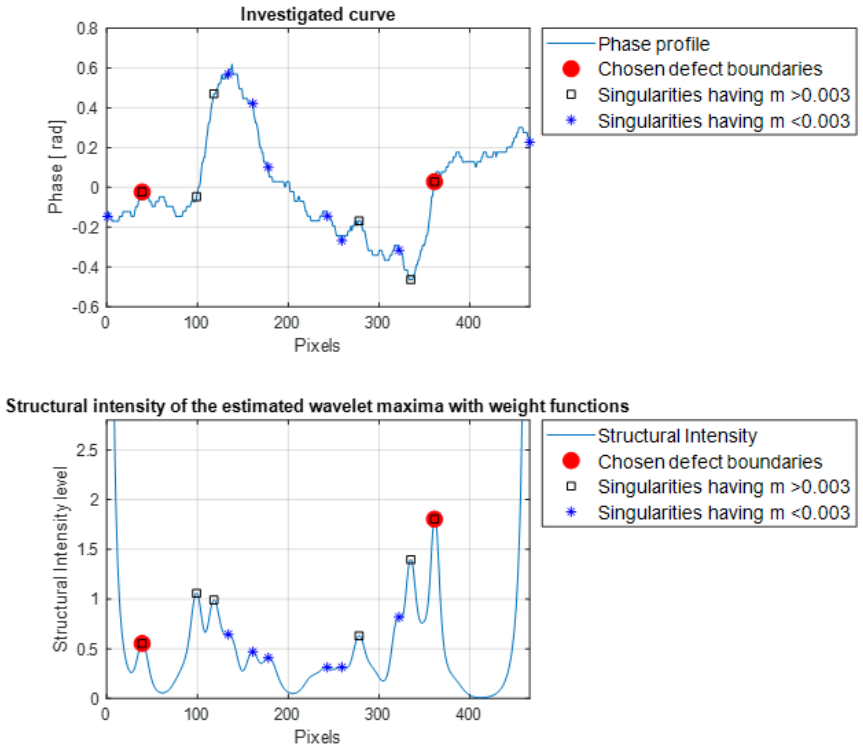

(a) $m_0 = 0.003$

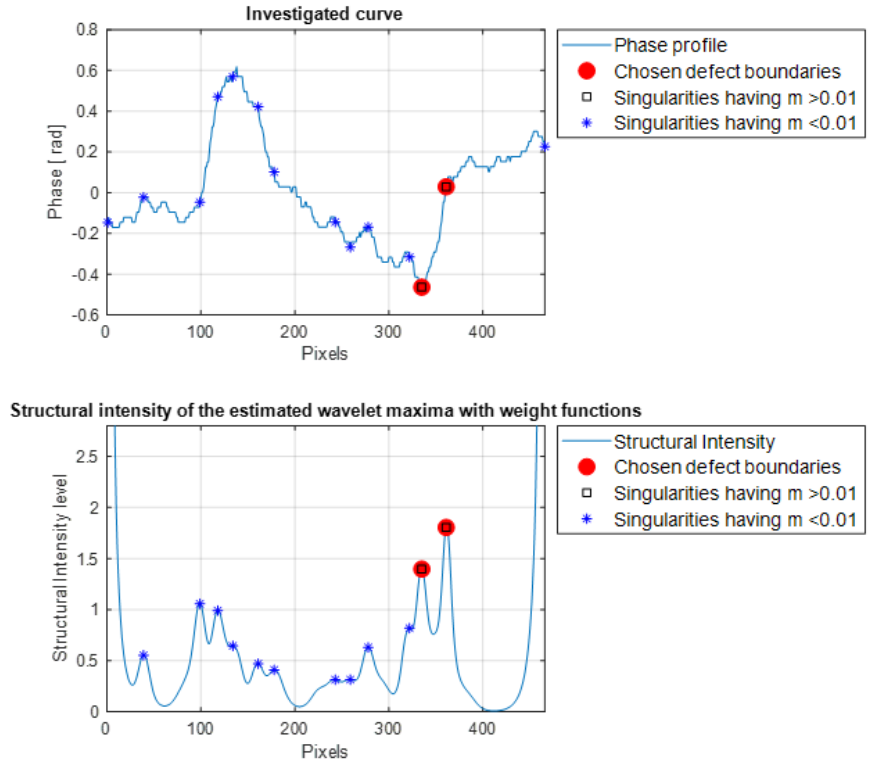

(b) $m_0 = 0.01$

Figure 4.9: Effect of choosing different values for m_0

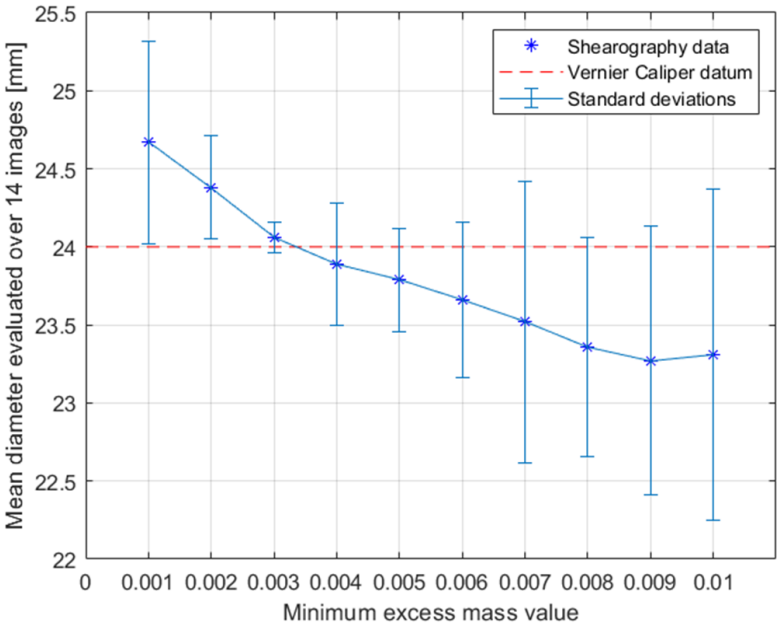

Figure 4.10: Calibration with respect to the maximum excess mass value for a PVC specimen

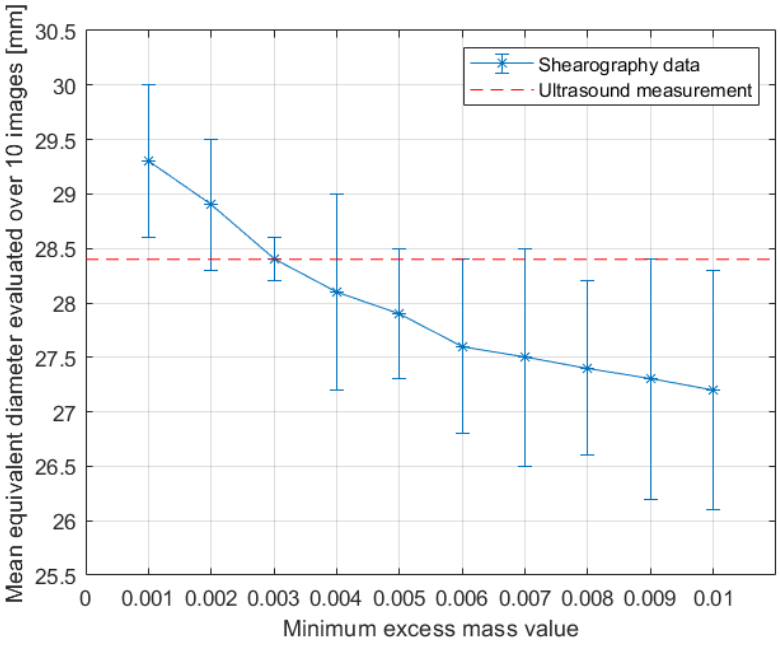

Figure 4.11: Calibration with respect to the maximum excess mass value for a sandwich composite specimen

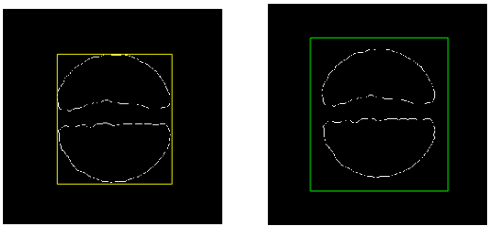

(a) *The smallest rectangle including the binarised defect*

(b) *The rectangle significantly larger (i.e. 20%) than 4.12a) used as a mask*

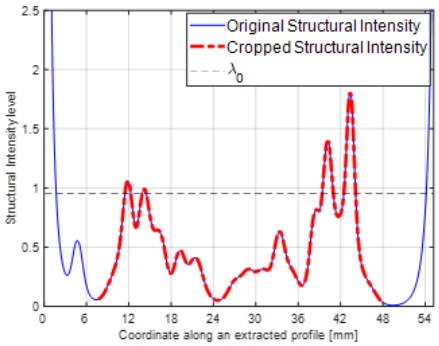

(c) *Cropped Structural Intensity for the definition of* λ_0

Figure 4.12: Work flow for the definition of the adaptive threshold $\lambda 0$

contrary, for $m > m_0$ the selection is more severe, and the case of Fig. 4.9b occurs, meaning that the chosen boundaries lie inside the actual ones, thus underestimating the actual size. In order to improve investigation accuracy, the authors drew inspiration from the method proposed in [55], which combines the minimum excess mass choice with an absolute threshold λ_0 of the Structural Intensity distribution, already anticipated by Fig. 4.9. This threshold was automatically set by defining the smallest bounding box (Fig. 4.12a) containing the thresholded defect (obtained by the Entropy-based method described in Sec. 4.1.5) and identifying a rectangle significantly larger than the same bounding box (Fig. 4.12b), so as to be sure not to exclude the boundaries from this selection (since it was demonstrated that thresholding processes underestimate defects). At this point, the rectangle defined was used to cut the Structural Intensity distributions (Fig. 4.12c), in which the minimum value of the outer modes was defined as λ_0 (Fig. 4.12c). Hence, the combined coded choice of m_0 and λ_0, enabled the exact selection of the right modes throughout the ROI, as it can be seen in Fig. 4.13, which shows a comparison between the results obtained by not selecting an adaptive threshold (Fig. 4.13a) and the improved version of the algorithm resulting from the adaptive threshold and the choice of the excess mass value (Fig. 4.13b) here described. In Fig. 4.13b a significant reduction in outliers and loss of data can be appreciated, which proves

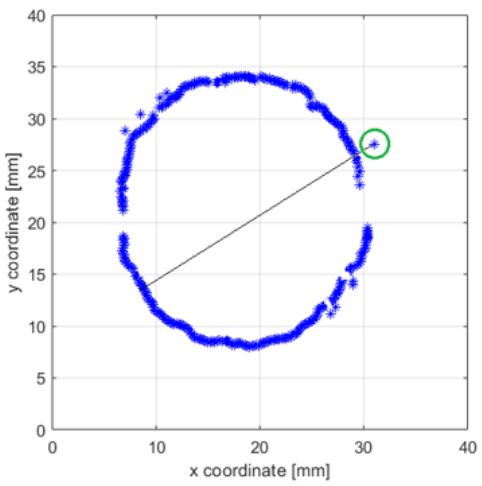

(a) *Results obtained by not using the adaptive threshold (the shearing effect is still present)*

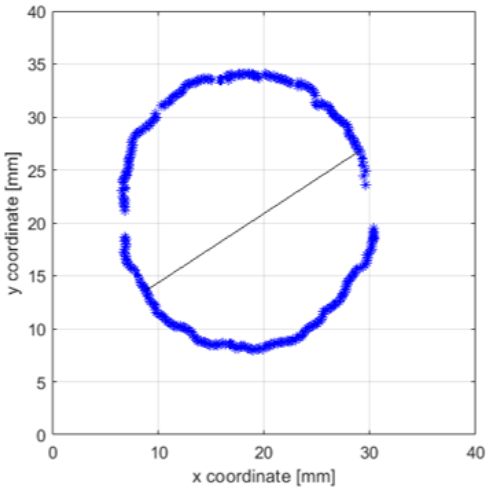

(b) *Results obtained through adaptive threshold selection (the shearing effect is still present)*

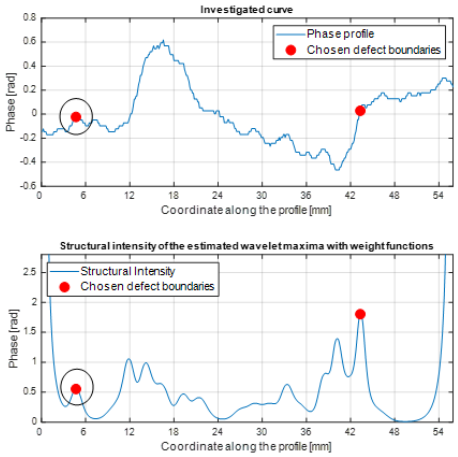

(c) *Profile processed without defining the adaptive threshold*

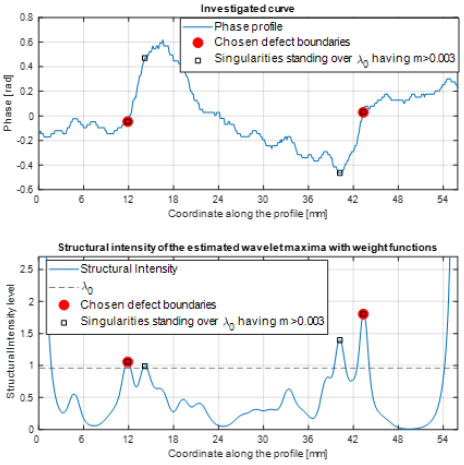

(d) *Profile processed by combining the choice of m0 with the adaptive threshold*

Figure 4.13: Comparison of the results obtained with and without threshold selection

the effectiveness of the approach presented. In particular, if the interrogation line in Fig. 4.13a and Fig. 4.13b is extracted, it is possible to appreciate that, by defining λ_0, the authors were able to discard the error circled in Fig. 4.13a and Fig. 4.13c, since the associated singularity was beneath λ_0 (Fig. 4.13d).

4.1.7 Defect area evaluation

Once all the damage boundaries are detected, a shear-subtracted plot highlighting the defect size and shape can be generated (in this regard, it should be recalled that Shearography-detected defect dimensions equal the sum of the defect dimensions and the shearing amount, as described in Sec. 3.2.2). In particular, the area was evaluated thanks to the Matlab function *polyarea*. This makes it possible to strengthen the morphological and dimensional control of a defect undergoing an increasing load, in addition to obtaining information about the defect along a desired direction chosen by the user in a real application.

4.2 Design and equipment of a computerized measurement setup

This work package aimed at overcoming the limits discussed in Sec. 3.1 and 3.3 thanks to the design of a proper measurement setup, whose scheme is reported in Fig. 4.15. In the following, the main goals of this package are summarized.

1. Controlling the switch-on and switch-off: a HID relay was exploited for this purpose.

2. Screening off the lamps after loading in order to avoid air turbulence and undesired residual radiations: a proper structure for housing two shutters, one for each heating lamp were prototyped (Fig. 4.14b). These shutters are kept in position by two electromagnets (Fig. 4.14a) controlled by a second HID relay. The shutters are released after lamps switch-off thanks to the relay itself, that opens the circuit in such a way that the electromagnets are no longer powered.

3. Controlling the thermal behavior of the inspected object: this item was useful just for achieving an overall knowledge of the physics of the problem, as a support for the development of the procedure discussed in the next Section.

4. Triggering the acquisition and defining the frame rate: as discussed in Sec. 3.3, the qualitative use of the technique didn't bring producers, in the past, to introduce these functionalities within the acquisition software. Nowadays, users already provided with older devices, are confident with their hardware but, for a quantitative use, they would be forced to spend a lot of money for software updates.

The solution studied for this Ph.D. thesis offers a universal package, developed in Labview environment, that can be integrated within the possessed system and compatible with any device. More precisely, this solution is based on a Virtual User installed in the Personal Computer provided with the Shearography acquisition software and connected to the controller. The Virtual User itself, is developed in Labview environment, and programmed for performing a series of operations, organized according to a specific sequence, aiming at achieving the goals listed above. The sequence of actions to carry out is the following one, and is also outlined in Fig. 4.16.

1. Heating the structure for a given time interval. Before loading, relay 1 is set by default to *normally open*, meaning that the lamps circuit is open and the lamps are not powered. On the contrary, relay 2 is by default set to *normally close*, meaning that the electromagnets are powered to constraint the shutters. Hence, Virtual User activates relay 1 to switch-on the lamps for the time interval pre-defined by the user. Relay 2 is still activated.

2. Switching-off the lamps and, at the same time, making the shutters fall to screen-off the lamps themselves. In this phase, both relay 1 and relay 2 are deactivated, so that both lamps and electromagnets are no longer powered.

3. Starting Shearography acquisition after a pre-defined time interval successive to load interruption. The Virtual User now acts on the Shearography acquisition software and is able to store phase-maps with the chosen rate.

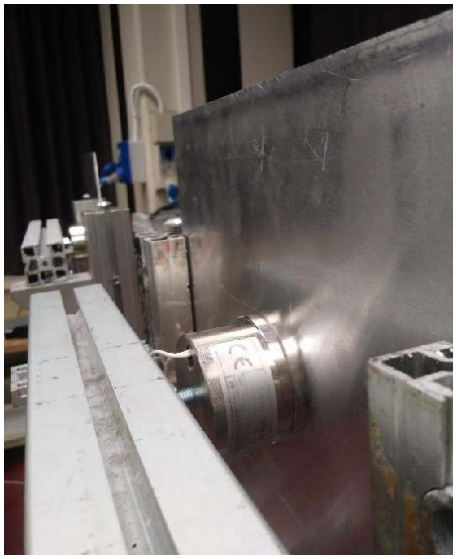

(a) *Electromagnet used to keep the shutter in position when the lamps are heating the structure and to release it after loading*

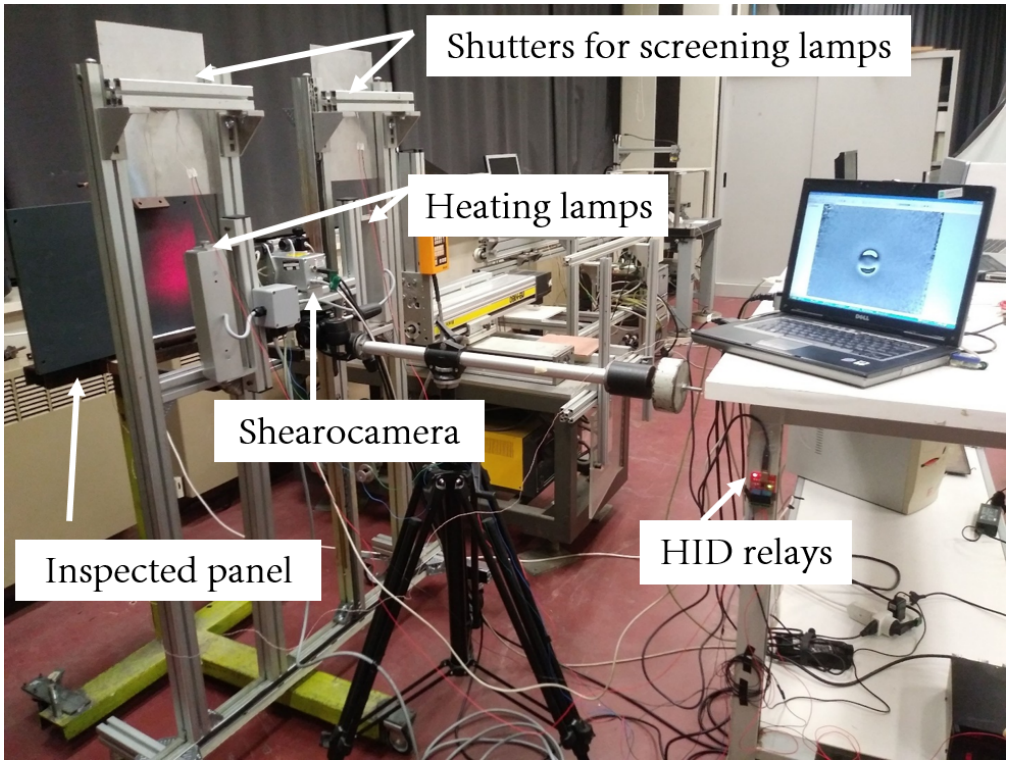

(b) *Entire measurement setup*

Figure 4.14: Measurement setup

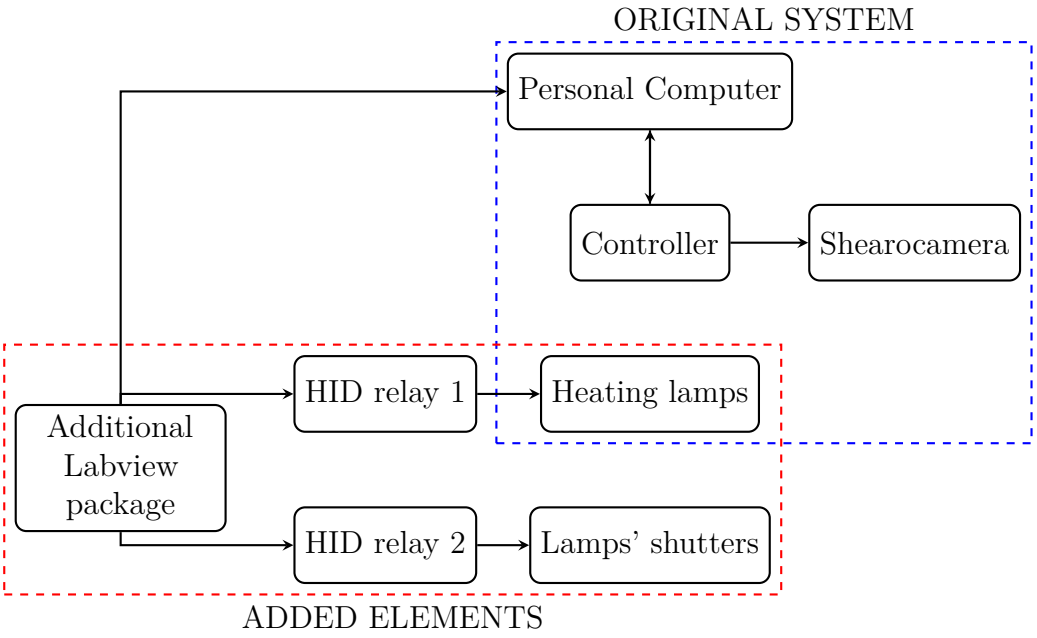

Figure 4.15: Measurement setup scheme

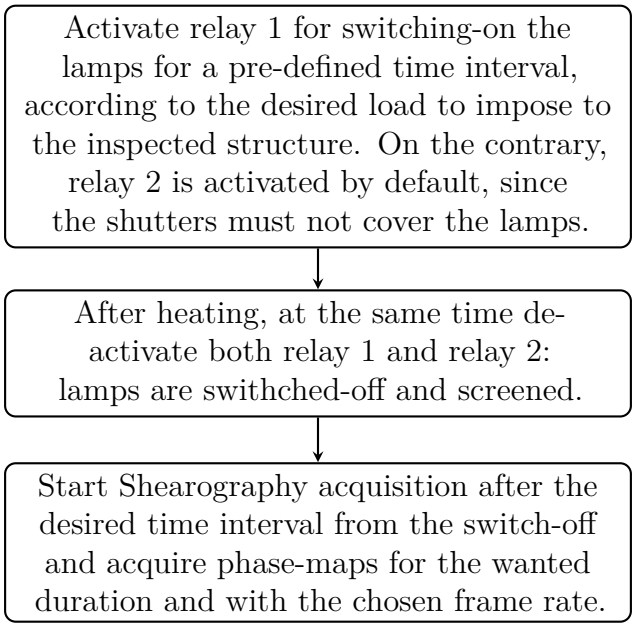

Figure 4.16: Sequence of operations performed by the Virtual User

These operations are performed by sequentially pushing the corresponding *open* and *close* buttons within the Relay software interface (see Fig. 4.17a, and the *start acquisition*, *store image* and *end acquisition* buttons within the Shearography acquisition software (see Fig. 4.17b). The Virtual User is able to recognize and to find such buttons thanks to a pattern matching algorithm, requiring, at the very first use of the Virtual User itself, to load the template buttons to use for matching. This is a one-time and very fast operation that does not affect time efficiency at all.

4.3 Definition of a measurement procedure for data acquisition and analysis

The hardware and software developed in Sec. 4.1 and 4.2 were integrated within a specific procedure aiming at providing the user with quantitative indications and unambiguous results. This procedure can be carried out even if the material properties are unknown, and can be divided into two different phases:

1. preliminary operations;
2. defect characterization and reconstruction.

4.3.1 Preliminary operations

As will be better discussed later, the developed approach is based on the application of different, intensity-increasing load steps. Therefore, the first aspect to tackle is to state the maximum load step intensity to impose to the structure, while the minimum one is given by the system's rapidity. The maximum condition can be defined by physical considerations lying in the fact that a defect can be well represented by Shearography technique only if its deformation is sufficiently different from the deformation of the rest of the structure. This no longer happens once the load reaches such an intensity that its effect on the entire structure dominates on the differences between the defect and the structure itself. In this case, in fact, in conjunction with fringes related to possible defects within the inspected components, generalized fringes representing the deformation of the entire component appear, see for example Fig. 4.18. This causes both a decrease of the

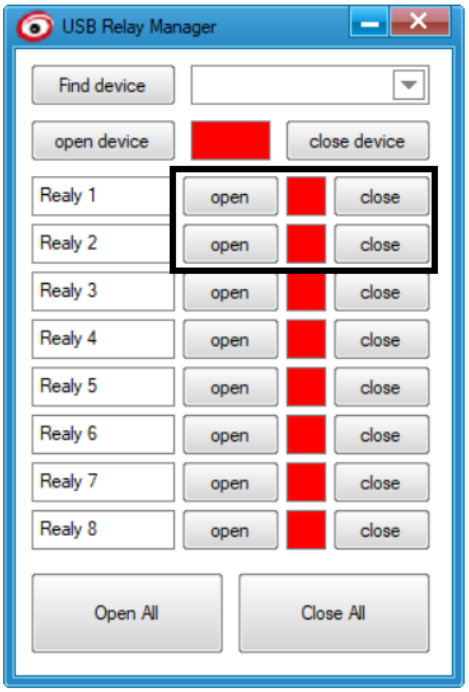

(a) *Template buttons for controlling realy1 and 2, indicated by the black rectangle*

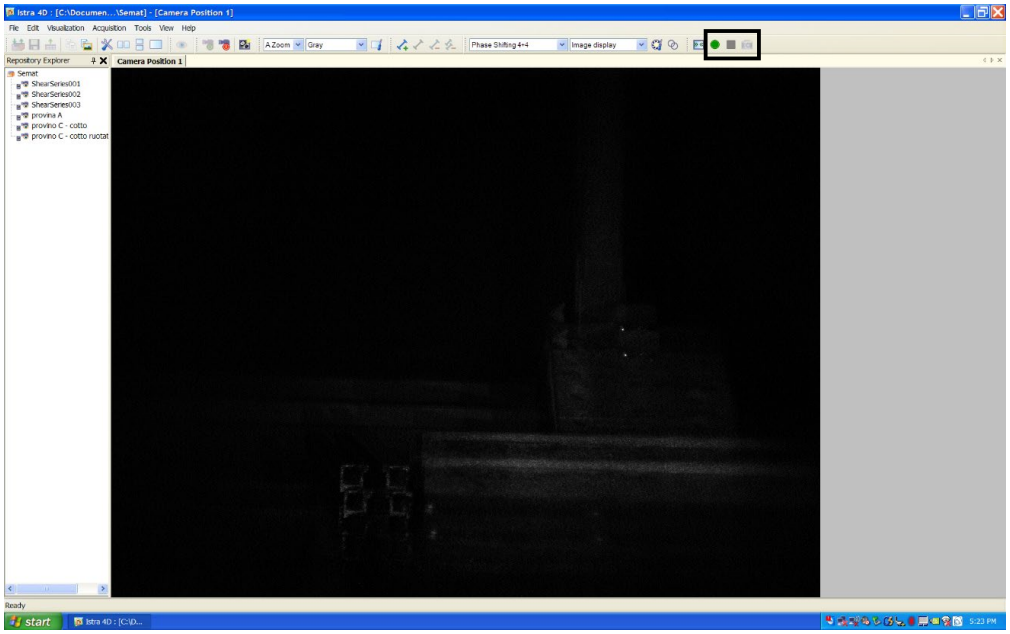

(b) *Template buttons of Shearography acquisition software, indicated by the black rectangle. From left to right: start acquisition, end acquisition, store current phase-map*

Figure 4.17: Template buttons for Pattern Matching

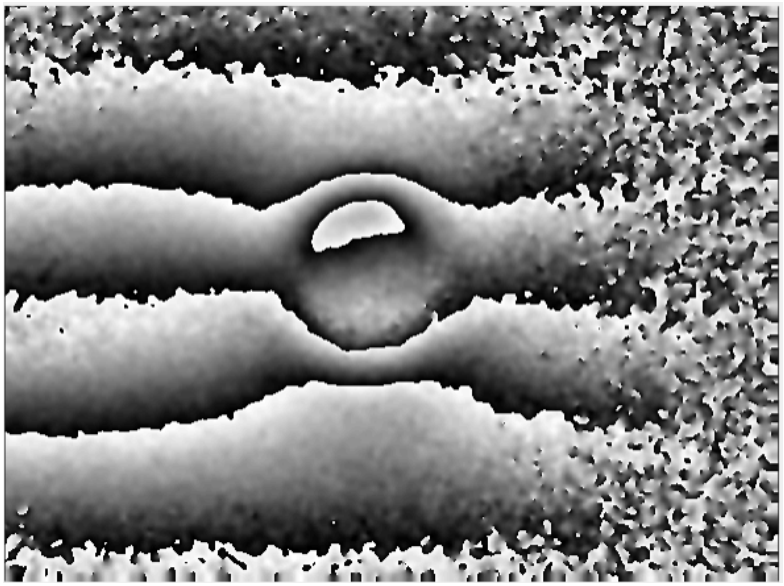

Figure 4.18: Example of superimposition of defect fringes and fringes generated by the deformation of the entire structure

Signal-to-Noise Ratio and the fact that defect boundaries are incorporated within the global deformation of the structure, increasing the probability of errors in the reconstruction performed by the algorithm described in Sec. 4.1. The described condition occurs when the thermal radiation reaches the defect depth; this moment can be expressed as the delay between the heated surface and a given position L inside the material thickness. If material properties are known, this delay can be expressed as the material phase shift f in accordance with the standard ASTM-E 2582-07 [57] :

$$f = \frac{L^2}{\pi\alpha}[s], \tag{4.4}$$

where α is the thermal diffusivity in m^2s^{-1} defined by:

$$\alpha = \frac{k}{\rho c_p}\left[\frac{m^2}{s}\right], \tag{4.5}$$

with k representing the thermal conductivity in $Wm^{-1}K^{-1}$, ρ is the material density in kgm^{-3}, and c_p is the specific heat at constant pressure in $Jkg^{-1}K^{-1}$. Unfortunately, usually thermal properties of the material are not known. Therefore, the idea is to calculate this delay as the material time constant τ, by putting a

Table 4.1: Thermal properties of the PVC test panel

$k \left[\frac{W}{mK}\right]$	$\rho \left[\frac{g}{cm^3}\right]$	$c_p \left[\frac{J}{KgK}\right]$
0.14	1.42	880

thermocouple on the component surface, and another one on the opposite side. In fact, at the very beginning, the study has to be performed by considering all the material thickness since the defect presence has not been checked yet and, in any case, the defect depth is not known. After positioning the thermocouples, the operator imposes a step excitation and computes the corresponding response of the back side of the component, as a first-order system. The time constant of the back side is evaluated as the 63% of the asymptotic value. At this point, it is possible to suppose the maximum depth up to which it is expected to find defects, considering that Shearography may fail in detecting defects deeper than 5 mm. Thus, by substituting τ with f, it is possible to compute the thermal diffusivity α by Eq. 4.4 and, by the same Equation, it is also possible to substitute L with the imposed maximum depth for recomputing the delay in that position. This value will be used as the maximum heating time to impose to the inspected component. As anticipated at the beginning of this Chapter, a PVC specimen with known and accessible defects (see Fig. 4.19) were exploited for developing the measurement procedure. In this phase, the defects accessibility was exploited to validate the just proposed method. The mechanical and thermal properties of the PVC test panel (reported in Tab. 4.1) were known and used to calculate the phase shift for the entire thickness (10 mm), resulting $f = 291\ s$. Furthermore, the step response of the back side of the panel was computed, giving $\tau = 291\ s$. Fig. 4.20 graphically shows this operation. In this way, by using Eq. 4.4 it was possible to calculate $\pi\alpha = 0.34\ m^2/s$. This latter value was used, supposing a maximum defect depth of 3 mm, for computing the delay at this position, giving $f = 27\ s$. At this point, having access to the defects, as can be verified from Fig. 4.19, another thermocouple was put in correspondence of the defect of 3 mm depth, and the same experiment as the one on the back-side was carried out. Accordingly to the theoretically-calculated value, the delay calculated at 3 mm depth by the step response, was $27s$, see Fig. 4.21. At the end, this double check confirms the validity

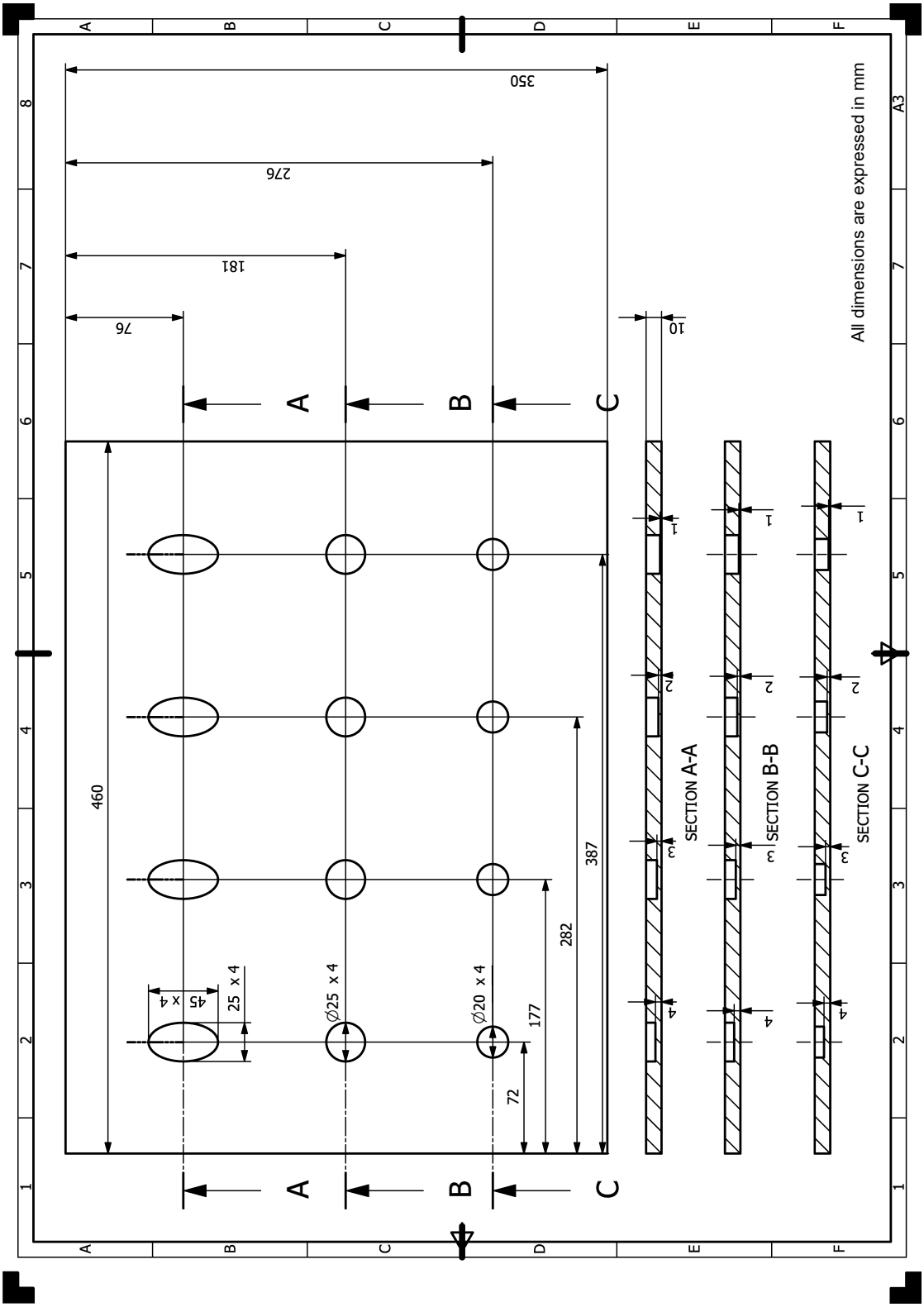

Figure 4.19: Technical 2D draft of the PVC test panel used for developing the procedure

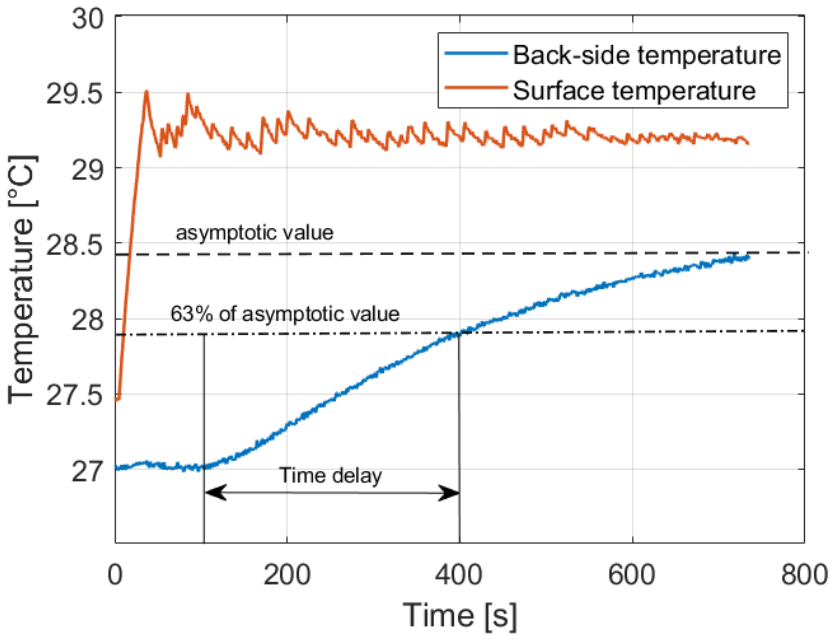

Figure 4.20: Step response of the back-side of the PVC test panel

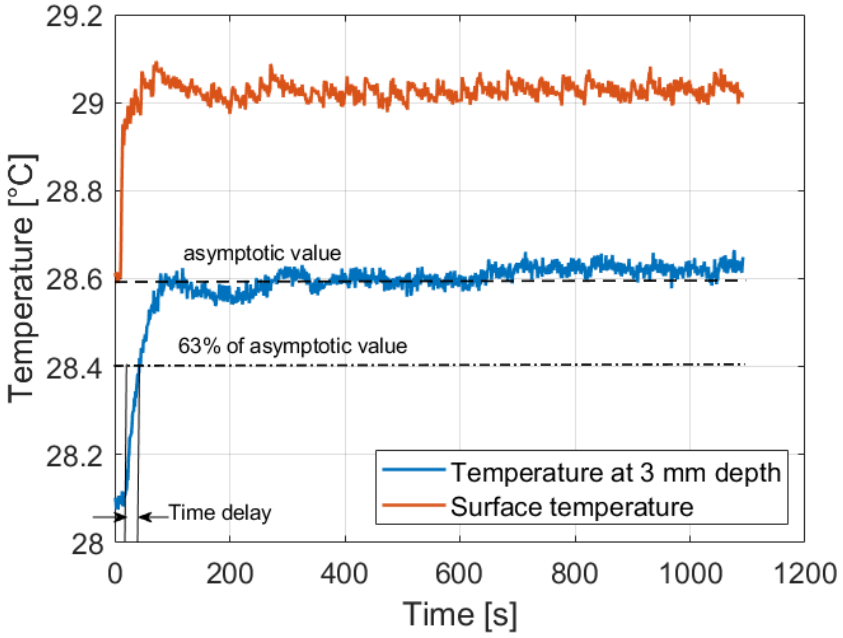

Figure 4.21: Step response of the PVC test panel at 3mm-depth

of the proposed method for the determination of the maximum heating time to apply for given depth. This first step is performed a priori, before activating the Shearography hardware.

After that, the second step involves the definition of the measurement ranges for a given load cycle. For this purpose, it is worth to recap the relationship that links the variation of the phase relation Δ occurring after the load imposition, the shearing amount δx, and the first derivative of the out-of-plane displacement $\partial w/\partial x$, in cases where the shear is set along a unique direction (even if not perfectly unique), and the laser beams are aligned with the focal direction of the Shearocamera:

$$\frac{\partial w}{\partial x} = \frac{\lambda}{4\pi\delta x}\Delta. \tag{4.6}$$

It is necessary, then, to define a sequence of actions to perform in order to compute $\partial w/\partial x$ and to define the measurement ranges, as consequence. For this purpose, the procedure is articulated as in the following, exploiting the software items discussed in Sec. 4.1.1, 4.1.2, 4.1.3, 4.1.4, i.e.:

1. heating the structure, where the heating time lies in the range defined previously;
2. taking the reference image 1 s after lamps switch-off, in order to reduce noise, as described in Sec. 3.1;
3. acquiring an image per second for 60 s;
4. data encoding and wrapped phase computation from speckle images;
5. distorsion correction;
6. shear computation;
7. phase-map filtering;
8. absolute phase computation: this step may be obtained either by unwrapping the fringe maps and successively computing the unwrapping error by comparison with the maps obtained by *Adding and Subtracting method*, or by simply using the *Adding and Subtracting method* results. Once computed the

absolute phase and the shearing amount, the absolute displacement gradient can be obtained by Eq. 4.6.

At this point, an important aspect lies in the fact that the resolution associated to the detected deformation is strictly related to the shearing amount. Therefore, this parameter influences both the number of fringes associated to a given deformation (hence the system sensitivity) and the minimum, detectable, deformation change. The latter is generally expressed per-unit of shear, in fact. In particular, our system resolution is given by:

$$0.03\frac{\mu m}{\delta x}. \tag{4.7}$$

This is a focal point for the definition of the measurement ranges. In this regard, it is fundamental to define two other limit conditions, i.e. the one associated to the first fringe appearing and the one associated to the maximum accepted number of fringes that, according to [58], can be set to 10. This upper limit is due to resolution as well: after the 10th fringe, in fact, the spatial gap between adjacent fringes becomes too short to be resolvable even for smaller $mm/pixel$ ratios. Both the discussed conditions can be expressed by mathematical formulations. In particular, the first fringe appears when:

$$\Delta_{max} - \Delta_{min} = 2\pi \tag{4.8}$$

thus, by substituting Δ with $\partial w/\partial x$ by using Eq. 4.6, it is obtained:

$$\left(\frac{\partial w}{\partial x}\right)_{max} - \left(\frac{\partial w}{\partial x}\right)_{min} = \frac{\lambda}{2\delta x}. \tag{4.9}$$

In the same way, when the observed phase-map reaches the 10th fringe, it occurs:

$$\Delta_{max} - \Delta_{min} = 2\pi \cdot 10, \tag{4.10}$$

that, in terms of deformation, becomes:

$$\left(\frac{\partial w}{\partial x}\right)_{max} - \left(\frac{\partial w}{\partial x}\right)_{min} = \frac{5\lambda}{\delta x}. \tag{4.11}$$

By considering Equations from 4.8 to 4.11, it can be noticed that the shear amount has a dominant role even in the definition of the measurement ranges. Fig. 4.22

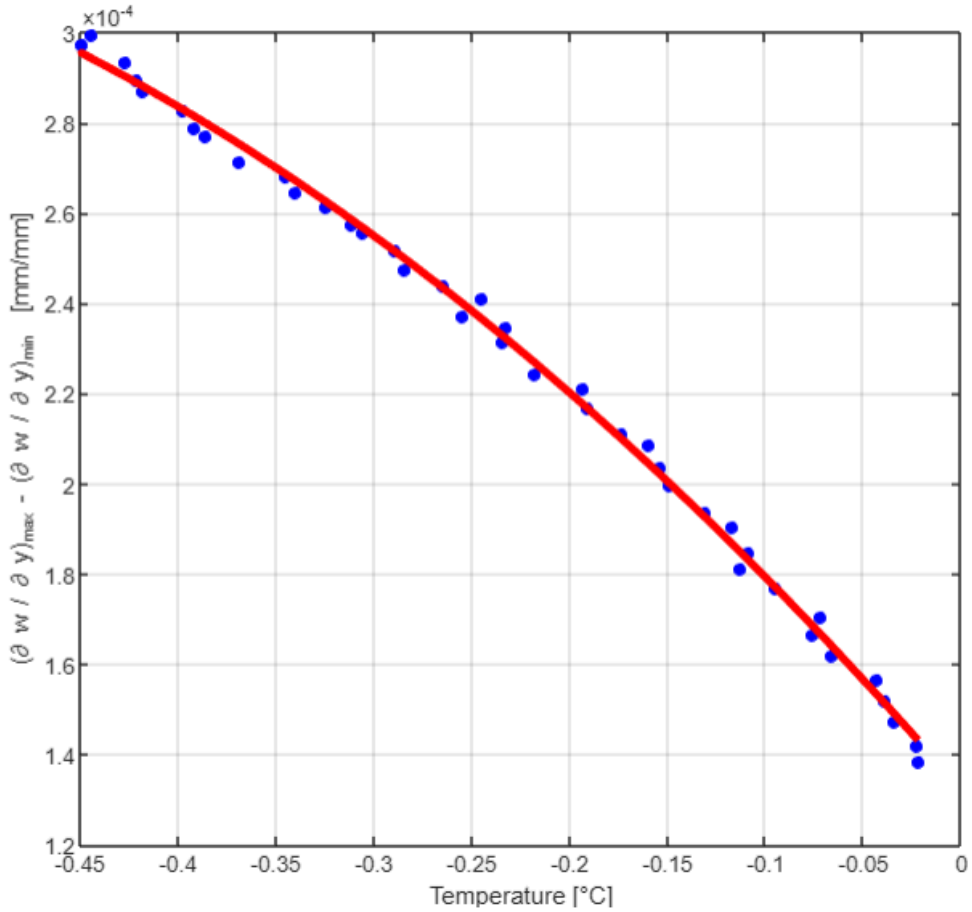

Figure 4.22: Relationship between Shearography-detected deformation and temperature variation

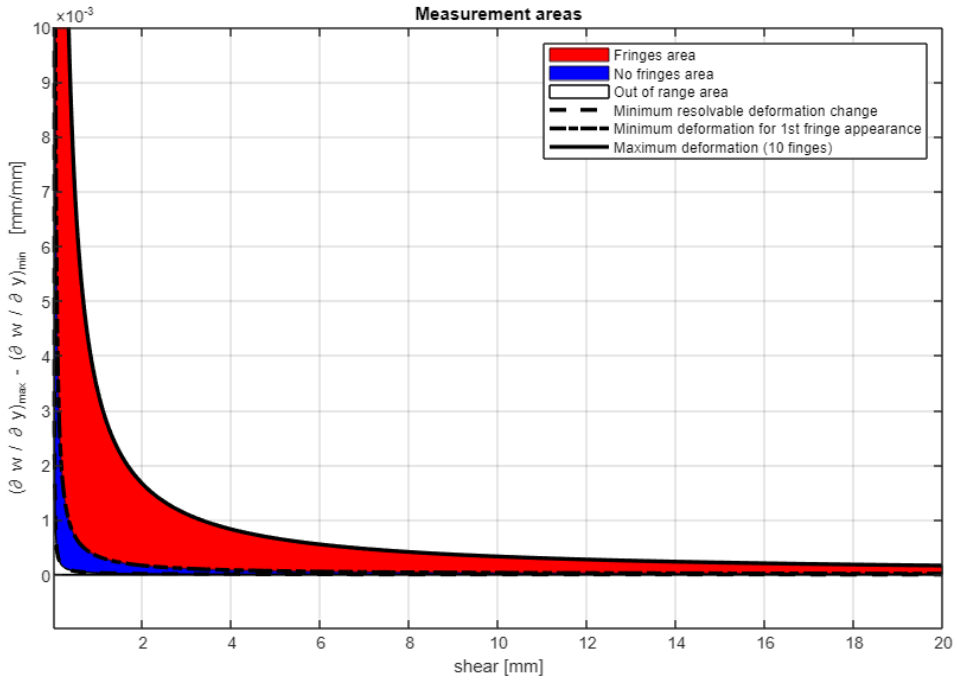

Figure 4.23: Measurement areas for a given load cycle

shows an example of the detected relationship between displacement gradient and temperature variation. This was obtained by using a thermal camera to match the mechanical behavior detected by Shearography, with the temperature evolution of the structure. The temperature variation is computed with respect to the same time instant as the one corresponding to the Shearography reference image. This can be exploited for converting measurement areas of Fig. 4.23 in terms of temperature changes, as shown in Fig. 4.24. Of course, if the load applied to the structure changes, the relationship between deformation and temperature changes too. Therefore, Fig. 4.24 should be recomputed each time the load is varied.
Fig. 4.23 graphically represents Equations 4.7, 4.9 and 4.11 for different values of shear. This is useful since, in a real application, one could have a specific requirement about the minimum displacement gradient to resolve, that is dependent on the shear itself for Eq. 4.7. Therefore, by this Equation it is possible to compute the shear needed to resolve such a deformation. However, it is highly probable that the phase change generated by this shear value, that is the minimum acceptable one, is not sufficient to provide a good Signal-to-Noise Ratio. In fact, this shear

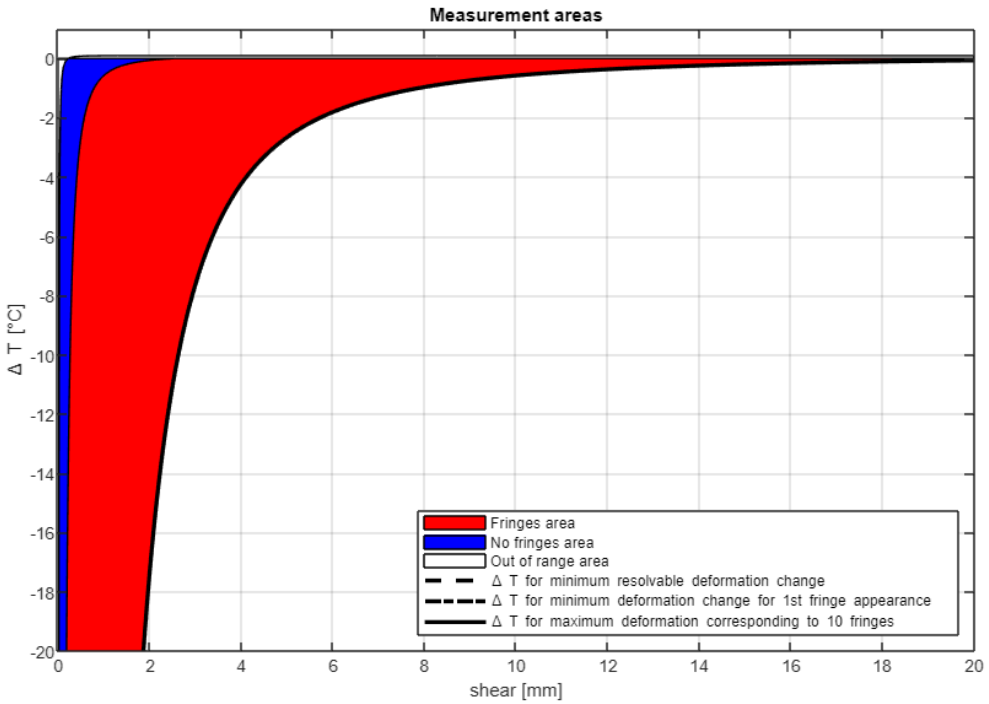

Figure 4.24: Measurement areas for a given load cycle

does not generate a phase variation higher than 2π, thus no fringe is detected. Therefore, through the Equations 4.9 and 4.11, it is possible to evaluate, for the given shear, the deformation range within which fringes can be detected, in order to have higher SNRs. Of course, even the variation of shear values must be limited within a given range that, this time, is established by the positioning system acting on the shearing mirrors. Therefore, the operator has to manually set the minimum and the maximum shear and to acquire the corresponding images. The *.hdf5* file, encoded in Matlab environment as described in Sec. 4.1.1, contains also the information about the shear vector in the image plane, that can be easily converted in the one on the object plane by the calculation of the Magnification M, see Eq. 2.7. Alternatively, if it is the deformation to apply to be fixed, instead of the shear amount, it is possible to evaluate by the same Equations, the shear range characterized by fringes detection. These aspects are shown in Fig. 4.23: the blue area corresponds to the measurement range where Shearography is able to resolve deformation changes as the shear varies, without facing phase relations higher than 2π (no fringes). On the contrary, the red area describes the fringe detection-range

of values, and the shear axis is limited by the pre-determined range.

4.3.2 Defect characterization and reconstruction

After having defined the measurement ranges for shear values, heating time and displacement gradient, the second phase of the studied procedure deals with cases where, after load application, one or more defects is (are) detected. Here, it is useful to repeat some information already provided in Chapter 1, regarding the elements influencing the defect size estimation, since they were used for developing this procedure phase itself. These elements are:

1. shear amount: as already discussed in multiple Sections, it changes the instrument sensitivity and the resolution in the deformation estimation;

2. distance of observation: it changes the spatial resolution and has an effect on turbulence produced by the heating radiation. In general, the nearer the Shearocamera, the more precise is defect reconstruction, compatibly with the possibility of reaching a good focalisation;

3. applied load: the higher the load, the more warped the defect, the higher its overestimation. On the contrary, the smaller the load, the lower the Signal to Noise Ratio, the less reliable the results. For this purpose, the idea developed in this work is to apply to the inspected structure different load cycles, increasing heating time from a cycle to another. Shearography results, then, have to be examined and a criterion for choosing the load cycle providing the right defect estimation is needed;

4. defect depth: the inner the defect, the lower the difference between the defect deformation and the background deformation, the lower the Signal to Noise Ratio;

5. defect size: the smaller the defect, the lower the difference between the defect deformation and the background deformation, the lower the Signal to Noise Ratio.

Therefore, being the defect characterization so sensitive to the mentioned parameters, and being the geometrical features of the defect itself a conditioning item, when

Table 4.2: Parameters used for method developing and testing

Shearing amount [mm]	**Distance of observation [cm]**	**Heating time [s]**	**Defect size [mm]**	**Defect depth [mm]**
3, 5, 10	24, 50, 70	1, 2, 3, 5, 10, 15	1, 2, 3, 4	10, 15, 25

a Shearography operator meets fringes related to the presence of a defect, a weel-defined series of actions to carry out is needed for being confident with inspection results. For this purpose, the developed procedure consists in performing sequential tests on the same defect, varying conditioning parameters, mainly shear and load. The distance of observation can be varied too, in order to have an idea of the loss of accuracy faced when the Shearocamera is moved further from the inspected surface. Tab. 4.2 shows the parameters values chosen for developing and testing the method. For a better explanation of the procedure, consider the PVC test panel of Fig. 4.19 putting the focus, in the very beginning, on the defect with a diameter of 25 mm positioned at a depth of 1 mm from the surface. In the first inspection, the defect was observed from a distance of 24 cm. At first, a shear value was fixed (5 mm, for example) and the different heating time expressed in Tab. 4.2, according to the measurement procedure already reported in Sec. 4.3.1, were applied. Therefore, a video showing the cooling phase of the defect and the surrounding background was stored for each load cycle, and the algorithm proposed in Sec. 4.1 was applied to each frame of each video, such that the time evolution of the defect size and shape could be obtained. The information matched with defect size for each frame, is the quantity $\left(\frac{\partial w}{\partial x}_{max} - \frac{\partial w}{\partial x}_{min}\right)_{defect} - \left(\frac{\partial w}{\partial x}_{max} - \frac{\partial w}{\partial x}_{min}\right)_{background}$, since it gives an indication about how much the defect is visible with respect to the background. An example of a typical time history of $\left(\frac{\partial w}{\partial x}_{max} - \frac{\partial w}{\partial x}_{min}\right)_{defect} - \left(\frac{\partial w}{\partial x}_{max} - \frac{\partial w}{\partial x}_{min}\right)_{background}$ is shown in Fig. 4.26a, while the difference of the temperature gradient between the defect and the background $(dT/dt)_{defect} - (dT/dt)_{background}$ is reported in Fig. 4.26b. From these two Figures, it is possible to note that the two trends are perfectly comparable: this highlights the fact that, for thermal load applications, the difference of thermal sensitivities between defect and background is linked to the difference of displacement gradients, detected by Shearography. Moreover, Fig. 4.26 represents

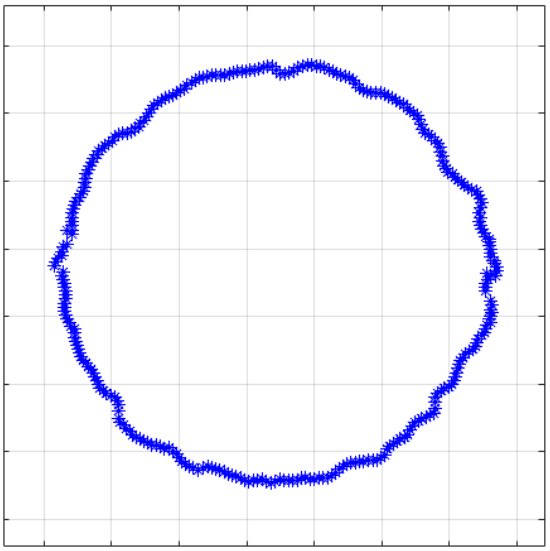

Figure 4.25: Morphology reconstruction of the 25 mm-diameter defect localized at 1 mm depth and observed from a distance of 24 cm.

the physical behavior of the defect: initially, the deformation gap between the defect itself and the rest of the structure increases and, successively, reaches a maximum value, around which this gap stabilizes for a certain time interval, depending on the imposed load. The smaller the load, the longer the time interval; the higher the load, the more dynamical the phenomenon, the shorter the time interval. After this time interval, the global deformation becomes more important and starts approaching the defect deformation, thus the gap decreases. Furthermore, an important aspect lies in the fact that, when the gap stabilizes around the maximum value, the detected defect size stabilizes too, as can be seen in Fig. 4.27. Thus, by matching Fig. 4.26a and Fig. 4.27, it is possible to obtain the graph of Fig. 4.28. Here, it is easy to note that the stabilization time intervals generate accumulation points in the bivariate distribution composed of displacement gradient differences and defect size. In addition, these accumulation points corresponds to increasing defect sizes as the heating time increases in turn, thus moving away from the actual size. However, there exist two particular cases in which this does not happen because the relationship between the displacement gradient and the defect size is completely random (see for example Fig. 4.29) :

1. the load is not sufficient to guarantee such relationship, meaning that the

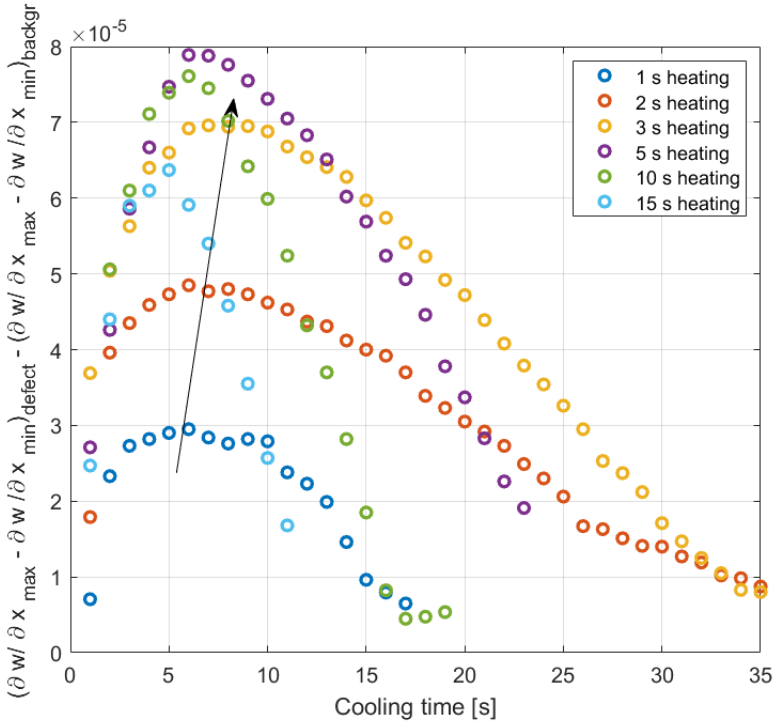

(a) *Difference of displacement gradients detected by Shearography*

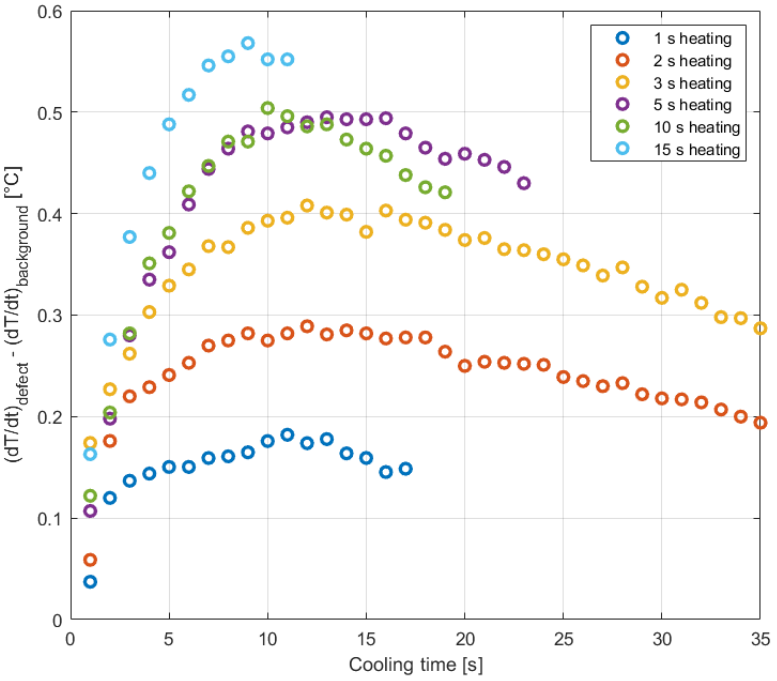

(b) *Difference of temperature gradients detected by Thermal Camera*

Figure 4.26: Differences between defect and background in terms of mechanical and thermal behavior

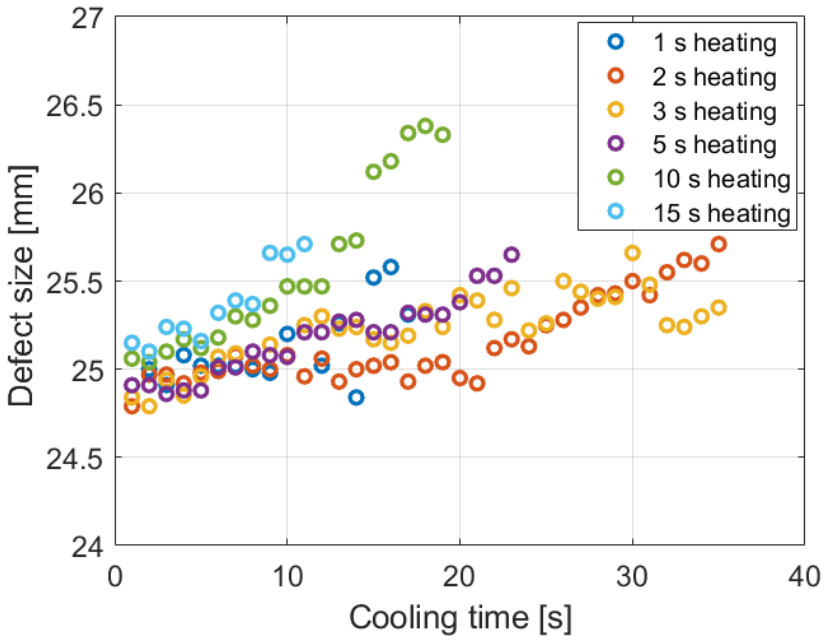

Figure 4.27: Time histories of the detected defect size for different load cycles.

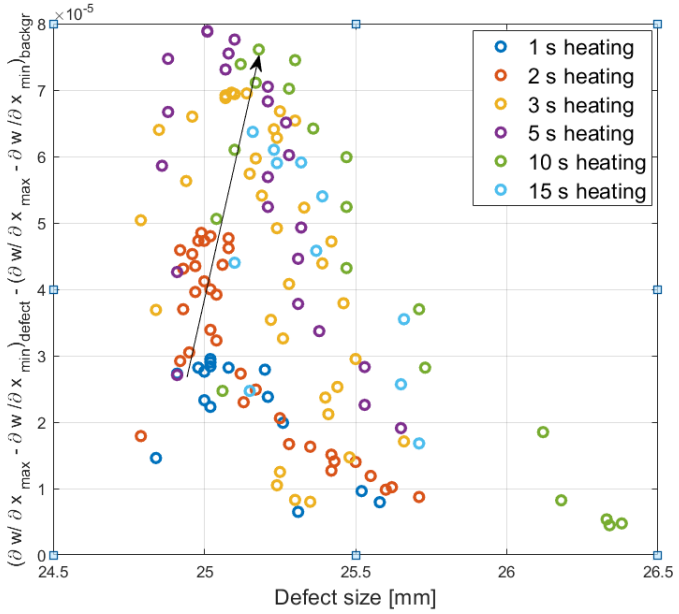

Figure 4.28: Correspondence between the mechanical behavior of the defect and its size computed by the developed procedure.

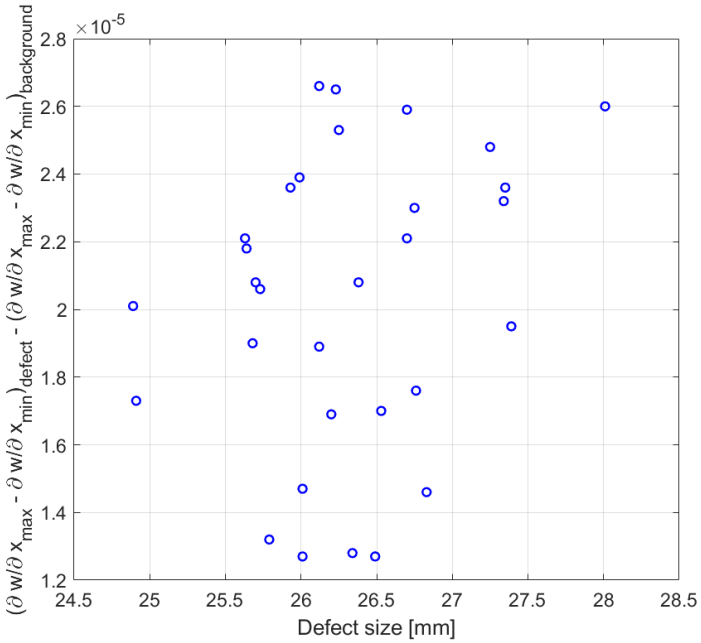

Figure 4.29: Example of random relationship between displacement-gradient difference and defect size

defect is not well represented;

2. the load is too large, so that the transit through the stability region is too fast and no accumulation point can be detected.

These two cases must be discarded since they do not provide reliable results. As a consequence of the previous statements, it makes sense to choose the minimum heating time providing an accumulation region, as the right data collection corresponding to the actual defect size.

At this point, a robust criterion is needed for examining the different load-cycle results and for selecting the data collection corresponding to the smallest load able to generate an accumulation point. For this purpose, statistical tests were exploited. In particular, the χ^2 test of independence showed that all the results (even the random ones) are positive to the χ^2 test, meaning that deformation differences (between defect and structure) and defect-size are always dependent. Furthermore, the χ^2-test positive results were subjected to the bivariate-normality test, since the positive ones correspond to random cases, where no accumulation point can

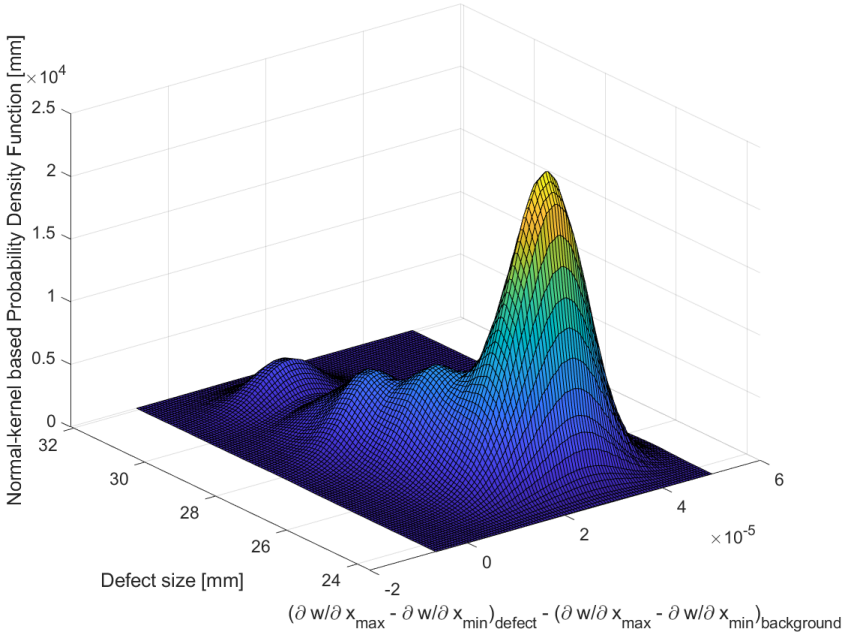

(a) *Accumulation point case*

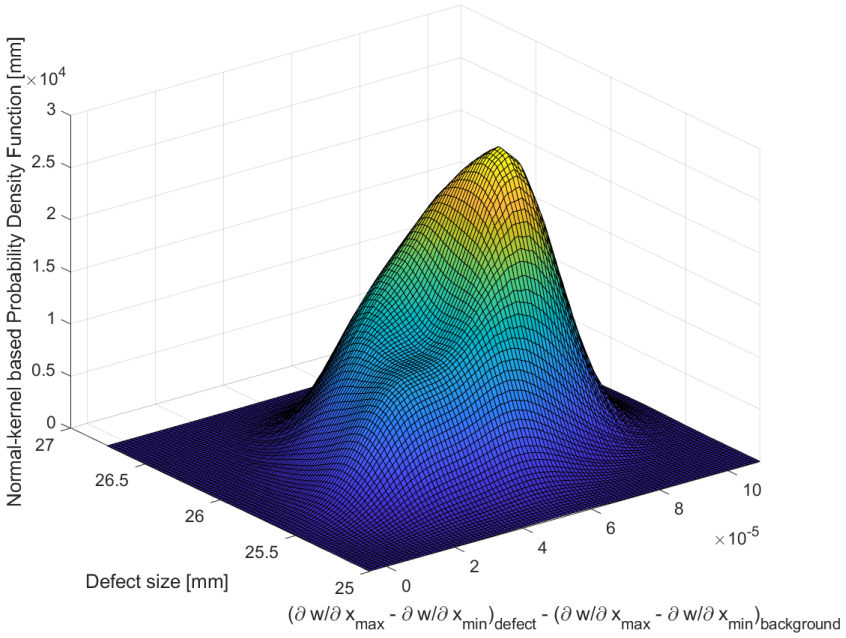

(b) *Random-relationship case*

Figure 4.30: Kernel-based Probability Density Functions for accumulation points and random cases.

be detected. Therefore, they must be discarded. In particular, three different bi-variate normality tests were performed: Royston's Multivariate Normality Test [59], Doornik-Hansen Omnibus Multivariate Normality Test [60], Henze-Zirkler's Multivariate Normality Test [61]. If at least one of these checks the presence of a normal distribution, the corresponding data-set is discarded. After these discarding tests, the remaining data-collection corresponding to the smallest applied load, is used as confident measurement, and the results exploited for carrying on the procedure. More precisely, the diameter value extracted from the data-set is the one corresponding to the maximum (accumulation point) of the bi-variate Probability Density Function. Fig. 4.30a shows an example of the Kernel-based Probability Density Function corresponding to the presence of an accumulation point, while Fig. 4.30b shows the same function obtained for a random relationship between displacement gradient and defect size. The Kernel distribution was exploited since it is able to define a Probability Density Function even when a parametric distribution cannot properly describe the data, or when you want to avoid making assumptions about the distribution of data, which is our case. A Kernel distribution is defined by a smoothing function and a bandwidth value, which control the smoothness of the resulting density curve. For any real values of x, the Kernel density estimator's formula is given by:

$$\hat{f}_h(x) = \frac{1}{nh} \sum_{i=1}^{n} K\left(\frac{x - x_i}{h}\right), \tag{4.12}$$

where $x_1, x_2, ..., x_n$ are random samples of an unknown distribution. n is the sample size, K is the Kernel smoothing function, and h is the bandwidth.

For a given distance between inspected object and Shearocamera, the procedure described above has to be repeated for at least three different shear values. Among these three values, there should be at least one having a difference of an order-of-magnitude with respect to the others. This enables to achieve an overview about the effect of the variation of the shear amount and makes more robust the computation of the optimal conditions. As already anticipated, in this work the shear values reported in Tab. 4.2 were used. Results obtained for the 25 mm-diameter defect positioned at a depth of 1 mm inside the material and observed from a distance of 24 cm, are reported in Tab. 4.3. Results of Tab 4.3, then, are graphically shown in Fig. 4.31. Here, it is possible to see that the simplest curve that fits the data is a parabola, whose vertex corresponds to the optimal condition (marked with the black

Table 4.3: Statistical results for the 25mm-diameter defect, positioned at 1 mm depth from the surface and observed from a distance of 24 cm (0.08 $\frac{mm}{pixel}$).

Computed shearing amount [mm]	**Statistically-chosen defect size [mm]**	**Statistically-chosen heating time [s]**
3.06	25.70	3
5.12	25.02	1
10.10	27.70	1

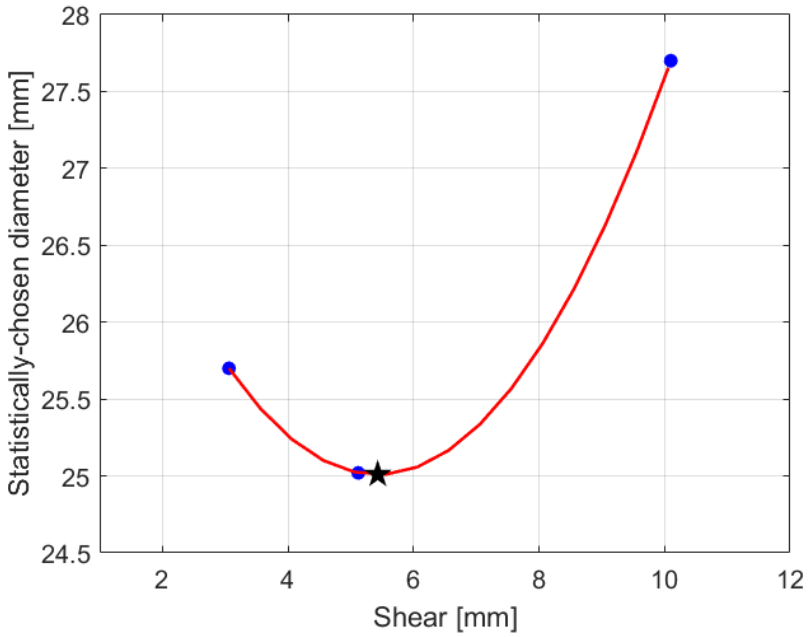

Figure 4.31: Graphical trend of results for the 25mm-diameter defect, positioned at 1 mm depth from the surface and observed from a distance of 24 cm.

Table 4.4: Optimal condition for the 25mm-diameter defect, positioned at 1 mm depth from the surface and observed from a distance of 24 cm.

Optimal shear[mm]	**Defect expected dimension if the optimal shear were used [mm]**
5.43	25.01

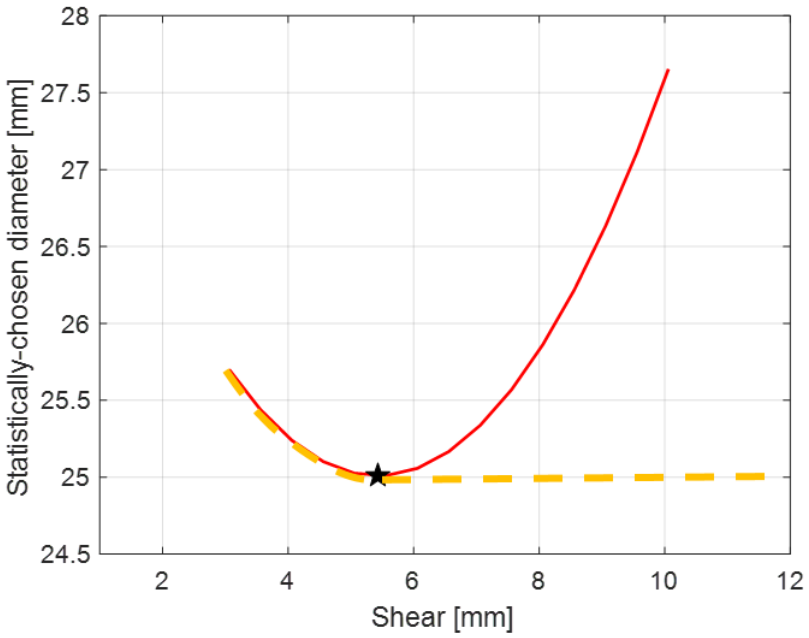

Figure 4.32: Theoretical explanation of the suitability of the parabolic fit.

star in Fig. 4.31) and, consequently, to the best size estimation. This condition is reported in Tab. 4.4. The parabolic relationship between shear and detected defect size has a physical explanation too, that strengthens the choice of such a fit. In this regard, it is worth to refer to Fig. 4.32. The part of the curve between the lower shear values and the optimal value (marked, again, by the black star) is due to the fact that, as the shear increases, the deformation resolution and the instrument sensitivity increase too, providing a better defect reconstruction. On the other hand, after reaching the optimal value, the effect of the sensitivity-increase is more evident with respect to the effect of the increase-of-resolution. This causes an increase of incoming noise within the measurement. For this reason, the defect reconstruction starts to get worse again, moving away from the theoretical trend, expressed by the orange, dashed line in Fig. 4.32. The theoretical behavior, in fact, stabilizes at the optimal condition, since an increase of sensitivity in ideal conditions (no incoming noise) only increases the contrast with respect to the background, with no effect on the defect boundaries since the background is not alterated. As a further confirmation of these theoretical statements, it is worth to consider three different phase-maps (see Fig. 4.33a) corresponding to the three used

shear values (3, 5 and 10 mm), and having comparable phase relation changes Δ in the background, as it is possible to see in Fig. 4.33b, where an interrogation line is extracted from each phase-map. The Peak magnitude-to-Root Mean Square ratio of the background is calculated from the three phase maps, obtaining the graph of Fig. 4.34. Here it is possible to observe the very same trend of the detected defect size, reported in Fig. 4.31. This confirms that, the combination of sensitivity and resolution has a parabolic influence on results as the shear varies, and that the actual defect size coincides with the vertex of the parabola. Furthermore, by varying the observation distance (thus, the spatial resolution, expressed by the $\frac{mm}{pixel}$ ratio), to parity of defect diameter (25 mm) and depth (1 mm), Fig. 4.35a and 4.35b are obtained. Fig. 4.35a shows that the loss of spatial resolution, i.e. the increase of observation distance, must be compensated by an increase of sensitivity and deformation resolution (shear) for achieving a good defect estimation. Moreover, Fig. 4.35b highlights that, after a critical value, the spatial resolution loss causes a great worsening of measurement precision.

By repeating the same procedure for different depths, the results in Fig. 4.36a and Fig. 4.36b were obtained, thus enabling to make further theoretical considerations. More precisely, Fig. 4.36a shows that the shear needed for reaching the most precise, achievable defect estimation, increases with the defect depth. This is in accordance with the fact that deeper defects deal with smaller deformation differences between the defect itself and the background, thus needing a higher sensitivity and resolution (shear) for estimating the deformation, in order to obtain a good reconstruction. On the other hand, Fig. 4.36b highlights that the deeper the defect, the less precise its estimation even in optimal conditions for the corresponding case. The described effects, both for shear and accuracy are much more evident for depths larger than 3 mm for the inspected defect. By matching Fig. 4.35a and Fig. 4.36a, Fig. 4.37 is obtained. Here it is possible to note that the optimal shear trend with respect to the observation distance is the same for different defect depths and vice versa.

At the very end, the described procedure was applied to other defects, whose dimensions are reported in Tab. 4.2. All the elaborations gave back a parabolic trend of results, confirming the assumptions made above. By merging all combinations of results, the 3D graph shown in Fig. 4.38 is obtained. In this plot, three different behaviors corresponding to the three different defect sizes can be detected, with

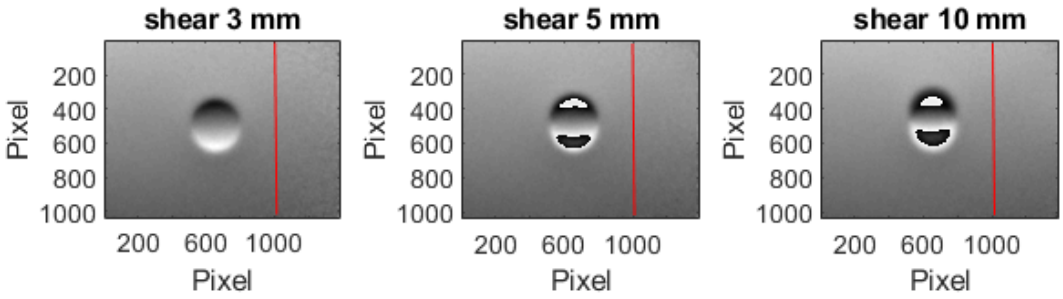

(a) *Phase-maps used for explaining the parabolic behaviour.*

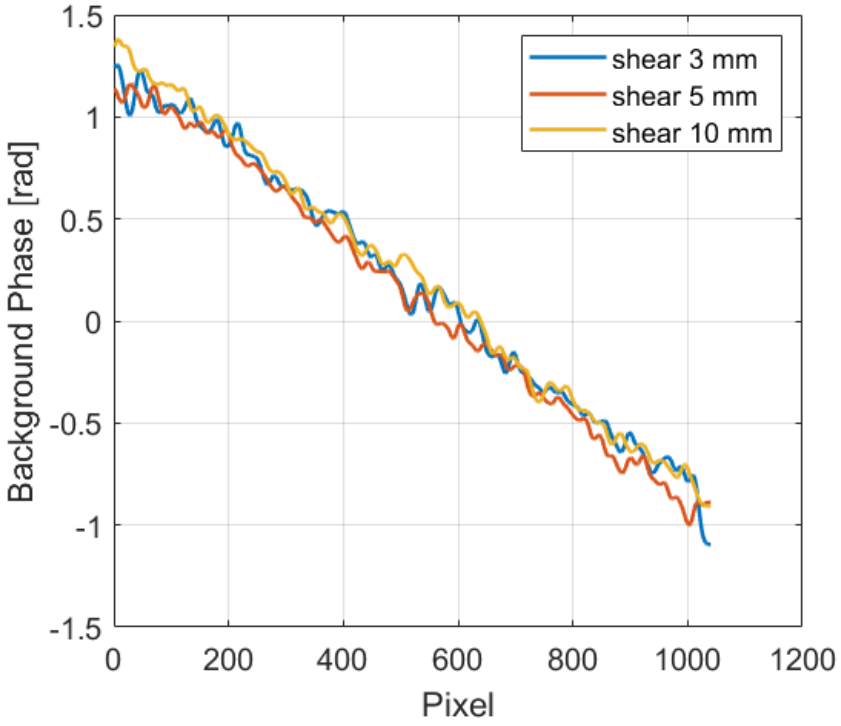

(b) *Interrogation line extracted from the three backgrounds.*

Figure 4.33: Data used for the validation of the parabolic-fit choice.

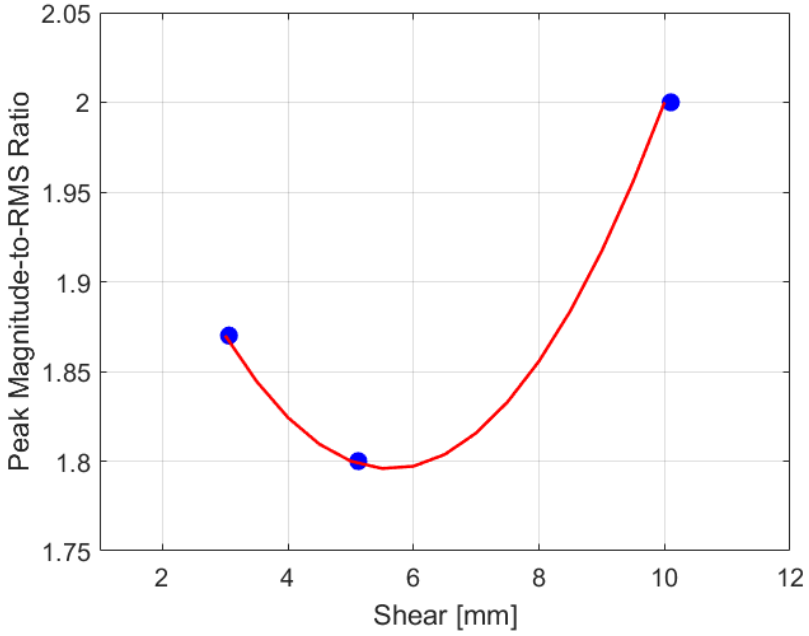

Figure 4.34: Peak Magnitude-to-RMS ratios of the background of the phase-maps in Fig. 4.33a.

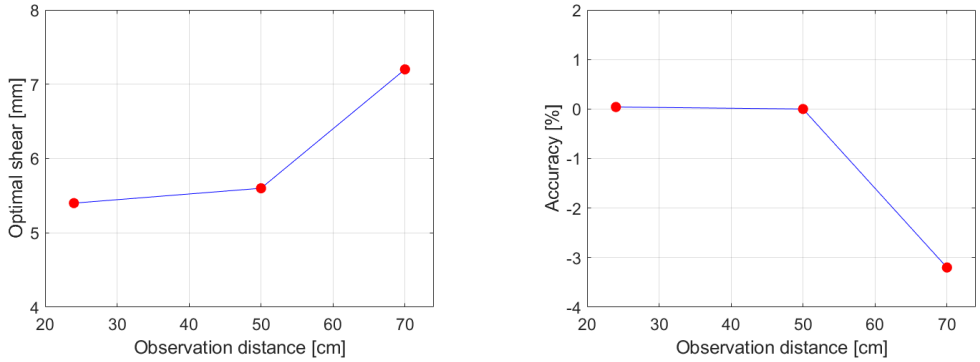

(a) *Optimal shear variation with respect to observation distance.*

(b) *Accuracy variation with respect to observation distance.*

Figure 4.35: Results obtained by varying the observation distance for a 25 mm diameter-defect localized at 1 mm depth with respect to the observed surface.

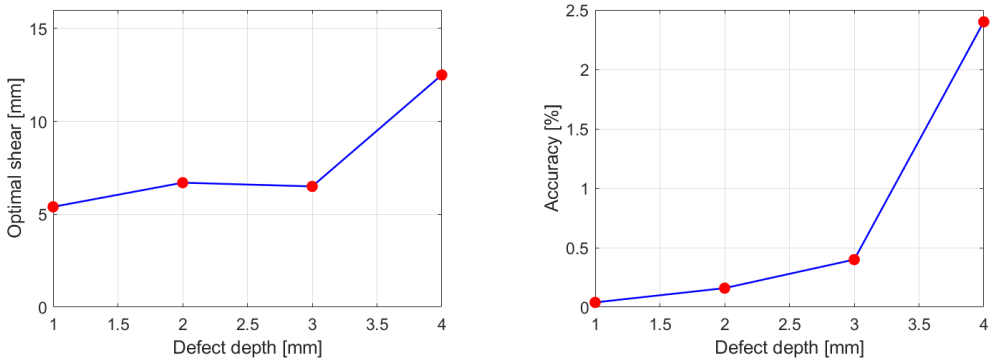

(a) *Optimal shear variation with respect to defect depth.*

(b) *Accuracy variation with respect to defect depth.*

Figure 4.36: Results obtained by varying the defect depth for a 25 mm diameter-defect observed from a distance of 24 cm.

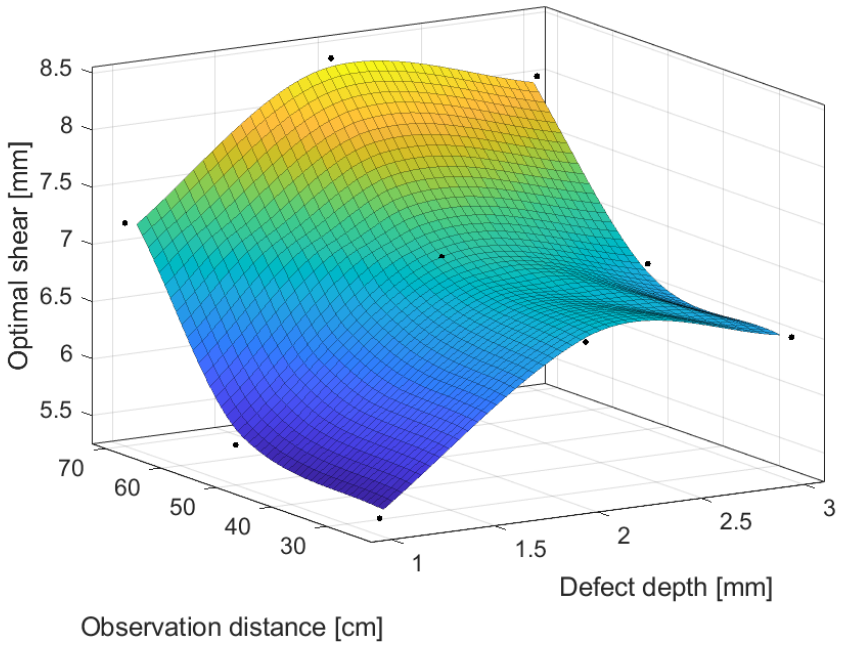

Figure 4.37: Optimal shear variation with respect to defect depth and observation distance for a defect of 25 mm diameter.

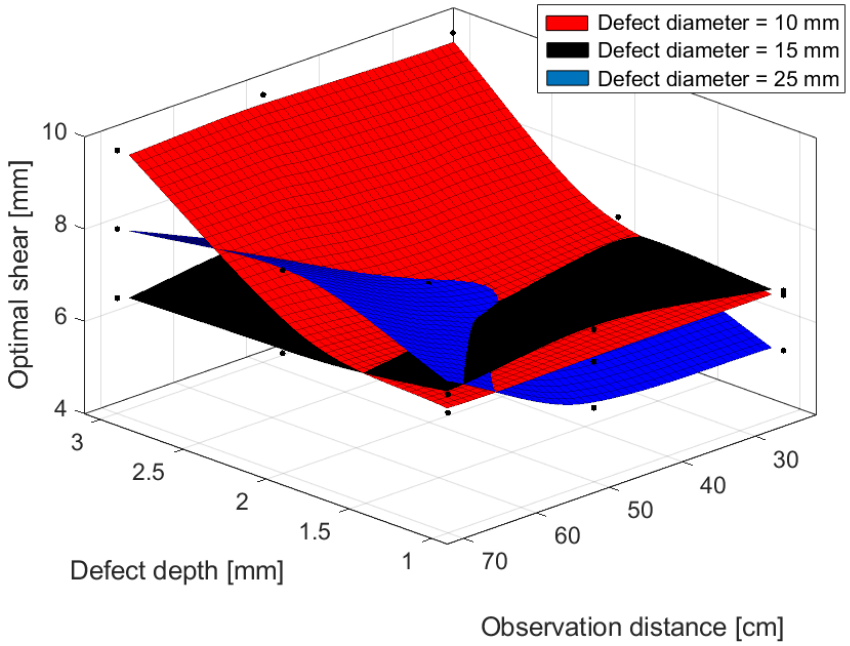

Figure 4.38: Optimal shear variation with respect to defect depth and observation distance for three different defect sizes

respect to the measurement parameters. In particular, considering the 10 mm-diameter defect, it can be noticed that the associated optimal condition is much more dependent on the defect depth rather than on the observation distance. This means that, the decrease of deformation difference between defect and background prevails on the negative effect of spatial-resolution loss occurring when the Shearocamera is moved away from the object. This is certainly in accordance with the physics of the problem: smaller and deeper defects impact to a lesser degree over displacement gradient, thus needing the device to be more performing (higher shear values). On the contrary, the 25 mm-diameter defect has an opposite behaviour: its related optimal condition depends more on spatial resolution than on depth. This is because the defect diameter is sufficient to provide good estimations even for higher depths, and the negative effect of spatial-resolution loss prevails on the the decrease of deformation difference between defect and background occurring in case of deeper defects. Finally, the 15 mm-diameter defect is not comparable with the previous ones. In fact, its optimal conditions seem quite stable with respect to measurement parameters. Therefore, it could be concluded that its $size/depth$ ratio generates

such a mechanical behaviour that balances the parameters' influence.

The through analysis of results just performed highlights that the definition of optimal conditions is strictly case-dependent. Hence, two possible options could be exploited by the operator:

1. if he has an idea about size and depth of the possible defects that may affect the inspected component, a test panel of the same material, provided with artificial defects, could be examined as preliminary phase in order to define the optimal conditions. In this way, during the inspection on the actual component, only the load-cycles phase of the developed procedure has to be carried out, while shear to set and, where appropriate, observation distance are indicated by distributions like the one in Fig. 4.38.

2. the entire procedure can be repeated each time a component has to be inspected. All the parameters' combinations (shear, load and, if needed, observation distance) are tested and the actual defect size is retrieved. This option can be chosen either if the user has no idea about the possible, detectable defects, or if he wants to avoid errors due to differences between the test panel and the actual component.

Both these options must be carried out, in any case, after performing the preliminary operations described in Sec. 4.3.1.

Chapter 5

Validation and application of the procedure in real case studies

In this Chapter, the robustness, reliability and repeatability of the developed procedure, described in Chapter 4, are checked. The validation is performed by considering three different real case studies, where artificial defects of unknown size affect the three following, different composite panels:

1. a sandwich panel composed by a honeycomb core and a carbon fiber skin, where Teflon inserts were put between sub-superficial layers (Fig. 5.1a);
2. a sandwich panel composed by a honeycomb core a fiberglass skin , where a sub superficial delamination is present (Fig. 5.1b);
3. a carbon thin plate affected by teflon inserts (Fig. 5.1c).

In order to have a comparative measurement for validating the results produced by the Shearography procedure developed, all the three defects were subjected to a non-contact Ultrasound Scanning [62], [63], [64], [65], using electro-capacitive air-coupled ultrasonic transducers with a central frequency around 200 kHz and an active area of 19 mm in transmission mode. The Ultrasound beam size was 19 mm, while the scanning resolution was provided by a Cartesian robot and corresponds to 0.2 mm. Moreover, in order to improve the Signal to Noise Ratio, 200 averages are computed for each point. The measurement was performed within the focal zone of the ultrasonic beam in order to work in the region with the highest resolution

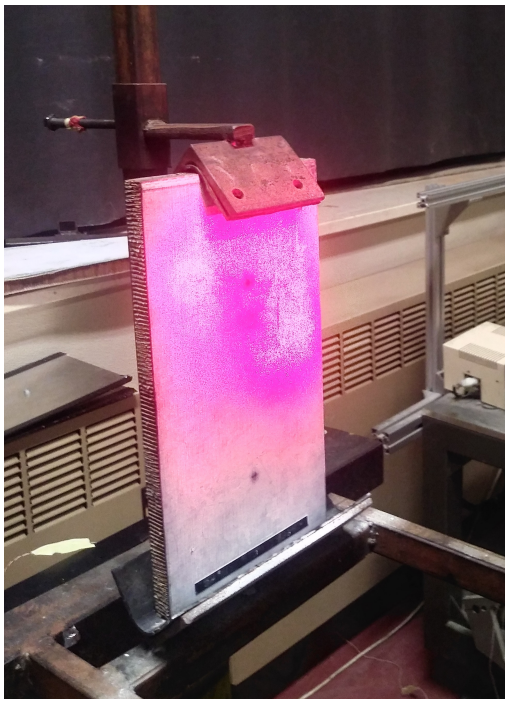

(a) *Sandwich panel composed by a honeycomb core and carbon fiber skin.*

(b) *Sandwich panel composed by a honeycomb core and fiberglass skin.*

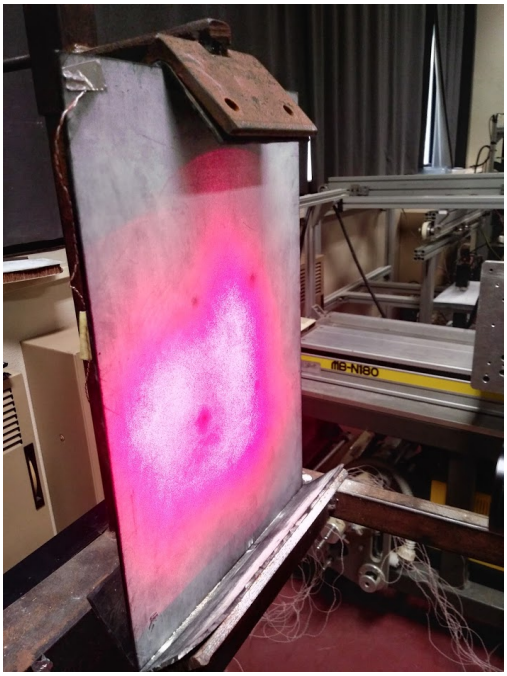

(c) *Carbon thin plate.*

Figure 5.1: Real case studies used for validating the Shearography measurement procedure.

achievable. This zone is localized in the neighborhood of the Near Field Distance, given by the following formulation:

$$N = \frac{D^2}{4\lambda}, \tag{5.1}$$

where: D is the probe diameter and λ is the wavelength of the ultrasonic beam. Furthermore, the mentioned resolution is influenced by different parameters, such as: probe characteristics (frequency, diameter, ultrasound beam distribution), interaction of beam path with the layers and material surface, thresholding algorithms used [66], [67]. Therefore, a reference sample with known defects would be necessary to estimate carefully the accuracy of the ultrasound system. However, in this case, since the ultrasound technique is used just to compare and confirm the Shearography results, a lateral resolution of 1.9 mm can be considered in the C-scan, computed by taking into account the known characteristics of the probes, the fact that the inspected panel lies within the focal zone, and the thresholding algorithms suggested used in literature. With regard to the latter ones, since the chosen threshold can consistently change the defect area results, attention was paid in this work in order to reduce errors due to these aspects. In particular, the focus was put both on classical, automatic thresholding methods discussed in [67] and in amplitude-drop methods typically used in Ultrasound flaw detection. In particular, in [68] a comparison is made between results provided by a -6 dB drop and a -12 dB drop, highlighting that in general a -6 dB threshold underestimates results, while the best accuracy is obtained with a -12 dB threshold. However, in the same paper, it is also specified that this assumption is valid mainly for flaws larger than the 80% of the active aperture while, for smaller flaws, thresholding by a -6 dB drop can avoid the effect of the probe diameter to prevail on the actual defect size, thus avoiding to commit overestimation. The comparison between drop methods and standard segmentation algorithms, showed a full correspondence between the latter and the -12 dB drop. Consequently, for defect diameters larger than the 80% of the active aperture, standard segmentation methods and drop methods are interchangeable. On the contrary, for defect diameters smaller than the 80% of the active aperture, standard segmentation methods are not reliable and -6 dB drop thresholding must be adopted.

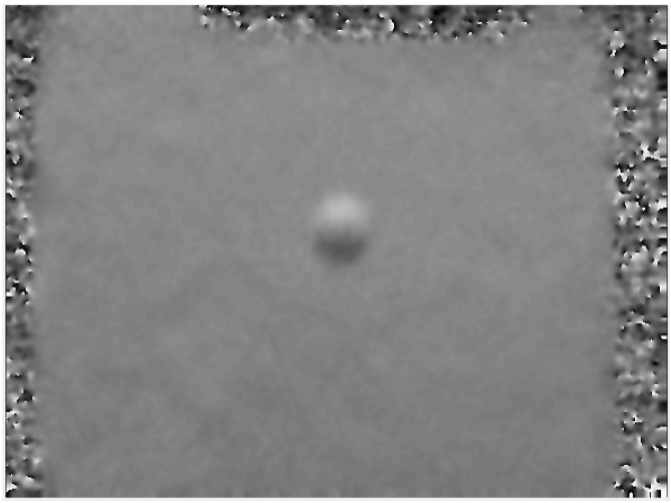

Figure 5.2: Phase-map of the sandwich panel composed of honeycomb core and carbon fiber skin.

5.1 Sandwich 1: honeycomb core and carbon fiber skin

The very same procedure discussed in Chapter 4 was performed for the inspection of this first test case. The observation distance was set to 24 cm, in order to have the best spatial resolution achievable. Fig. 5.2 shows an example of a phase-map frame associated to this panel. As the defect is very close to the object surface, its deformation can be very well appreciated. In fact, after reaching the maximum displacement-gradient difference between defect and background, the equilibrium between defect and entire structure persists for a much longer time with respect to the PVC panel used for developing the procedure itself, whose behaviour was already expressed in Fig. 4.26a. The quantity $\left(\frac{\partial w}{\partial x}_{max} - \frac{\partial w}{\partial x}_{min}\right)_{defect} - \left(\frac{\partial w}{\partial x}_{max} - \frac{\partial w}{\partial x}_{min}\right)_{background}$ for the sandwich panel composed of honeycomb core and carbon fiber skin is reported in Fig. 5.3. In this regard, the accumulation point between the deformation trend and the defect-size trend, matched in Fig. 5.4, results much denser, giving the kernel-based probability density function reported in Fig. 5.5. Tab. 5.1 reports the results obtained by the entire procedure, representing the parabolic behaviour shown in Fig. 5.6, while Tab. 5.2 highlights the optimal, found shear and, consequently, the best defect-size estimation achievable in the

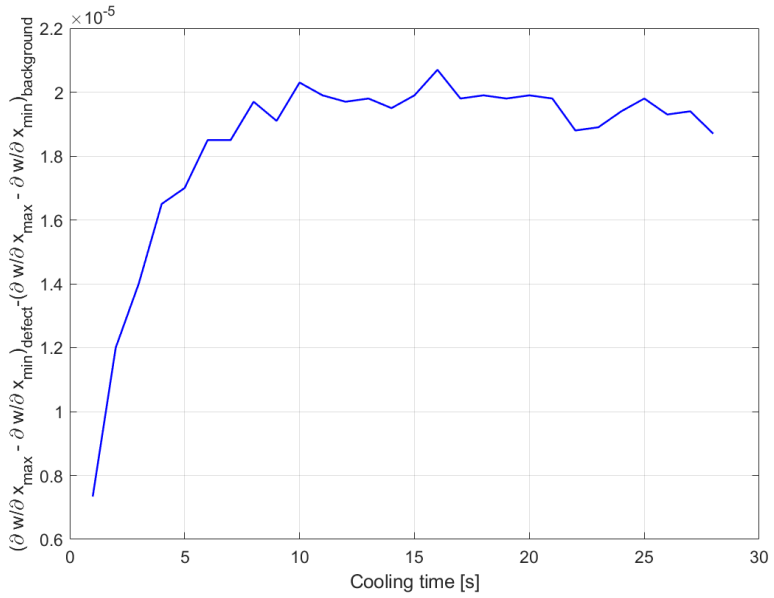

Figure 5.3: Difference between defect and entire structure in terms of out-of-plane displacement gradient.

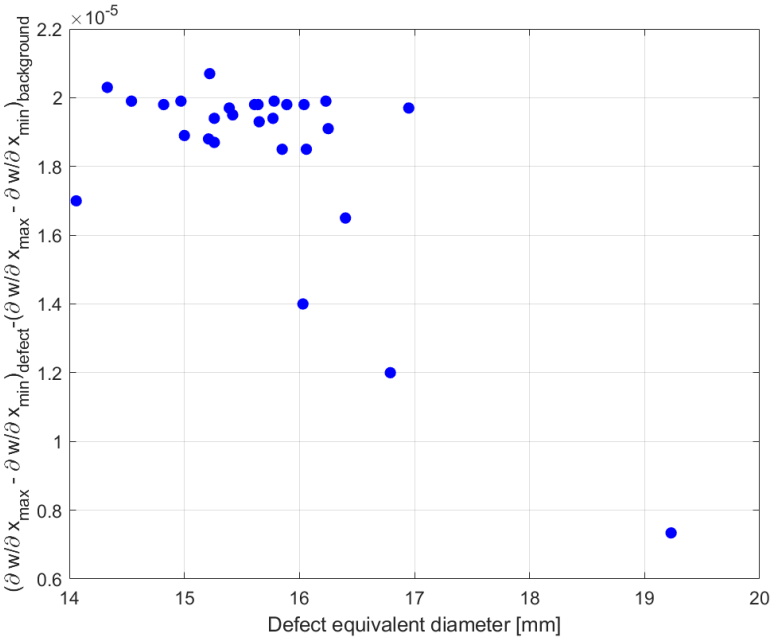

Figure 5.4: Displacement gradient difference vs defect size for the sandwich panel composed of honeycomb core and carbon fiber skin.

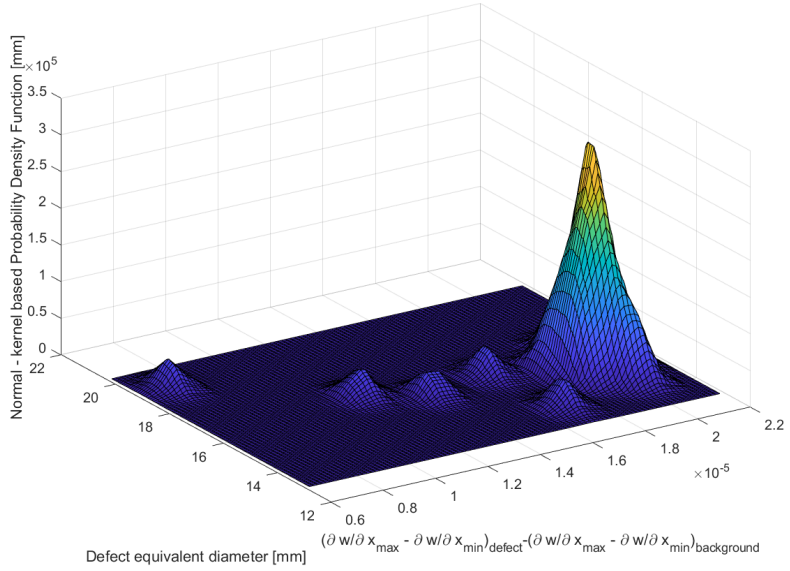

Figure 5.5: Example of kernel-based probability density function for the sandwich panel composed of honeycomb core and carbon fiber skin.

Table 5.1: Statistical results for the sandwich panel composed of honeycomb core and carbon fiber skin.

Computed shearing amount [mm]	**Statistically-chosen defect size [mm]**	**Statistically-chosen heating time [s]**
2.7	18.0	5
4.7	15.8	5
9.7	18.20	5

corresponding condition. Fig. 5.7 shows the morphology reconstruction of the inspected defect. Compared to the reconstruction obtained for the PVC panel studied in Chapter 4 and reported in Fig. 4.25, here the defect boundaries appear more disturbed. This is because the honeycomb cells, distributed within the entire structure, have an effect on the overall deformation and noise, providing a superimposition of effects, which disturbs the defect reconstruction. However, since the procedure itself requires to follow the warping evolution of the defect during the cooling phase and to use the corresponding results by a statistical approach, the disturbing dynamical effects are compensated, and the final results

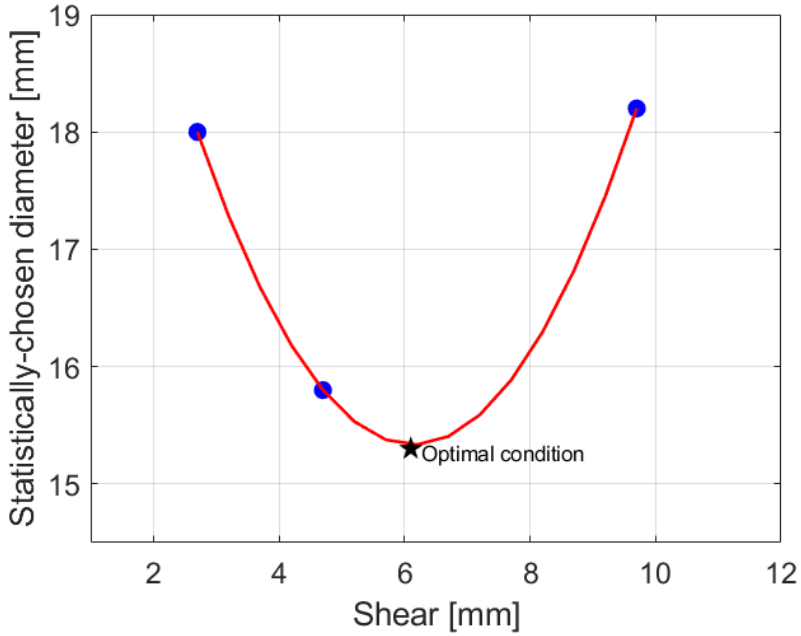

Figure 5.6: Graphical distribution of results for the defect detected in the sandwich panel composed of honeycomb core and carbon fiber skin.

Table 5.2: Optimal condition for the defect detected in the sandwich panel composed of honeycomb core and carbon fiber skin.

Optimal shear[mm]	**Defect expected dimension if the optimal shear were used [mm]**
6.1	15.3

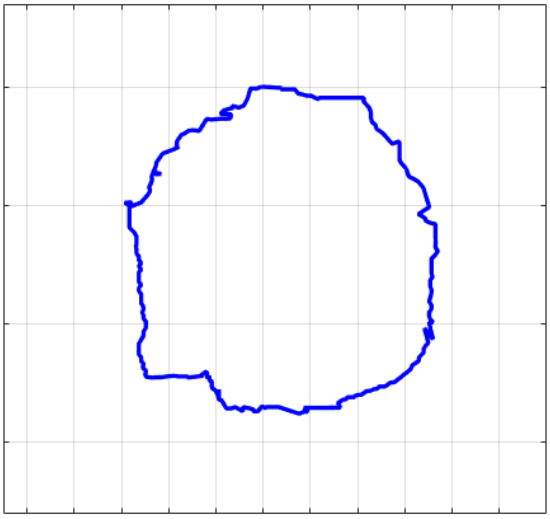

Figure 5.7: Morphology reconstruction of the sandwich panel composed of honeycomb core and carbon fiber skin.

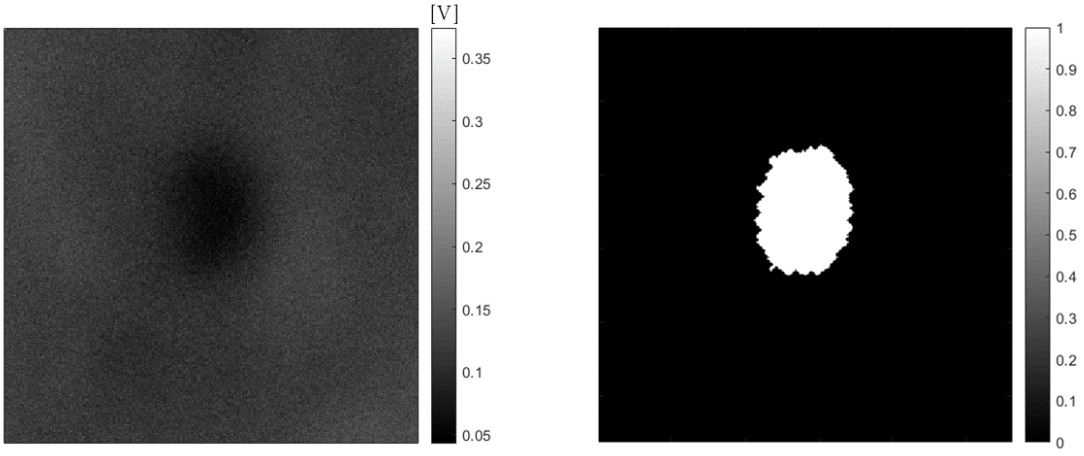

Figure 5.8: Ultrasound scanning data. On the right, the Ultrasound amplitude signal in [V]. On the left, the corresponding binarized image.

Table 5.3: Comparison between Shearography and Ultrasound results.

Shearography-detected equivalent diameter [mm]	**Ultrasound-detected equivalent diameter [mm]**
15.3	15 ± 2

are no longer affected by these problems, as confirmed by the comparison with the Ultrasound inspection, whose results are shown in Fig. 5.8. Here the amplitude map in Volts and the corresponding segmented image are reported, while in Tab. 5.3 quantitative results of Shearography and Ultrasound techniques are summarized. It is worth to remind that, in this study, Ultrasound inspection is not supposed to be used as a reference technique, since its accuracy is not ten times higher than Shearography one. On the contrary, the purpose is just to compare two Non Destructive techniques usually used for composite inspections, highlighting the advantage of Shearography in terms of inspection time. In fact, for obtaining the reported Ultrasound amplitude maps with the used scanning resolution of 0.2 mm, three days were needed, compared to the few hours taken to carry out the developed Shearography procedures, whose rapidity could be furtherly increased by means of software optimization. From Fig. 5.8 and Tab. 5.3, a good match between the two techniques can be noticed both in terms of quantitative results and in terms of morphological reconstruction, considering also that the Ultrasound reconstruction is performed in static conditions, while Shearography one corresponds to loaded states.

5.2 Sandwich 2: honeycomb core and fiberglass skin

In this case, a complex-shaped delamination is present and localized very close to the object surface. Consequently, atypical and very dynamical fringe patterns are detected, as shown in Fig. 5.9, and lower loads are sufficient for a good detection, as reported in Tab. 5.4. As for the Sandwich panel discussed in Sec. 5.1, also in this case the time interval in which the defect deformation is in equilibrium with the one of the entire panel is longer than the PVC stabilization range, giving the very same

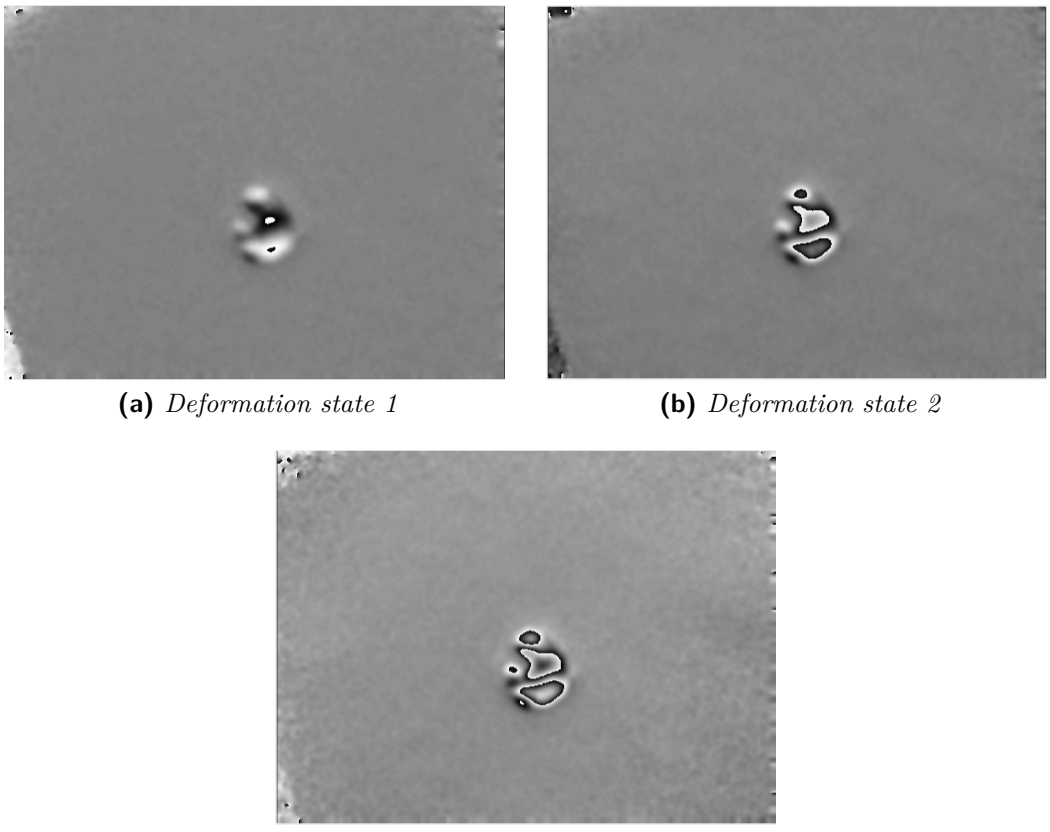

(a) *Deformation state 1*

(b) *Deformation state 2*

(c) *Deformation state 3*

Figure 5.9: Fringe pattern evolution for the delamination in the sandwich panel composed of honeycomb core and fiberglass skin.

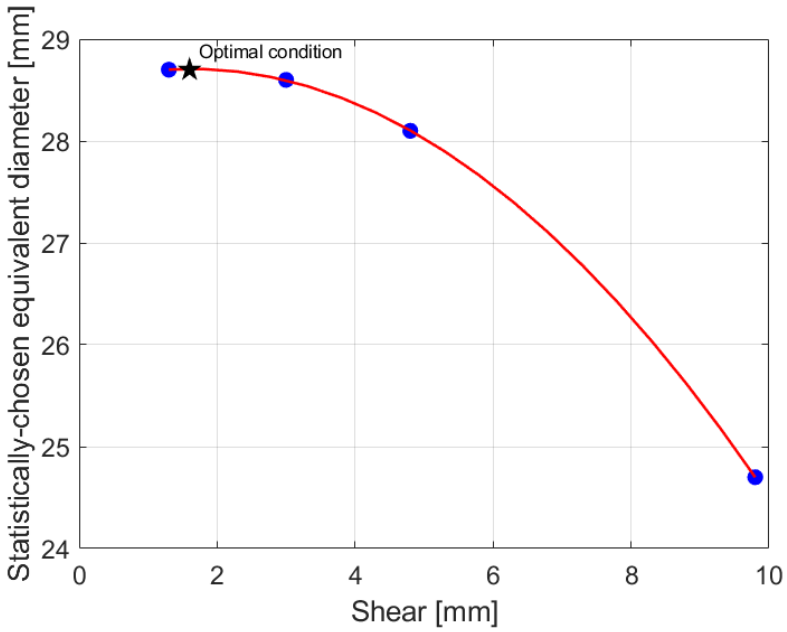

Figure 5.10: Graphical distribution of results for the defect detected in the sandwich panel composed of honeycomb core and fiberglass skin.

trends of Fig. 5.3 and Fig. 5.5. In contrast with the results obtained up to now for the PVC specimen and the Sandwich panel 1, in this case a facing-down concavity parabola is obtained, as it can be seen in Fig. 5.5. For being sure of the reliability of results, this time a fourth shear value has been tested, and the corresponding results confirmed to be confident with the other ones, see again Fig. 5.5. Therefore, in this case, the optimal condition will coincide with the maximum of the parabola. Tab. 5.4 reports the results obtained by the entire procedure, representing the parabolic behaviour shown in Fig. 5.10, while Tab. 5.5 highlights the optimal, found shear and, consequently, the best defect-size estimation achievable in the current condition. The fact that this time the optimal condition is detected at lower shear is in accordance with the fact that the defect was the closest to the inspected surface among other case studies, thus generating higher deformations, thus needing lower sensitivity in turn. Fig. 5.11 shows the morphological reconstruction of the examined defect, highlighting its complexity in terms of shape, as confirmed by the ultrasound inspection described in the following. The image to the right of Fig. 5.12 shows the amplitude signal in Volts obtained by defect scanning, while the image to the left is the corresponding binarized image used for area computation.

Table 5.4: Statistical results for the sandwich panel composed of honeycomb core and carbon fiber skin.

Computed shearing amount [mm]	Statistically-chosen defect size [mm]	Statistically-chosen heating time [ms]
1.3	28.7	10
3.0	28.6	10
4.8	28.1	10
9.8	24.7	10

Table 5.5: Optimal condition for the defect detected in the sandwich panel composed of honeycomb core and carbon fiber skin.

Optimal shear[mm]	Defect expected dimension if the optimal shear were used [mm]
1.6	28.6

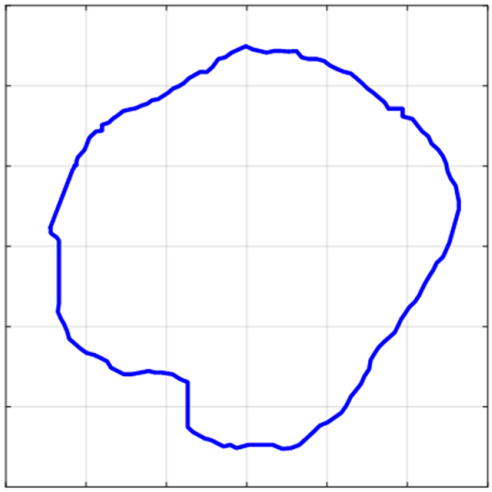

Figure 5.11: Morphology reconstruction of the sandwich panel composed of honeycomb core and fiberglass skin.

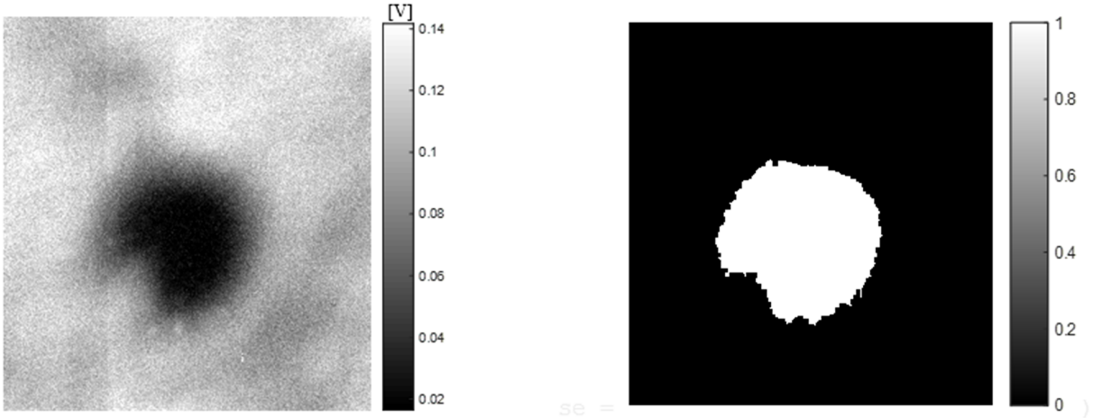

Figure 5.12: Ultrasound scanning data. On the right, the Ultrasound amplitude signal in [V]. On the left, the corresponding binarized image.

Table 5.6: Comparison between Shearography and Ultrasound results.

Shearography-detected equivalent diameter [mm]	**Ultrasound-detected equivalent diameter [mm]**
28.6	28 ± 2

From the latter, it can be noticed that the morphological reconstruction performed by Shearography is comparable with the shape highlighted by ultrasound scanning. With regard to size computation from ultrasound inspection,results show a defect size of 28 ± 2 *mm*. Tab. 5.6 reports this quantitative result and compares it with the Shearography-detected equivalent diameter, whose value is 28.6 *mm*. Again, since the ultrasonic inspection has not the requisites for being used as reference image (its accuracy is not 10 times higher than the Shearography one), the objective is just to confirm that the procedure developed for Shearography inspection gives results confident with those of other full-field non-contact techniques, even for complex-shaped defects.

5.3 Carbon thin plate

The carbon thin plate discussed in this Section is affected by a teflon insert. The stiffness of this component is such that the differences between the defect and the

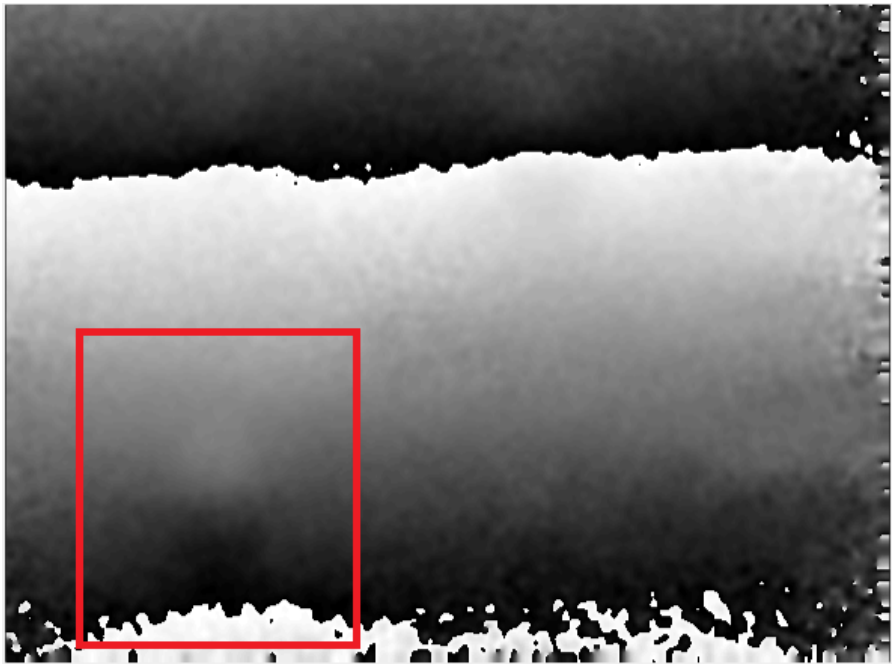

Figure 5.13: Example of a phase-map frame for the carbon thin plate with teflon insert.

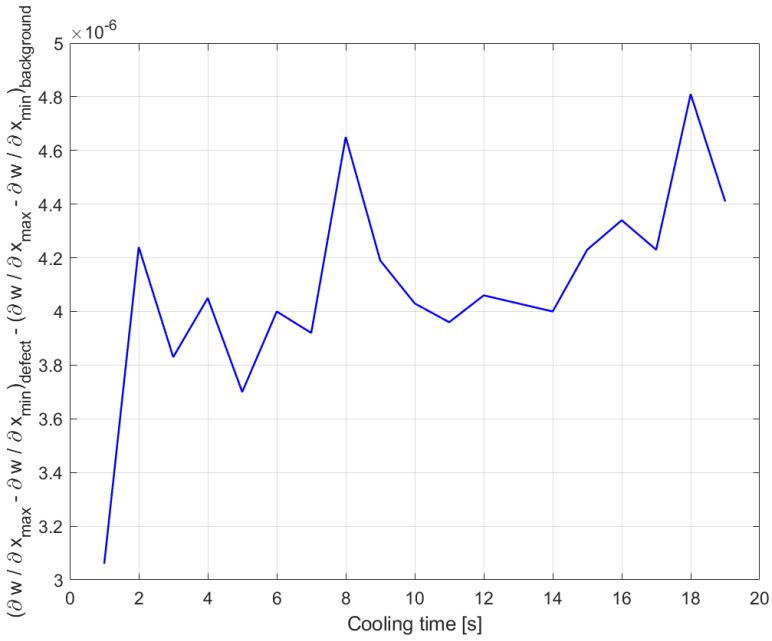

Figure 5.14: Time evolution of the differences between defect and entire structure in terms of out-of-plane displacement gradient for the carbon test panel with teflon inserts.

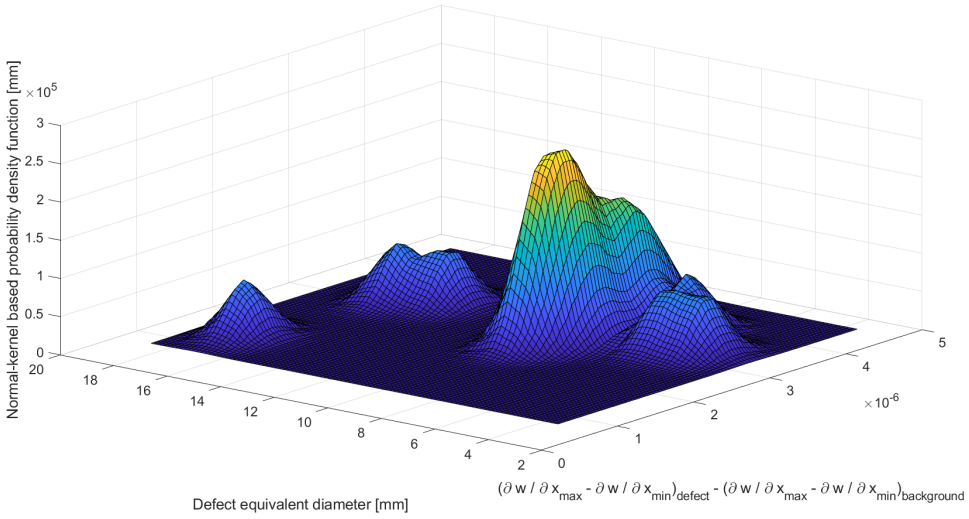

Figure 5.15: Example of kernel-based probability density function for the carbon thin plate with teflon insert.

entire component in terms of out-of-plane displacement gradient are very low and at the limit of resolution, as can be noticed in Fig. 5.14. Here, in fact, the reported plot corresponds to a shear of 10 mm thus, to the following resolution, according to Eq. 4.7:

$$res = \frac{0.03}{1000 * 10} = 3 \cdot 10^{-6}. \tag{5.2}$$

Therefore, it appears clear that the differences between the out-of-plane displacement gradients in Fig. 5.14 are of the same order of magnitude as the resolution. This significantly worsens defect detection, since the Signal to Noise Ratio is much lower with respect to the previous case studies. The low contrast between defect and background can also be checked in Fig. 5.13, where the studied defect is marked by a red rectangle. The lower quality of the detection can be also checked by the kernel-based probability density function in Fig. 5.15: in this case, the pdf has a multimodal distribution with secondary peaks comparable with the maximum one, meaning that data have considerably low-quality. In any case, the procedure has been carried out and the developed algorithm has been able to trace the parabolic behaviour, providing the results reported in Tab. 5.7 and Tab. 5.8 and shown in Fig. 5.16. An example of morphological reconstruction obtained for a given time instant during the cooling phase is reported in Fig. 5.17, where the detected

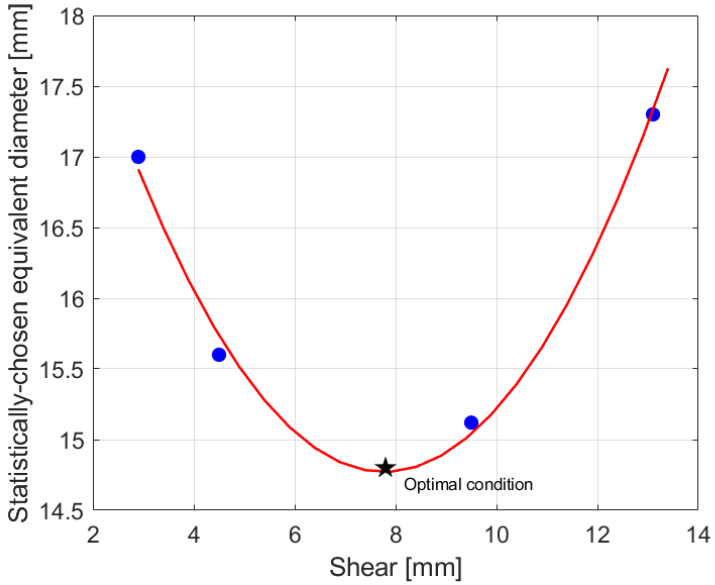

Figure 5.16: Graphical distribution of results for the defect detected in the carbon thin plate.

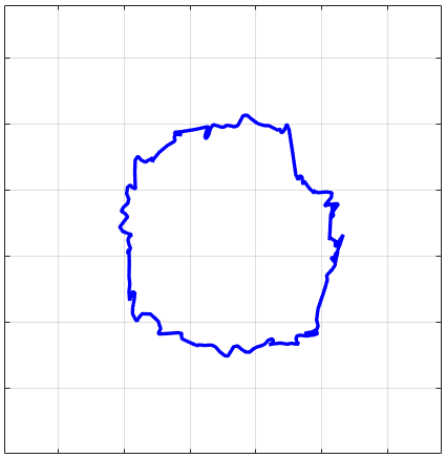

Figure 5.17: Morphological reconstruction for the defect detected within the carbon thin plate.

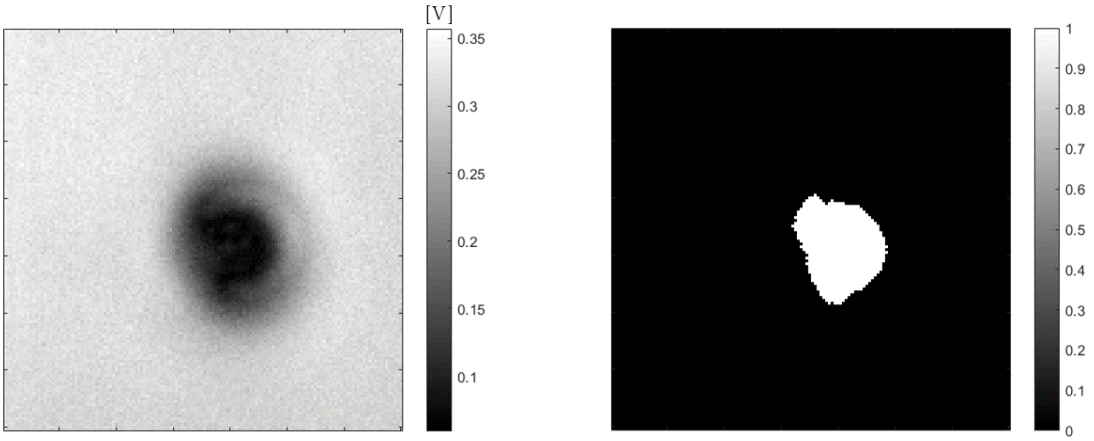

Figure 5.18: Ultrasound scanning data. On the right, the Ultrasound amplitude signal in [V]. On the left, the corresponding binarized image.

Table 5.7: Statistical results for the carbon thin plate.

Computed shearing amount [mm]	**Statistically-chosen defect size [mm]**	**Statistically-chosen heating time [ms]**
2.9	17.0	15
4.5	15.6	15
9.5	15.12	3
13.1	17.3	3

Table 5.8: Optimal condition for the defect detected in the carbon thin plate.

Optimal shear[mm]	**Defect expected dimension if the optimal shear were used [mm]**
7.8	14.8

Table 5.9: Comparison between Shearography and Ultrasound results.

Shearography-detected equivalent diameter [mm]	**Ultrasound-detected equivalent diameter [mm]**
14.8	13 ± 2

noisy boundaries are shown. Therefore, also for this case study it is possible to compare Shearography results with those obtained by Ultrasound Scanning, reported in Fig. 5.18 and in Tab. 5.9. From the comparison it can be noticed that, despite the low Signal to Noise Ratio achievable in Shearography measurement, the associated morphological and quantitative results have a great correspondence with Ultrasound inspection.

In conclusion, it can be stated that it is possible to obtain valid and reliable results by the developed Shearographic quantitative measurement procedure, even for complex cases having poor SNRs with displacement gradients at the limit of resolution.

Chapter 6

Discussion about metrological aspects of the method

In this Chapter all the aspects tackled in the previous Chapters are developed from the point of view of measurement uncertainty, accuracy and repeatability. More precisely, the following discussion aims at highlighting the negative influence of measurement parameters towards uncertainty and accuracy in cases where the procedure developed in this PhD thesis is not carried out. This will provide a quantitative evidence of the advantages of applying the discussed procedure.
The main idea consists in considering some representative data-sets among the ones discussed in Chapter 4 and Chapter 5 and to compute the defect size uncertainty considering different combinations of variables, so as to observe the effect of each parameter one at a time. As mentioned many times in this thesis, the main parameters influencing Shearography inspections are: shear, observation distance, defect size and depth. Consequently, the estimation of the effects on uncertainty of these parameters will be performed by:

1. fixing defect size and depth and observation distance, so as to observe the influence of the shear amount;

2. fixing defect size and depth and shear amount, so as to observe the influence of the observation distance;

3. fixing shear amount, defect size and observation distance, so as to observe the influence of defect depth;

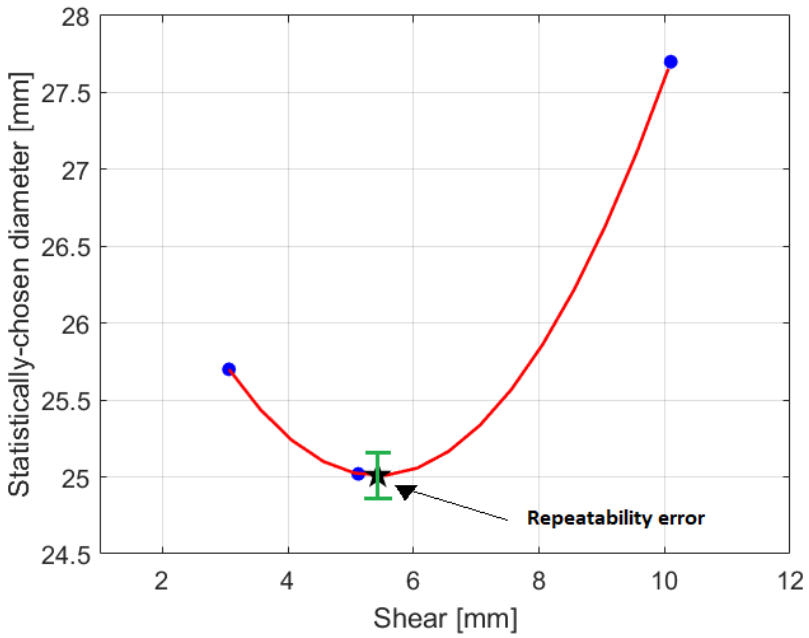

Figure 6.1: Graphical representation of the repeatability error of the vertex of the parabola.

4. fixing shear amount, defect depth and observation distance, so as to observe the influence of defect size;

5. fixing shear amount, defect depth, observation distance, defect size so as to observe the influence of load.

This workflow will be developed both for the PVC test panel used for developing the procedure itself, as shown in Chapter 4, and for the composite case studies discussed in Chapter 5.

6.1 Repeatability

Before considering the effect of each variable towards measurement results, it is necessary to estimate the method repeatability, hence the error of repeatability while computing the vertex of the optimization parabola, an example of which is reported in Fig. 6.1. As defined in the *Guide to the expression of Uncertainty in Measurement* (GUM) [69], repeatability represents the closeness of the agreement

between the results of successive measurements of the same measurand carried out under the same conditions of measurement, i.e.:

- the same measurement procedure ;
- the same observer :
- the same measuring instrument, used under the same conditions;
- the same location ;
- repetition over a short period of time.

The repeatability error E_{rep} can be computed as:

$$E_{rep} = V_{max} - V_{min}, \tag{6.1}$$

where V_{max} and V_{min} are respectively the maximum and the minimum measured value among a series of measurements in the conditions mentioned above.
In addition, due to the fact that the definition of a confidence level for the vertex of the parabola would require a huge number of repetitions of the entire measurement procedure, the estimation of repeatability can be also exploited for the computation of uncertainty, as uncertainty of type B. As defined by the GUM [69], Type B method performs evaluation of uncertainty by means other than the statistical analysis of series of observations. Therefore, considering a rectangular probability density function, the standard deviation can be computed as:

$$\sigma = \frac{E_{rep}}{2 \cdot \sqrt{3}}. \tag{6.2}$$

In order to perform this kind of analysis, seven repetitions were carried out considering the 25 mm-diameter defect observed from a distance of 24 cm (the one corresponding to the best spatial resolution, so as to not be conditioned by the distance effect) in the same conditions of the vertex of the parabola represented in Fig. 6.1, summarized in Tab. 4.4. As required by the procedure, for each of the seven repetitions results were found by detecting the accumulation of data in the bivariate PDF given by the defect size and relative deformation variations during the cooling phase. Results are reported in Tab. 6.1. According to these data, the

Table 6.1: Results obtained by seven repetitions corresponding to optimal conditions reported in Tab. 4.4.

Shear y [mm]	**Shear x [mm]**	**Calibration factor [mm/pixel]**	**Defect equivalent diameter in the accumulation point [mm]**
5.43	0.10	0.09	25.01
5.26	0.14	0.09	25.05
5.26	0.14	0.09	24.98
5.27	0.11	0.09	24.98
5.27	0.11	0.09	25.05
5.27	0.11	0.09	25.06
5.27	0.11	0.09	24.99

repeatability error is:

$$E_{rep} = 25.06 - 24.98 = 0.08mm \tag{6.3}$$

and the corresponding standard deviation:

$$\sigma = \frac{0.08}{2 \cdot \sqrt{3}} = 0.02mm. \tag{6.4}$$

Therefore, $\pm 0.02\ mm$ can be considered as the standard deviation associated to the optimal value corresponding to the vertex of the determined parabola. This value coincides with the total uncertainty if shear is the only parameter to vary. Otherwise, this value must be combined with uncertainty generated to the variation of other measurement parameters, for example observation distance.

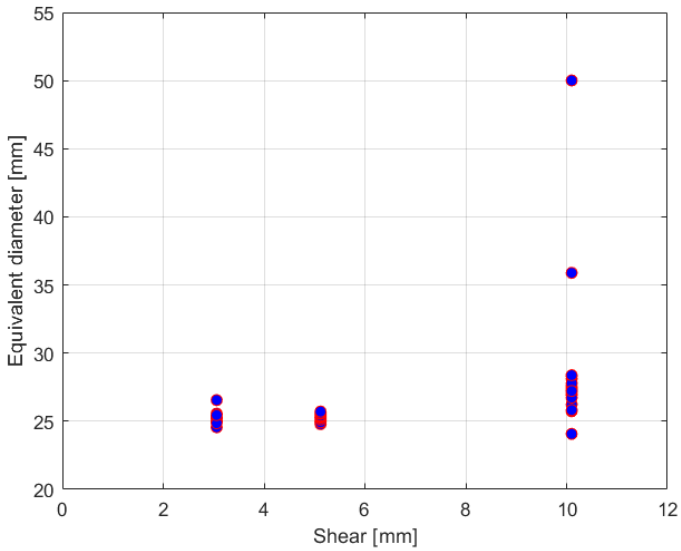

Figure 6.2: Data distribution for a defect of 25 mm positioned at 1 mm from the surface, observed from a distance of 24 cm by using different shear values.

6.2 Evaluation of the influence of measurement parameters on uncertainty and accuracy for the PVC test panel

Since uncertainty evaluation will be performed by treating the data-sets as generic point distributions, thus not by processing them by the method proposed in Chapter 4, data belonging to the entire cooling phase will be considered, without selecting the stabilization region. This will confirm that in this work advantages both in terms of uncertainty and of accuracy have been reached.

6.2.1 Effect of shear variation on measurement uncertainty

As representative data-sets, the ones corresponding to the 25 mm-diameter defect observed from a distance of 24 cm were chosen and the variation of results with the shear amount was observed. As in Chapter 4, the used shear values are: 3 mm, 5 mm and 10 mm. Fig. 6.2 shows the variability of results as the shear amount varies. This distribution corresponds to a mean equivalent diameter of 26 mm with a standard deviation of $\pm$ 3 mm. On the contrary, the application

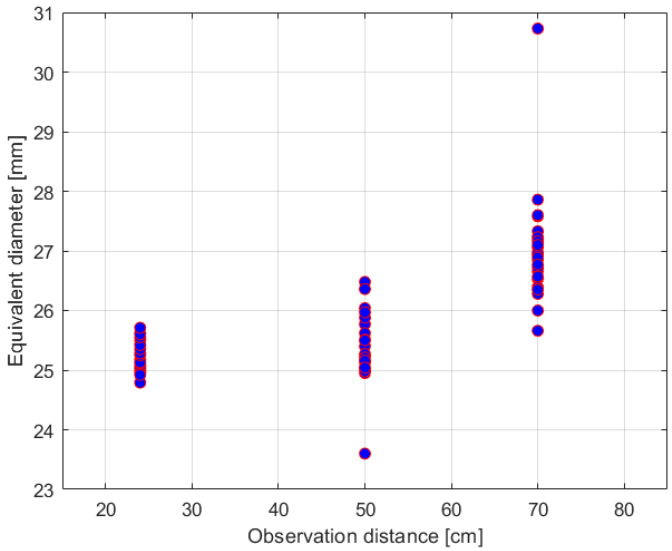

Figure 6.3: Data distribution for a defect of 25 mm positioned at 1 mm from the surface, observed from a variables distance by using a shear value of 5 mm.

of the developed measurement procedure provides an equivalent diameter of 25.01 mm in optimal conditions, corresponding to a shear of 5.43 mm. In addition, the use of our procedure, that works by finding the cooling stabilization regions as accumulation points in data distributions, revealed that uncertainty within the stabilization region corresponds to 0.02 mm, as discussed in Sec. 6.1. This latter value can be used as an indication of uncertainty for each vertex of the parabolas in Chapter 4, see for example the one in Fig. 4.31. In fact, ones the data-sets corresponding to different parameters combinations are processed by the studied procedure, the mentioned parameters themselves stop to influence final results, that remain influenced only by the repeatability error of the procedure for defect size and morphological reconstruction that guarantee, indeed, an uncertainty of $\pm$ 0.02 mm.

6.2.2 Effect of observation distance variation on measurement uncertainty

Fig. 6.3 shows the data distributions obtained by varying observation distance for a defect of 25 mm positioned at 1 mm from the surface. By considering

Table 6.2: Optimal conditions detected by the studied procedure for different observation distances.

Observation distance [cm]	Statistically-chosen defect size [mm]
24	25.01
50	25.00
70	24.2

the raw data without applying the developed measurement procedure, the mean equivalent diameter is 26 mm with an uncertainty of ± 1 mm. On the contrary, in Tab. 6.2 results obtained by our procedure for different observation distances are summarized. Considering these three data-points, a mean diameter of 24.70 mm is obtained with a standard deviation of ± 0.40 mm. This standard deviation must be combined to the one given by the repeatability of the procedure, in order to obtain the total standard deviation σ_{tot}. This is given by the following formula [69], being repeatability and observation distance independent parameters:

$$\sigma_{tot} = \sqrt{\sum_{i=1}^{N} c_i^2 \sigma_{X_i}^2}, \tag{6.5}$$

where N is the number of uncertainties to combine, c_i are sensitivity indexes and can be defined as a sort of weight for the considered parameter. This allows to give more importance to the standard deviation of a certain variable (σ_{X_i}) rather than another. In this analysis all sensitivity parameters are set to 1. Therefore, the total standard deviation for this case is given by:

$$\sigma_{tot} = \sqrt{\sum_{i=1}^{N} 0.40^2 + 0.02^2} \approx 0.40mm. \tag{6.6}$$

It is clear, for this case, that the effect of the variation of the observation distance largely prevails on the error of repeatability.

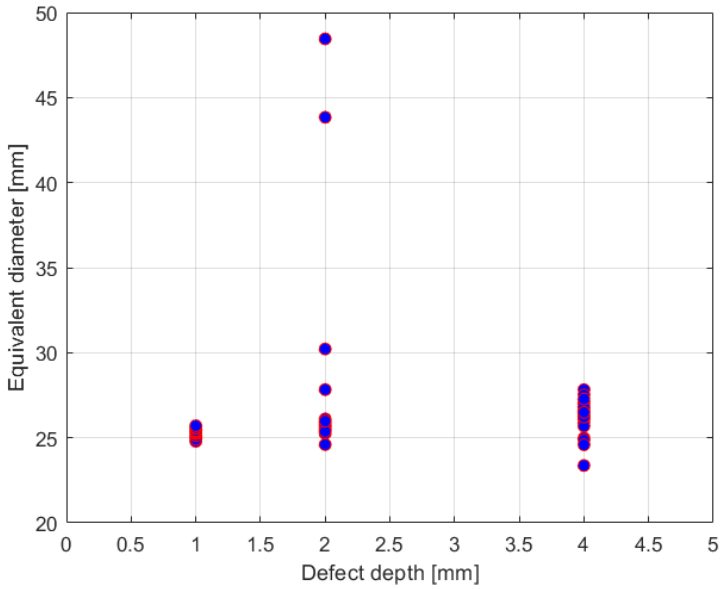

Figure 6.4: Data distribution for a defect of 25 mm positioned at variable depth from the surface, observed from a distance of 24 cm by using a shear value of 5 mm.

Table 6.3: Optimal conditions detected by the studied procedure for different depths.

Defect depth [mm]	Statistically-chosen defect size [mm]
1	25.01
2	25.04
4	25.6

6.2.3 Effect of defect depth variation on measurement uncertainty

In this Section, the effect of the defect position inside the thickness of the material (1, 2 and 4 mm) is discussed, by fixing defect dimension (diameter of 25 mm), shear (5 mm) and observation distance (24 cm). Results are shown in Fig. 6.4, and correspond to a mean diameter of 26.00 mm with a standard deviation of ± 3.00 mm. On the other hand, Tab. 6.3 shows results obtained by the developed procedure for the three depths. By using results of Tab. 6.3, the mean equivalent diameter is 25.2 with an uncertainty of ± 0.3 mm. As for the case of the variation

Table 6.4: Results for different defect dimensions corresponding to a usual use of Shearography, without exploiting the procedure developed in this work.

Defect mean diameter [mm]	σ **[mm]**
11.0	$\pm$ 0.3
17.0	$\pm$ 2.0
25.1	$\pm$ 0.2

Table 6.5: Optimal conditions for different defect dimensions, obtained by exploiting the procedure developed in this work.

Defect reference diameter [mm]	**Equivalent diameter [mm]**
10.00	10.20
15.00	14.90
25.00	25.01

of the observation distance, this value prevails on the uncertainty due to the repeatability error, for Eq. 6.5. Therefore, a significant uncertainty reduction is achieved compared to a non-procedural data processing.

6.2.4 Effect of defect size variation on measurement uncertainty

In this last case, the effect of processing defects of different size is investigated, by fixing the defect position inside material thickness (1 mm), the observation distance (24 cm) and the shear amount (5 mm). The minimum observation distance was chosen for this study among the ones used in the performed tests, in order not to be conditioned by resolution losses corresponding to higher distances. In Fig. 6.5 data distributions corresponding to different defect dimensions are reported, while in Tab. 6.4 the relative mean diameters and standard deviations σ are summarized. On the contrary, Tab. 6.5 reports results obtained by using the measurement procedure developed in this thesis, confirming the increase of accuracy achievable by its application. The measurement uncertainty corresponding to the determined optimal conditions, as already mentioned in Sec. 6.2.1 corresponds to the uncertainty detected by the repeatability error, i.e. $\pm$ 0.02 mm.

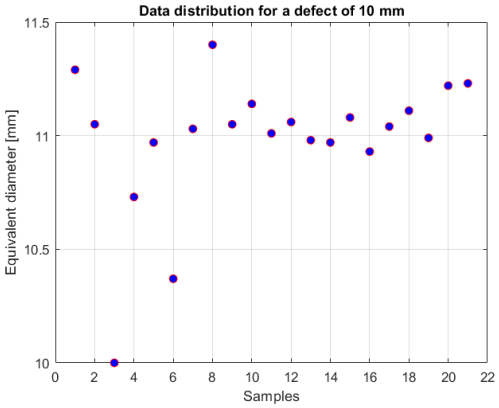

(a) *Data distribution for a defect of 10 mm-diameter observed from a distance of 24 cm by using a shear value of 5 mm and positioned at 1 mm depth from the observed surface.*

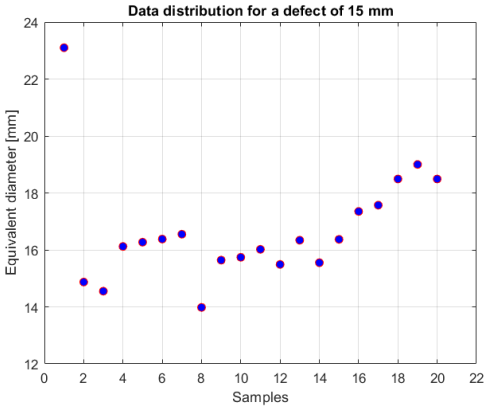

(b) *Data distribution for a defect of 15 mm-diameter observed from a distance of 24 cm by using a shear value of 5 mm and positioned at 1 mm depth from the observed surface.*

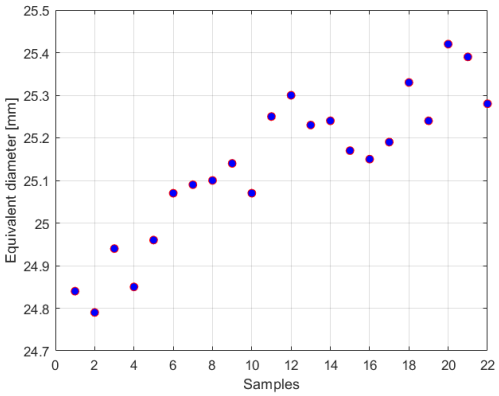

(c) *Data distribution for a defect of 25 mm-diameter observed from a distance of 24 cm by using a shear value of 5 mm and positioned at 1 mm depth from the observed surface.*

Figure 6.5: Different data distribution for different defect sizes under the same conditions.

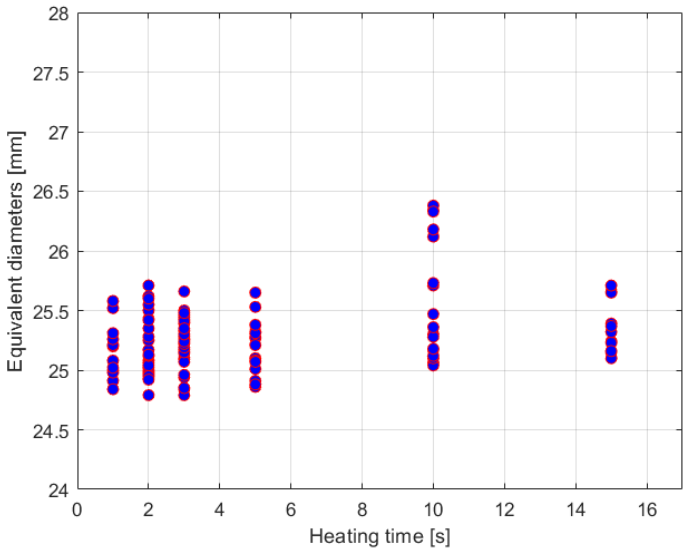

Figure 6.6: Data distribution for a defect of 25 mm positioned at 1 mm from the surface, observed from a distance of 24 cm by using a shear value of 5 mm, subjected to different loads.

6.2.5 Effect of load intensity on measurement uncertainty

The influence of load intensity on the estimation of defect dimensions has been widely discussed both in Chapter 1 and in Chapter 4. In particular, in the latter the need of choosing the right load intensity to apply so as to neither overestimating nor underestimating the actual size was discussed. In Fig. 4.26 it can be noticed that an increase of load intensity causes accumulation points to move towards higher diameters. In order to have an idea of the order of magnitude of the standard deviation achievable by varying load intensity, a defect of 25 mm diameter observed from a distance of 24 cm and located at 1 mm from the observed surface is considered. Results, reported in Fig. 6.6, show a mean diameter of 25.3 mm with a standard deviation of *pm* 1 mm. On the other hand, the developed procedure chose as most reliable load intensity a heating time of 1 s, whose corresponding data-set provides an uncertainty of $\pm$ 0.02 mm. Hence, it can be highlighted that the use of the developed procedure enabled both an improvement in terms of accuracy and in terms of uncertainty.

Table 6.6: Comparison between standard use of Shearography and the developed procedure in terms of uncertainty and accuracy.

Varying parameter: shear		**Standard use**	**Developed procedure**
	Accuracy [%]	4	0.04
	Uncertainty [mm]	± 3.00	± 0.02
Varying parameter: observ. distance		**Standard use**	**Developed procedure**
	Accuracy [%]	4	1.24
	Uncertainty [mm]	± 1.00	± 0.40
Varying parameter: defect depth		**Standard use**	**Developed procedure**
	Accuracy [%]	4	0.4
	Uncertainty [mm]	± 3.00	± 0.30
Varying parameter: defect size		**Standard use**	**Developed procedure**
	Accuracy [%]	10	2
	Uncertainty [mm]	± 0.30	± 0.02
Varying parameter: load intensity		**Standard use**	**Developed procedure**
	Accuracy [%]	1.2	0.04
	Uncertainty [mm]	± 1.00	± 0.02

6.2.6 Final discussion about uncertainty and accuracy for the PVC reference panel

Tab. 6.6 summarizes all results discussed in the previous Sections highlighting how, for each single parameter variation, a decrease of uncertainty and an improvement of accuracy are detected. In particular, the reported measurement accuracy was computed as

$$a = \Big(\frac{D_{meas}}{D_{ref}} * 100\Big) - 100, \tag{6.7}$$

where D_{meas} is the measured equivalent diameter and D_{ref} is the reference diameter. With regard to the case in which the defect size varies, in Tab. 6.6 the result corresponding to the worst case (the smallest defect size of 10 mm) is reported. The improvement of accuracy and uncertainty are expressed as percentage in Tab. 6.7.

Table 6.7: Accuracy and standard deviation improvement between standard use and developed procedure.

Varying parameter	**Accuracy improvement** [%]	**Uncertainty reduction** [%]
Shear	99	99
Observation distance	69	60
Defect depth	90	90
Defect size	80	93
Load intensity	97	98

Here it can be noticed that the lowest improvement corresponds to the case in which the observation distance increases. In fact, despite the optimization process, the loss of spatial resolution jeopardizes data a priori, affecting the positive effect of the optimization procedure. Once analyzed the single effect of each parameter on both uncertainty and accuracy, it is worth to consider the combination of all the measurement parameters (shear, observation distance, defect depth, load intensity) for a single defect, in order to give an estimation of the total uncertainty, thus of the total error that an operator could commit without using the optimization procedure developed in this work. Considering a defect of 25 mm diameter, results are shown in Fig. 6.7. The combination of all results gives a mean value of 25.8 $\pm$ 2.2 mm.

6.3 Evaluation of the influence of measurement parameters on uncertainty and accuracy for real case studies

In this Section the focus is put on comparing standard use of Shearography and optimization procedure for the real case studies examined in Chapter 5, in order to highlight the advantages of the studied procedure for more complex inspections. Since the mentioned case studies were supposed to be used as validation, not all the parameter combinations were tested. In particular, shear was the varying

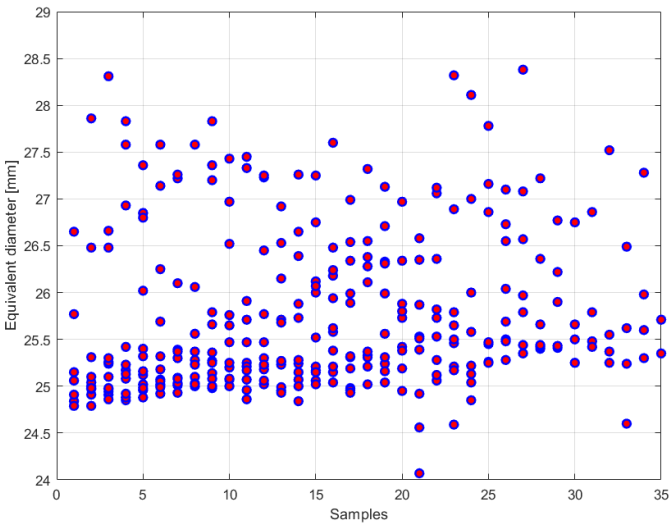

Figure 6.7: Data distribution for a 25 mm defect considering all the possible paramter variations.

parameter (necessary condition for building the parabola), while the observation distance was set to 24 cm in order to benefit from higher spatial resolution.

6.3.1 Sandwich 1 (honeycomb core and carbon fiber skin)

Data discussed in Sec. 5.1 are analyzed from the point of view of accuracy and uncertainty, as done in the previous Section for the PVC test panel. Fig. 6.8 shows the distribution of data for different shear values, for a fixed observation distance of 24 cm. The depth of the defect is unknown. Without applying the developed procedure, data would provide a resulting mean value of 17.70 mm with a standard deviation of $\pm$ 2.00 mm, while the optimization process gives a diameter of 15.30 mm with a standard deviation of $\pm$ 0.02 mm, given by the algorithm performances. The latter result is much closer to the one obtained by the Ultrasound inspection discussed in Sec. 5.1, see Tab. 6.8. Since Ultrasound inspection is exploited just as comparative measurement and not as reference measurement, the definition of an accuracy percentage is not appropriate. Nevertheless, after the optimization process, a closer agreement with Ultrasound inspection results can be registered in addition to an uncertainty reduction of 99 %.

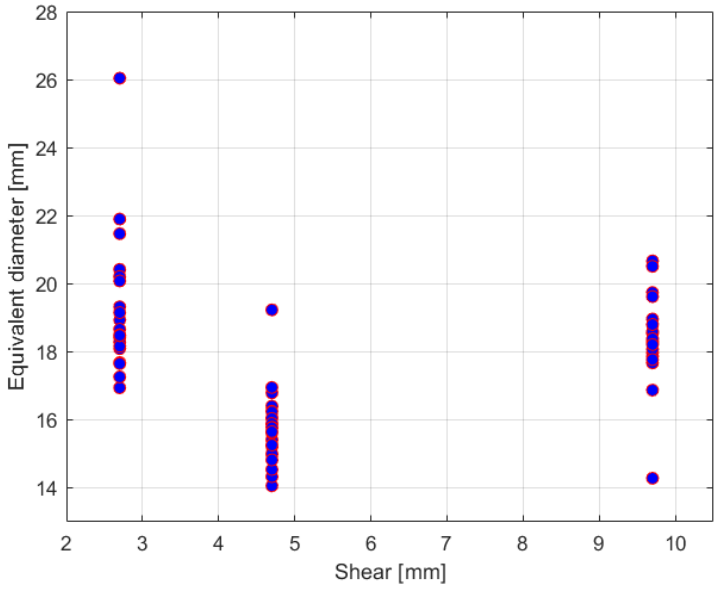

Figure 6.8: Data distribution for different shear amounts for Sandwich 1.

Table 6.8: Uncertainty results for Sandwich 1.

	Standard use	**Developed procedure**	**Ultrasound inspection**
Resulting diameter [mm]	17.70	15.30	15
Uncertainty [mm]	± 2.10	± 0.02	± 2

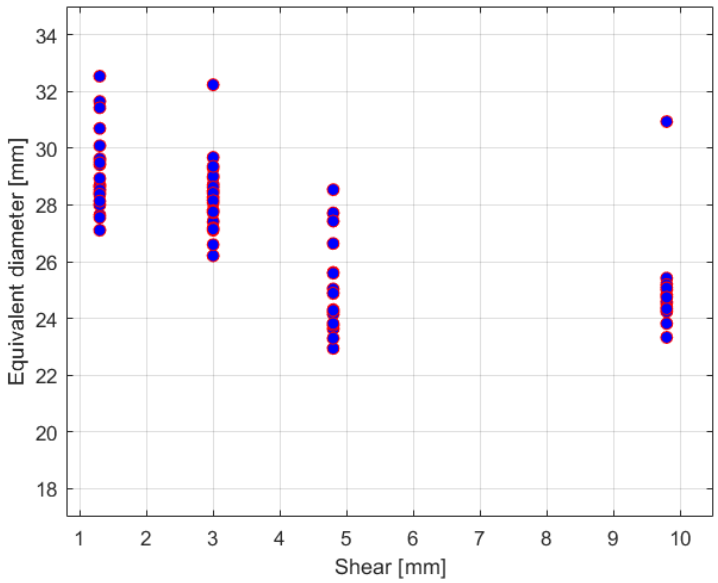

Figure 6.9: Data distribution for different shear amounts for Sandwich 2.

Table 6.9: Uncertainty results for Sandwich 2.

	Standard use	**Developed procedure**	**Ultrasound inspection**
Resulting diameter [mm]	27.50	28.60	28
Uncertainty [mm]	± 4.50	± 0.02	± 2

6.3.2 Sandwich 2 (honeycomb core and fiberglass skin)

In this Section data discussed in Sec. 5.2 are analyzed from the point of view of accuracy and uncertainty. Fig. 6.9 shows the distribution of data for different shear values, for a fixed observation distance of 24 cm. Without applying the developed procedure, data would provide a resulting mean value of 27.50 mm with a standard deviation of ± 4.50 mm, while the optimization process gives a diameter of 15.30 mm with a standard deviation of ± 0.02 mm, given by the algorithm performances. The latter result is much closer to the one obtained by the Ultrasound inspection discussed in Sec. 5.2, see Tab. 6.9. Similarly Sandwich 1, an uncertainty reduction of 99.5 % is detected by the use of the developed procedure with respect to a standard use of the technique.

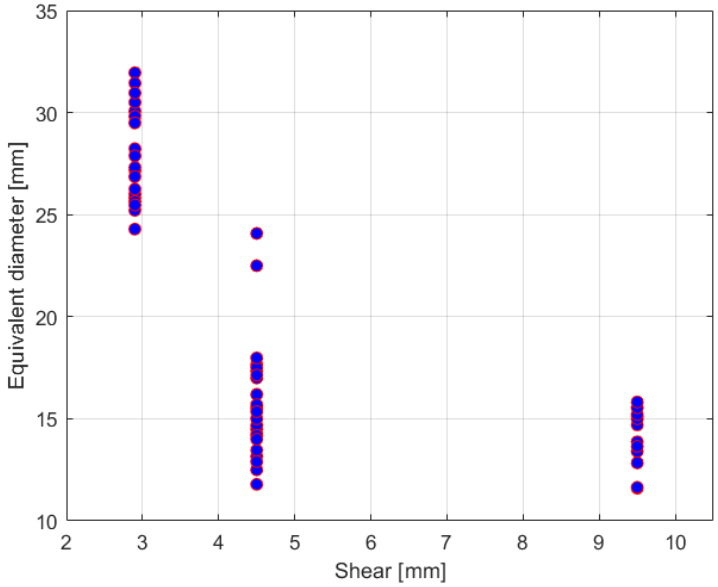

Figure 6.10: Data distribution for different shear amounts for the Carbon thin plate.

Table 6.10: Uncertainty results for the Carbon thin plate.

	Standard use	**Developed procedure**	**Ultrasound inspection**
Resulting diameter [mm]	18.90	14.80	13
Uncertainty [mm]	± 6.20	± 0.02	± 2

6.3.3 Carbon thin plate

In this Section data discussed in Sec. 5.3 are analyzed from the point of view of accuracy and uncertainty. Fig. 6.10 shows the distribution of data for different shear values, for a fixed observation distance of 24 cm. Without applying the developed procedure, data would provide a resulting mean value of 18.90 mm with a standard deviation of ± 6.20 mm, while the optimization process gives a diameter of 14.80 mm with a standard deviation of ± 0.02 mm, given by the algorithm performances. The latter result is much closer to the one obtained by the Ultrasound inspection discussed in Sec. 6.10, see Tab. 6.10. Considering data in Tab. 6.10, an uncertainty reduction of 99.9 % is detected by the use of the developed procedure with respect to a standard use of the technique.

6.3.4 Final discussion about uncertainty and accuracy detected for the examined, real case studies

In this Section all results obtained from the composites panel examined are summarized in order to make considerations about the advantages associated with the exploitation of the optimization procedure developed in this work. As already mentioned, the resolution available for the used Ultrasound system did not allow its use as reference measurement, but just as comparative inspection. Therefore, instead of computing the accuracy percentage, it is possible to compute the agreement percentage of Shearography results with Ultrasound inspection. Results are shown in Tab. 6.11. Here it can be noticed that the advantages of the procedure both in terms of standard deviation and of agreement with another Non Destructive Technique are even more evident for the most complex case, i.e. the carbon thin plate. In fact, as discussed in Sec. 5.1, this case corresponds to the lowest Signal-to-Noise ratio due to the component's stiffness that makes the defect deformation closer to the global deformation of the panel with respect to sandwich ones. Therefore, the exploitation of the developed optimization process appears significantly suitable to counter the increase of data dispersion and the worsening accuracy in case of low SNRs.

Table 6.11: Accuracy and standard deviation improvement between standard use and developed procedure for real case studies.

		Standard use	Developed procedure
Case study: Sandwich 1	**Agreement with ultrasound inspection** [%]	82	98
	Uncertainty [mm]	± 2.10	± 0.02
	Uncertainty reduction [%]	99	
		Standard use	**Developed procedure**
Case study: Sandwich 2	**Agreement with ultrasound inspection** [%]	98	98
	Uncertainty [mm]	± 4.50	± 0.02
	Uncertainty reduction [%]	99.5	
		Standard use	**Developed procedure**
Case study: Carbon thin plate	**Agreement with ultrasound inspection** [%]	54	86
	Uncertainty [mm]	± 6.20	± 0.02
	Uncertainty reduction [%]	99.9	

Chapter 7

Conclusions

The aim of my Ph.D. activities has been focused on designing, developing and validating a standardized and quantitative measurement procedure for Shearography inspections involving thermal load applications. The importance of this work lies in the fact that, up to now, Shearography has been used as a qualitative technique, i.e. only for checking the presence of possible defects within the inspected structure, without paying attention about quantitative defect size estimation and morphological reconstruction. In fact, Shearography is a highly sensitive non-destructive interferometric technique, working in the sub-micrometer range for detecting defects exploiting the difference of deformation between the defect itself and the rest of the structure.
The reasons of the qualitative use of Shearography are, mainly: the lack of standard procedures to perform in case of thermal load applications, the lack of algorithms for defect size computation and morphological reconstruction from Shearography phase-maps, and the variability of inspection results with respect to the measurement parameters themselves (shear, distance of observation, load, defect size and depth). The procedure has been developed by using a PVC test panel, and validated on real case studies involving different composite materials affected by different defects. The fixed objective was achieved by developing both new hardware and software.

With regard to the new hardware developed, a computerized measurement setup was designed and prototyped. In particular, it is provided with: the Shearocamera, its own controller and Personal Computer, two heating lamps and a proper structure supposed to house two shutters for screening the lamps after their switching-off.

These shutters avoid thermal radiation coming from the lamps (even if already switched-off) to keep heating the structure and avoid also air turbulence due to the residual radiation itself, thus reducing the uncertainty sources upstream. Lamps and shutters are controlled by two HID relays communicating with the Shearography Personal Computer. In order to make the procedure repeatable from the acquisition phase, all these setup elements were synchronized by using a Virtual User, developed in Labview environment and installed in the Shearography Personal Computer. This Virtual User is programmed for performing the following series of actions: heating the structure for a fixed time interval (activating lamps relay), switching-off the heating lamps and, in the same time instant, screening them by releasing the shutters (previously kept in position by two electromagnets controlled by the second HID relay), starting Shearography acquisition and storing phase-maps for a given time interval with a fixed frame rate. The Virtual User is able to realize this sequence by recognizing and pushing pre-defined buttons within the desktop, thanks to a proper Pattern Matching algorithm. The implementation of such Virtual User was necessary since only the more recent systems are provided with triggering and rating options, because of the typical qualitative use does not need such additional tools. However, they are crucial for guaranteeing quantitative measurements and repeatability. Unfortunately, available software upgrades for older systems are considerably expensive, and compatibility errors with older hardware may occur. The Virtual User developed during my Ph.D. activities overcomes these problems since it is compatible with any device and operating system, at no cost.

On the other hand, with regard to the new software developed, my work focused on the implementation of a tool able both to process resulting phase-maps for extracting quantitative information about the component deformation evolution, and to perform defect size computation and morphological reconstruction. Both these goals required the following processing steps: distortion correction, phase computation, phas-maps filtering, phase-map unwrapping and unwrapping-error correction, shear computation. Moreover, the algorithm used for defect characterization is based on a Wavelet Transform approach for singularities estimation, since defect boundaries can be considered as singular points within the entire phase-map. Because of noise, other secondary singularities are superimposed to the dominant ones so that, in order to select the latter and discard the others, a

specific parameter, called Structural Intensity is exploited.

Once provided the new hardware and software tools, my work focused on studying the mentioned measurement procedure for Shearography inspection. The very first step of the procedure is performed before activating the Shearography hardware, and involves the definition of measurement ranges, in particular the maximum and minimum heating time for the inspected material. While the minimum heating time is given by the system's rapidity, the maximum heating time is computed by imposing a step excitation to the structure and evaluating the time constant τ on the component's back-side. From this datum, it is possible to retrieve the time delay after which the thermal wave reaches a certain fixed depth from the observed surface. This delay corresponds to the maximum heating time to impose, since in this condition the deformation of the entire structure becomes more comparable with respect to the defect deformation, generating a decrease of the Signal to Noise Ratio and consequently, of the reliability of results. After doing this, Shearography hardware can be activated for the definition of the shear range. In this regard, both the upper and the lower limits are given by the shearing and phase-shifting mirrors lying inside the Shearocamera. Therefore, the operator has to manually set the minimum and the maximum shear he is able to impose and to store the respective speckle images. After that, the two shear values can be extracted by encoding the data provided by the acquisition software. In fact, another part of this work dealt with encoding hierarchical data coming from the device in order to retrieve both the shear vector information associated to each image, and the four speckle images that the devices exploits, during acquisition, for computing the phase-maps. Having the possibility of accessing raw data has been an important goal during my activities, since it enabled to limit errors generated by data conversions and to implement algorithms that would not have been possible otherwise. The third step of the procedure is focused on defining the measurement ranges in terms of deformation, by the assumption that the shearing amount influences both the resolution and the sensitivity of the system. This is useful since, in a real application, one could have a specific requirement about the minimum displacement gradient to resolve, that is dependent on the shear itself. Therefore, it is possible to compute the shear needed to resolve such a deformation. However, it is highly probable that the phase change generated by this shear value, that is the minimum acceptable one, is not sufficient to provide a good Signal-to-Noise

Ratio. In fact, this shear does not generate a phase variation higher than 2π, thus no fringe is detected. It is needed to evaluate, for the given shear, the deformation range within which fringes can be detected, in order to have higher SNRs. This procedure phase, at the end, is aimed at defining, in the deformation-shear domain, three different areas: the out-of-measurement range area, the area where it is possible to resolve deformation changes but no fringe is detected, and the fringe detection area, where the upper limit is set to 10 fringes due to limitations given by spatial resolution. This first group of steps can be categorized as *preliminary operations* and can be carried out even if no defect is detected. On the contrary, if a defect-generated fringe pattern is detected, a second group of actions is defined to complete the entire measurement procedure. This is necessary because of the variability of the defect size estimation with respect to measurement parameters. Therefore, the main idea has been to create different data-collections corresponding to different combinations of load, observation distance, shear and defects. More precisely, by fixing a certain defect and observation distance, results obtained from at least three different shear values should be examined. For each shear value, a series of load cycles of increasing intensity (within the range determined during preliminary operations) has to be imposed to the structure, and results have to be processed in order to choose, as right observation, the first data-collection where the relationship between computed defect size and deformation is not random, but it is characterized by an accumulation point. Therefore, a unique load cycle is considered suitable for reaching a confident inspection at given shear, so that a unique result per shear value is finally obtained. At the end, by matching the resulting defect sizes and the corresponding shear, a parabolic distribution is always observed. The vertex of this parabola represents the optimal condition, in terms of shear, and the best defect-size estimation achievable for that specific defect, observed from that specific distance. Therefore, it is possible to repeat the same procedure on the same material affected by different defects, changing also observation distance. In this way, a model can be obtained estimating the optimal combinations of measurement parameters. This requires the possession of a test panel of the same material as the one of the structure to inspect, in order to draw up a data-set of optimal parameters combination to use for different defect size and depths. Alternatively, in order to avoid errors due to differences between the test panel and the structure to inspect, it is possible to carry out the developed

procedure on the real structure for the currently detected defect.

At the end, validations were performed by considering three different case studies: a sandwich panel composed by a honeycomb core and a carbon fiber skin, where teflon inserts were put between sub-superficial layers, a sandwich panel composed by a honeycomb core a fiberglass skin , where a sub superficial delamination is present, and a carbon thin plate affected by teflon inserts. Results obtained by these case studies were compared to those obtained by air-coupled ultrasonic inspections performed on the same panels. It is worth to precise that such Ultrasound inspection is not used as reference measurement - since its accuracy is not higher than 10 times Shearography accuracy - but just as a comparative measurement. As a result, a good correspondence was obtained between Shearography and Ultrasound scanning for the two sandwich panels, even if the corresponding defects were either superimposed to the honeycomb cells deformation, or characterized by a complex shape affected by dynamical evolution. In addition, also the carbon thin plate inspection performed by Shearography showed a good match with respect to Ultrasound inspection. This was achieved despite the component's stiffness, that causes low contrast between defect and background, worsening the detection. The out-of-plane displacement gradient difference between defect and entire structure, in fact, was demonstrated to be at the limit of resolution.

In conclusion, a comparison between a standard use of Shearography and the optimization procedure developed in this work was performed. This investigation gave an improvement of accuracy and uncertainty between 70 % and 99 % according to the parameter responsible of affecting results (shear, observation distance, defect depth and size, load intensity). In fact, the lowest increase of performances achieved by the use of the developed procedure is recorded when the varying parameter is observation distance, due to the loss of resolution that jeopardizes data a priori.

The comparison between standard use and optimization procedure was carried out even for the composite panels used as real case studies for validation. In all these cases an uncertainty reduction around 99 % was achieved by the use of the optimization procedure with respect to standard use. Nevertheless, it is worth to put the attention on the agreement as percentage with Ultrasound inspection. In particular, the highest improvement of such agreement achieved by the use of the procedure corresponds to the case of the carbon thin plate, having the lowest SNR. Therefore, it can be concluded that the positive effect of this work is even more

evident for more complex cases, where the deformation of the defect is slightly different from the global deformation.

The further optimization in terms of computational expense of the implemented software could be carried out as future activities as well as the engineering of the entire system in order to enable implementation in commercial field.

Appendix A

Additional activities

During my Ph.D. Course, in conjunction with the main research project presented in this thesis, other additional activities were carried out in the field of Non Destructive Testing of aerospace components and materials. In particular, a feasibility study about the possibility of using Thermoelastic Stress Analysis (TSA) for the inspection of Additively Manufactured Satellite Bracket made in titanium-based alloys was conducted. This activity was also published in Measurement Journal, see [70]. Metal brackets made in titanium based-alloys are one of the most diffused case studies in the field of Additive Manufacturing (AM) technologies: the current generation of satellites relies on metal brackets to serve as a link between the body of the satellite and the reflectors and feeder facilities mounted at its upper end. In this scenario, one of the main focal points is the qualification of the 3D printed-products, including both the characterization of the micro/macro-structure of the component, and the definition of its mechanical behavior. Despite the high presence, in literature, of works dealing with the detection of defects in the structure, no dissertation can be found about stress analysis on the actual component, and this is what this paper focuses on. This topic is crucial because some morphological or dimensional differences between the nominal (CAD) structure and the manufactured one could lead to non-predicted stress concentrations at the end. In literature, many industries and institutions (Airbus, NASA, Rolls-Royce, Oak Ridge National Laboratory, etc.) are involved in research projects dealing with AM Technologies implemented on aerospace components, especially on titanium alloy made-brackets. Generally, this kind of products requires design optimization

processes searching for a component geometry that satisfies all structural and manufacturing constraints while maximizing the objectives associated with the application. Minimal mass and minimal costs objectives are associated with stiffness, strength and allowable volume constraints. From the study of the state of the art, it emerged that no work has been done up to now about performing stress analysis on the actual component, in order to compare the experimental results with the expected, nominal, mechanical behavior: this is what this activity focuses on. In fact, dimensional, roughness-generated, structural deviations between the nominal and the manufactured component could even lead to discrepancies in the stress distributions across the component. This methodology could act as a support for dimensional inspection in order to define the amount and the kind of deviations between the nominal and the actual component, making available a more complete inspection.

The Thermoelastic effect is based on the fact that the temperature of a substance can only be raised by working up on it in some way so as to produce increased thermal motions within it, and from this effect the mutual distances or arrangement of its particles which may accompany a change of temperature. The work necessary to produce this total mechanical effect is proportional to the quantity of the substance raised from one standard temperature to another. Therefore when a substance loses or receives heat, a mechanical effect is produced, which is proportional to the heat which it emits or absorbs. Therefore, a temperature change ΔT is strictly related to the variation of the first stress invariant $\Delta\sigma$: in this way, by observing a loaded component through a thermal camera, it is possible to store its stress distribution. However, the temperature changes generated by the most commonly used engineering materials are very little and rapidly disappear because of heat transfer. It is therefore necessary to dynamically load the component at proper frequency. In the following, the different steps of the methodology developed for the stress characterisation of a satellite bracket made by Electron Beam Melting (EBM) are presented.

Reverse Engineering using a triangulation system For the 3D reconstruction of our component, we used a GOM ATOS Core 185 Optical Measurement System with the following characteristics:

- Measurement area: 185×140 mm;

Figure A.1: Reconstructed geometry by means of the triangulation system.

- Observing distance: 440 mm;
- Points distance: 0.07 mm;
- Sensor dimensions: $361 \times 205 \times 64$ mm;
- Probing error form : 0.001 mm;
- Sphere spacing error: 0.002 mm.

For evaluating dimensional deviations between the reconstructed geometry and the nominal one, a best-fit alignment between the two parts was used.

Equipment of a test bench for TSA In Fig. A.2 the measurement chain designed for the determination of the stress distribution by thermoelastic effect is shown. The adiabatic conditions, necessary for a reliable measurement, are obtained by periodically loading the component by an electrodynamical shaker, regulated by a PID controller. Hence, the shaker produces a sine wave characterized by the imposed load (peak-to-peak) and frequency, and the feedback sensor is represented by a load cell. Now, due to the fact that the thermal cameras used for TSA have a Noise Equivalent Differential Temperature (NEDT) of the order of 10 mK (we used a FLIR Cedip Titanium Series SC700 thermal camera, having a NEDT < 18 mK), while the temperature changes related to thermoelastic effect are of the order of 1 mK, a particular arrangement to overcome the problem is necessary. Hence, a Lock-In Amplifier technique is generally implemented: the thermal camera receives

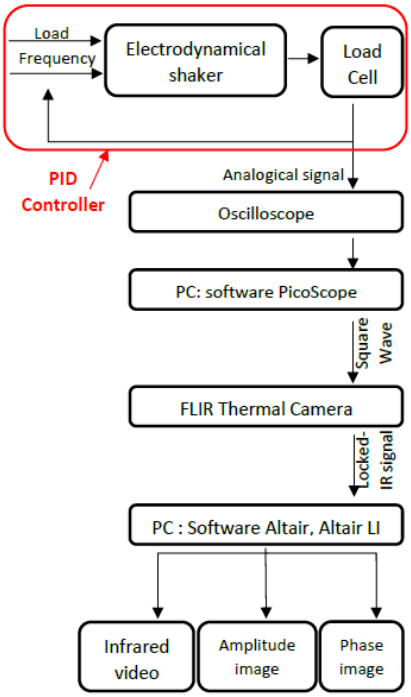

Figure A.2: Measurement chain.

a periodical signal having the load frequency as input, and multiplies the Infrared signal with the input one, in order to remove all the noise that is stored at the other frequencies. At the end, the output is a thermal film whose complex analysis gives back an amplitude image and a phase one, representing respectively the stress distribution across the pixel array and the stress sign (compression or traction).

Comparison between experimental and FEM results In order to define possible deviations between the expected and the actual mechanical behavior, a comparison between TSA and two kinds of FEM results was performed: the first one is evaluated on the CAD model, while the second one is evaluated on the reconstructed geometry using the mentioned Reverse Engineering system. This further comparison is suitable for a better understanding of the reasons of the identified discrepancies in the stress trends.

Results The dimensional comparison between the Reverse Engineering- reconstructed model and the CAD one, evaluated by the GOM Correlate software, shows

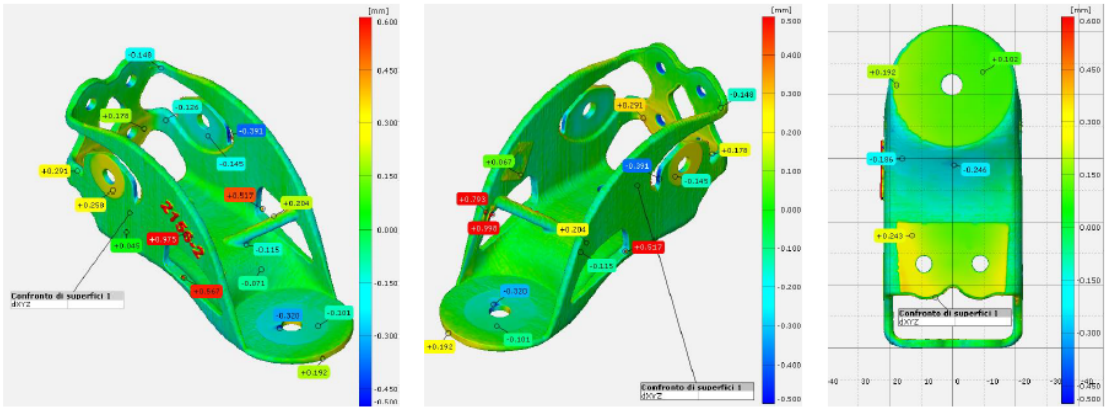

Figure A.3: Evaluation of dimensional deviations by GOM Correlate software

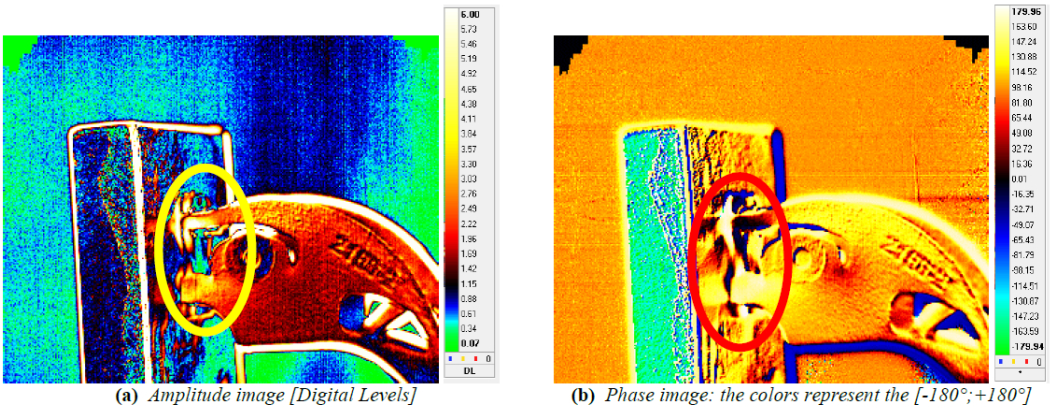

(a) *Amplitude image [Digital Levels]*

(b) *Phase image: the colors represent the [-180°;+180°] range*

Figure A.4: TSA results revealing the location and the sign of the stress concentrations.

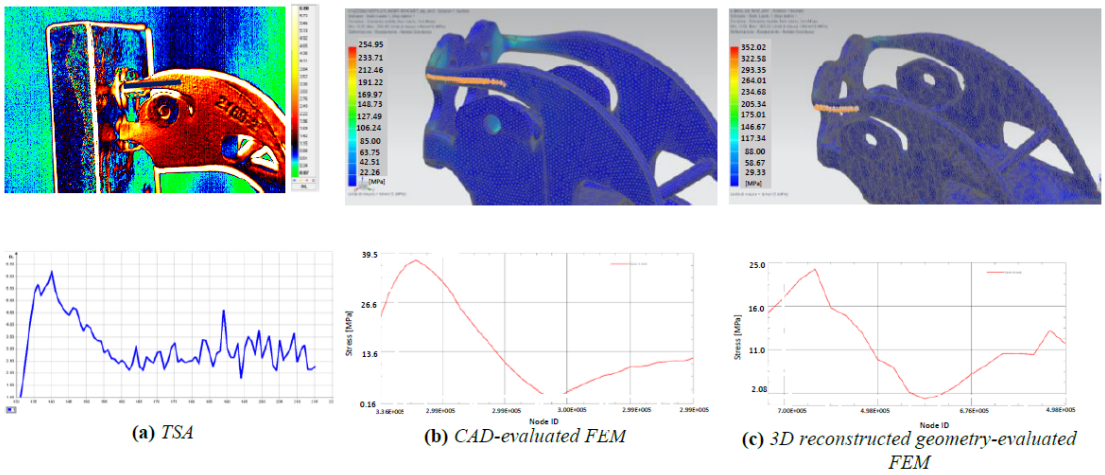

Figure A.5: Comparison between experimental results and theoretical ones.

a maximum deviation of the order of 0.3 mm, excepting for some higher deviations due to printed codes, an installed extensimeter, etc., see Fig. A.3. According to the image to the left in Fig. A.4, the stress localization is in accordance with the predicted one, confirming the feasibility of such a kind of investigation for the examined component. On the other side, the image on the right shows another result in accordance with the physics of the problem: the upper and the lower curvatures work oppositely in terms of stress: when the ones are stretched, the others are compressed and vice-versa. This can be deduced by the opposition of color levels, as the color level is associated to phase values between $-180°$ and $180°$. Moreover, in Fig. A.5 the comparison between experimental and theoretical results is reported. Significant interrogation lines were extracted in order to gain more sensitivity about the stress trends. It is worth to precise that this comparison is qualitative, as a comparison based on the effective stress values would have been possible only after a proper calibration process. Therefore, it is remarkable that the stress trend relative to the FEM analysis conducted on the CAD model (Fig. A.5(b)) is much smoother than the trends in the actual component. This is clear both in the theoretical results extracted from the FEM analysis evaluated on the 3D reconstructed geometry (Fig. A.5 (c)), and in the TSA results (Fig. A.5 (a)). However, it generally happens the opposite: the thermoelastic trends are the smoother ones, as a small amount of heat exchange always occurs, providing a small loss of resolution. Hence, the trends obtained in our test campaign, reveal

that the particular micro/macro structure and the surface roughness provided by the Additive Manufacturing process, lead to localized stress peaks, not predictable a-priori.

Conclusions A feasibility study about the possibility of applying Thermoelastic Stress Analysis (TSA) on an additively manufactured aerospace bracket made in a titanium based-alloy was carried out. The developed measurement technique, in conjunction with proper morphological and dimensional investigation tools, could make available a more complete Non- Destructive qualification process for AM made aerospace brackets (which represent one of the most diffused case studies), giving information about the effective mechanical behavior of the structure.

Bibliography

[1] N. V. Nayak. "Composite Materials in Aerospace Applications ". In: *International Journal of Scientific and Research Publications* 14.9 (2014). ISSN: 2250-3153.

[2] S. Rana and R. Fangueiro. "Advanced composites in aerospace engineering". In: *Advanced Composite Materials for Aerospace Engineering*. Ed. by Sohel Rana and Raul Fangueiro. Woodhead Publishing, 2016, pp. 1–15. ISBN: 978-0-08-100939-0. DOI: https://doi.org/10.1016/B978-0-08-100037-3.00001-8. URL: http://www.sciencedirect.com/science/article/pii/B9780081000373000018.

[3] Z. Fawaz. "Quality control and testing methods for advanced composite materials in aerospace engineering". In: *Advanced Composite Materials for Aerospace Engineering*. Ed. by Sohel Rana and Raul Fangueiro. Woodhead Publishing, 2016, pp. 429–451. ISBN: 978-0-08-100939-0. DOI: https://doi.org/10.1016/B978-0-08-100037-3.00015-8. URL: http://www.sciencedirect.com/science/article/pii/B9780081000373000158.

[4] L. Z. Linganiso and R. D. Anandjiwala. "Fibre-reinforced laminates in aerospace engineering". In: *Advanced Composite Materials for Aerospace Engineering*. Ed. by Sohel Rana and Raul Fangueiro. Woodhead Publishing, 2016, pp. 101–127. ISBN: 978-0-08-100939-0. DOI: https://doi.org/10.1016/B978-0-08-100037-3.00004-3. URL: http://www.sciencedirect.com/science/article/pii/B9780081000373000043.

[5] J. P. Nunes and J. F. Silva. "Sandwiched composites in aerospace engineering". In: *Advanced Composite Materials for Aerospace Engineering*. Ed. by Sohel Rana and Raul Fangueiro. Woodhead Publishing, 2016, pp. 129–174. ISBN: 978-0-08-100939-0. DOI: https://doi.org/10.1016/B978-0-08-100037-

3.00005-5. URL: http://www.sciencedirect.com/science/article/pii/B9780081000373000055.

[6] B. Frieden. "Laser speckle and related phenomena". In: *IEEE Journal of Quantum Electronics* 20.12 (Dec. 1984), pp. 1533–1533. ISSN: 0018-9197. DOI: 10.1109/JQE.1984.1072321.

[7] W. Steinchen and L. Yang. *Digital Shearography: Theory and Application of Digital Speckle Pattern Shearing Interferometry*. Press Monograph Series. SPIE Press, 2003. ISBN: 9780819441102. URL: https://books.google.it/books?id=qDSYT0GnM20C.

[8] K. n Exner. " Über die Fraunhofer'schen Ringe, die Quetelet'schen Streifen und verwandte Erscheinunge". In: *Sitzungsber. Akad. Wiss. Wien* 76 (1877), pp. 522–550.

[9] C. V. Raman. *Lectures on Physical Optics*. Ed. by Indian Academy of Sciences. Lectures on Physical Optics pt. 1. Indian Academy of Sciences, 1959. URL: https://books.google.it/books?id=5-A9AQAAIAAJ.

[10] P. Hariharan. "Speckle Patterns: A Historical Retrospect". In: *Optica Acta: International Journal of Optics* 19.9 (1972), pp. 791–793. DOI: 10.1080/713818646. eprint: https://doi.org/10.1080/713818646. URL: https://doi.org/10.1080/713818646.

[11] M. Crompton T. R. Tamberg. "Laser Shearography of Aerospace Composites". In: *The NDT Technician* 10.3 (2011), pp. 1–4.

[12] N. Soltani D. Akbari. "Investigation of Loading Parameters in Detection of Internal Cracks of Composite Material with Digital Shearography". In: *World Applied Sciences Journal* 21.4 (2013), pp. 526–535. ISSN: 1818-4952.

[13] Bing Pan et al. "Two-dimensional digital image correlation for in-plane displacement and strain measurement: a review". In: *Measurement Science and Technology* 20.6 (Apr. 2009), p. 062001. DOI: 10.1088/0957-0233/20/6/062001. URL: https://doi.org/10.1088%2F0957-0233%2F20%2F6%2F062001.

[14] R. Di Sante et al. “Reliability and Accuracy of Embedded Fiber Bragg Grating Sensors for Strain Monitoring in Advanced Composite Structures”. In: *Metals and Materials International* 20 (May 2014), pp. 537–543. DOI: 10.1007/s12540-014-3020-7.

[15] Filip Zastavnik et al. “Calibration and correction procedure for quantitative out-of-plane shearography”. In: *Measurement Science and Technology* 26.4 (Feb. 2015), p. 045201. DOI: 10.1088/0957-0233/26/4/045201. URL: https://doi.org/10.1088%2F0957-0233%2F26%2F4%2F045201.

[16] Y. Y. Hung. “Digital shearography versus TV-holography for non-destructive evaluation”. In: *Optics and Lasers in Engineering* 26.4 (1997). Speckle and Speckle Shearing Interferometry-II, pp. 421–436. ISSN: 0143-8166. DOI: https://doi.org/10.1016/0143-8166(95)00141-7. URL: http://www.sciencedirect.com/science/article/pii/0143816695001417.

[17] D. Francis, R. Tatam, and R. Groves. “Shearography Technology and Applications: A Review”. In: *Measurement Science and Technology* 21 (Aug. 2010). DOI: 10.1088/0957-0233/21/10/102001.

[18] Y. Y. Hung and A. J. Durelli. “Simultaneous measurement of three displacement derivatives using a multiple image-shearing interferometric camera”. In: *The Journal of Strain Analysis for Engineering Design* 14.3 (1979), pp. 81–88. DOI: 10.1243/03093247V143081. eprint: https://doi.org/10.1243/03093247V143081. URL: https://doi.org/10.1243/03093247V143081.

[19] B. Bhaduri et al. “Use of spatial phase shifting technique in digital speckle pattern interferometry (DSPI) and digital shearography (DS)”. In: *Opt. Express* 14.24 (Nov. 2006), pp. 11598–11607. DOI: 10.1364/OE.14.011598. URL: http://www.opticsexpress.org/abstract.cfm?URI=oe-14-24-11598.

[20] G. T. Shrivakshan and C. Chandrasekar. “A Comparison of various Edge Detection Techniques used in Image Processing”. In: *International Journal of Computer Science Issues* 9 (Sept. 2012), pp. 269–276.

[21] Hubert A. Aebischer and Stephan Waldner. “A simple and effective method for filtering speckle-interferometric phase fringe patterns”. In: *Optics Communications* 162.4 (1999), pp. 205–210. ISSN: 0030-4018. DOI: https://doi.

org/10.1016/S0030-4018(99)00116-9. URL: http://www.sciencedirect.com/science/article/pii/S0030401899001169.

[22] T. Lindeberg. *Scale-space: A framework for handling image structures at multiple scales*. 1996.

[23] Firas Sawaf and Ralph Tatam. "Finding minimum spanning trees more efficiently for tile-based phase unwrapping". In: *Measurement Science and Technology* 17 (May 2006), p. 1428. DOI: 10.1088/0957-0233/17/6/022.

[24] C. Zuo et al. "Temporal phase unwrapping algorithms for fringe projection profilometry: A comparative review". In: *Optics and Lasers in Engineering* 85 (2016), pp. 84–103. ISSN: 0143-8166.

[25] Michael Esseling. "Electric Fields and Their Detection in Photorefractive Crystals". In: *Photorefractive Optoelectronic Tweezers and Their Applications*. Ed. by Springer. Cham: Springer International Publishing, 2015. Chap. 1, pp. 15–40. ISBN: 978-3-319-09318-5. DOI: 10.1007/978-3-319-09318-5_3. URL: https://doi.org/10.1007/978-3-319-09318-5_3.

[26] D. C. Ghiglia and M. D. Pritt. *Two-dimensional phase unwrapping: theory, algorithms, and software*. Wiley-Interscience publication. Wiley, 1998. ISBN: 9780471249351. URL: https://books.google.it/books?id=pQtTAAAAMAAJ.

[27] Munther Gdeisat and Francis Lilley. *One-Dimensional Phase Unwrapping Problem*. 2011. URL: https://www.ljmu.ac.uk/~/media/files/ljmu/about%E2%80%91us/faculties%E2%80%91and%E2%80%91schools/tae/geri/two_dimensional_phase_unwrapping_finalpdf.pdf?la=en.

[28] S. Liu and L. X. Yang. "Regional phase unwrapping method based on fringe estimation and phase map segmentation". In: *Optical Engineering* 46.5 (2007), pp. 1–9. DOI: 10.1117/1.2741232. URL: https://doi.org/10.1117/1.2741232.

[29] Sikun Li, Wenjing Chen, and Xianyu Su. "Reliability-guided phase unwrapping in wavelet-transform profilometry". In: *Appl. Opt.* 47.18 (June 2008), pp. 3369–3377. DOI: 10.1364/AO.47.003369. URL: http://ao.osa.org/abstract.cfm?URI=ao-47-18-3369.

[30] W. Steinchen et al. "Strain analysis by means of digital shearography: Potential, limitations and demonstration". In: *The Journal of Strain Analysis for Engineering Design* 33.2 (1998), pp. 171–182. DOI: 10.1243/0309324981512896. eprint: https://doi.org/10.1243/0309324981512896. URL: https://doi.org/10.1243/0309324981512896.

[31] Thorsten Siebert, Karsten Splitthof, and Andreas Ettemeyer. "A Practical Approach to the Problem of the Absolute Phase in Speckle Interferometry". In: *Journal of Holography and Speckle* 1 (Mar. 2004), pp. 32–38. DOI: 10.1166/jhs.2004.005.

[32] R. Kastle, E. Hack, and U. Sennhauser. "Multiwavelength shearography for quantitative measurements of two-dimensional strain distributions." eng. In: *Applied optics* 38 (1 Jan. 1999), pp. 96–100.

[33] A. G. Anisimov and R. M. Groves. *3D shape shearography with integrated structured light projection for strain inspection of curved objects*. 2015. DOI: 10.1117/12.2184058. URL: https://doi.org/10.1117/12.2184058.

[34] Dênis T. Goto and Roger Groves. "A combined experiment with simulation approach to calibrated 3D strain measurement using shearography". In: *Proceedings of SPIE - The International Society for Optical Engineering* 7387 (Sept. 2010). DOI: 10.1117/12.870572.

[35] Fu Yang et al. "The effect of loading methods and parameters on defect detection in digital shearography". In: *Results in Physics* 7 (2017), pp. 3744–3755. ISSN: 2211-3797. DOI: https://doi.org/10.1016/j.rinp.2017.09.015. URL: http://www.sciencedirect.com/science/article/pii/S2211379717309245.

[36] URL: https://www.dantecdynamics.com/shearography-non-destructive-testing.

[37] URL: https://optotechnik.zeiss.com/en/67-en/produkte/shearografie-ndt.

[38] URL: http://www.isi-sys.com/shearography-systems/.

[39] Martin Kadlec and Roman Ruzek. "A Comparison of Laser Shearography and C-Scan for Assessing a Glass/Epoxy Laminate Impact Damage". In: *Applied Composite Materials - APPL COMPOS MATER* 19 (June 2011), pp. 1–15. DOI: 10.1007/s10443-011-9211-1.

[40] Dantec Dynamics. *Application Note – T-Q-800-Sandwich-CSM-002-EN.*

[41] R. M. Groves E. C. Krutul. "Opto-mechanical modelling and experimental approach to the measurement of aerospace materials using shearography and thermal loading". In: *Modeling Aspects in Optical Metrology III.* Vol. 80831C. SPIE. 2011.

[42] Davood Akbari, Naser Soltani, and Mohammadreza Farahani. "Numerical and experimental investigation of defect detection in polymer materials by means of digital shearography with thermal loading". In: *Proceedings of the Institution of Mechanical Engineers, Part B: Journal of Engineering Manufacture* 227.3 (2013), pp. 430–442. DOI: 10.1177/0954405412473054. eprint: https://doi.org/10.1177/0954405412473054. URL: https://doi.org/10.1177/0954405412473054.

[43] Daniel Hofmann et al. "Optimization of the excitation and measurement procedures in nondestructive testing using shearography." eng. In: *The Review of scientific instruments* 79 (11 Nov. 2008), p. 115105.

[44] Angelica Andersson et al. "TV shearography: quantitative measurement of shear-magnitude fields by use of digital speckle photography". In: *Applied Optics* 39.16 (June 2000), pp. 2565–2568. DOI: 10.1364/AO.39.002565. URL: http://ao.osa.org/abstract.cfm?URI=ao-39-16-2565.

[45] T. W. Ng. "Shear measurement in digital speckle shearing interferometry using digital correlation". In: *Optics Communications* 115.3 (1995), pp. 241–244. ISSN: 0030-4018. DOI: https://doi.org/10.1016/0030-4018(94)00702-V. URL: http://www.sciencedirect.com/science/article/pii/003040189400702V.

[46] Xin Xie et al. "Polarized digital shearography for simultaneous dual shearing directions measurements". In: *Review of Scientific Instruments* 87 (Aug. 2016). DOI: 10.1063/1.4961473.

[47] Fabrice Michel, Yvon Renotte, and Serge Habraken. "Measurement of the defect size by shearography or other interferometric techniques". In: *Optical Engineering* 51 (Mar. 2012). DOI: 10.1117/1.OE.51.3.033602.

[48] N. Sridevi P. Subashini. "An Optimal Binarization Algorithm Based on Particle Swarm Optimization". In: *International Journal of Soft Computing And Engineering (IJSCE)* 1.4 (2011), pp. 32–36.

[49] J. N. Kapur, P. K. Sahoo, and A. K. C. Wong. "A new method for gray-level picture thresholding using the entropy of the histogram". In: *Computer Vision, Graphics, and Image Processing* 29.3 (1985), pp. 273–285. ISSN: 0734-189X. DOI: https://doi.org/10.1016/0734-189X(85)90125-2. URL: http://www.sciencedirect.com/science/article/pii/0734189X85901252.

[50] M. S. Prasad, V. R. Krishna, and L. S. S. Reddy. "Investigation on Entropy based Threshold Methods". In: *Asian Journal of Computer Science and Information Technology* 1.5 (2013).

[51] J. Zhang and J. Hu. "Image Segmentation Based on 2D Otsu Method with Histogram Analysis". In: *2008 International Conference on Computer Science and Software Engineering*. Vol. 6. Dec. 2008, pp. 105–108. DOI: 10.1109/CSSE.2008.206.

[52] I.-P. Chen, Ming-Yi Lai, and Ling-Ling Wang. "An improvement in the moment-preserving thresholding method". In: *International Journal of Imaging Systems and Technology* 18 (Jan. 2008), pp. 365–370. DOI: 10.1002/ima.20169.

[53] Andrew Wee et al. "A continuous wavelet transform algorithm for peak detection". In: *ELECTROPHORESIS* 29.20 (2008), pp. 4215–4225. DOI: 10.1002/elps.200800096. eprint: https://onlinelibrary.wiley.com/doi/pdf/10.1002/elps.200800096. URL: https://onlinelibrary.wiley.com/doi/abs/10.1002/elps.200800096.

[54] Jérémie Bigot. "A scale-space approach with wavelets to singularity estimation". In: *http://dx.doi.org/10.1051/ps:2005007* 9 (Apr. 2005). DOI: 10.1051/ps:2005007.

[55] N. Fisher and J. S. Marron. "Mode testing via the excess mass estimate". In: *Biometrika* 88 (June 2001). DOI: 10.1093/biomet/88.2.499.

[56] Cristina Butucea, Mathilde Mougeot, and Karine Tribouley. "Functional approach for excess mass estimation in the density model". In: *Electronic Journal of Statistics* 1 (Nov. 2007). DOI: 10.1214/07-EJS079.

[57] *ASTM E2582-07, Standard Practice for Infrared Flash Thermography of Composite Panels and Repair Patches Used in Aerospace Applications*. ASTM International. West Conshohocken, PA, 2007.

[58] R. Groves et al. "Full-field Laser Shearography Instrumentation for the Detection and Characterization of Fatigue Cracks in Titanium 10-2-3". In: *Journal of Astm International* 3 (Jan. 2006). DOI: 10.1520/JAI12757.

[59] A. Trujillo-Ortiz et al. *Royston's Multivariate Normality Test*. Oct. 2007.

[60] Jurgen A. Doornik and Henrik Hansen. "An Omnibus Test for Univariate and Multivariate Normality". In: *University of Oxford, Open Access publications from University of Oxford* 70 (Dec. 2008). DOI: 10.1111/j.1468-0084.2008.00537.x.

[61] A. Trujillo-Ortiz, R. Hernandez-Walls, and K. Barba-Rojo. *Henze-Zirkler's Multivariate Normality Test*. Dec. 2007.

[62] G. M. Revel, G. Pandarese, and A. Cavuto. "Advanced ultrasonic non-destructive testing for damage detection on thick and curved composite elements for constructions". In: *Journal of Sandwich Structures and Materials* 15 (Jan. 2013), pp. 5–24. DOI: 10.1177/1099636212456861.

[63] A. Cavuto et al. "Experimental investigation by laser ultrasonics for high speed train axle diagnostics". In: *Ultrasonics* 55 (2015), pp. 48–57. ISSN: 0041-624X. DOI: https://doi.org/10.1016/j.ultras.2014.08.010. URL: http://www.sciencedirect.com/science/article/pii/S0041624X14002327.

[64] A. Cavuto et al. "Train wheel diagnostics by laser ultrasonics". In: *Measurement* 80 (2016), pp. 99–107. ISSN: 0263-2241. DOI: https://doi.org/10.1016/j.measurement.2015.11.014. URL: http://www.sciencedirect.com/science/article/pii/S0263224115006004.

[65] G. Revel, Alfonso Cavuto, and G. Pandarese. "Laser ultrasonics for bulk-density distribution measurement on green ceramic tiles". In: *Review of Scientific Instruments* 87 (Oct. 2016), p. 102504. DOI: 10.1063/1.4964626.

[66] Angelika Wronkowicz, Krzysztof Dragan, and Krzysztof Lis. "Assessment of uncertainty in damage evaluation by ultrasonic testing of composite structures". In: *Composite Structures* 203 (2018), pp. 71–84. ISSN: 0263-8223. DOI: https://doi.org/10.1016/j.compstruct.2018.06.109. URL: http://www.sciencedirect.com/science/article/pii/S0263822318311280.

[67] Angelika Wronkowicz-Katunin et al. "Uncertainty Estimation for Ultrasonic Inspection of Composite Aerial Structures". In: *Journal of Nondestructive Evaluation* 38.3 (Aug. 2019), p. 82. ISSN: 1573-4862. DOI: 10.1007/s10921-019-0622-5. URL: https://doi.org/10.1007/s10921-019-0622-5.

[68] P. Ciorau. *Comparison between -6 dB and -12 dB amplitude drop techniques for length sizing*. Ontario Power Generation. 2011. URL: http://www.ndt.net/.

[69] *Evaluation of measurement data — Guide to the expression of uncertainty in measurement*. JCGM 100:2008.

[70] Gloria Allevi et al. "Qualification of additively manufactured aerospace brackets: A comparison between thermoelastic stress analysis and theoretical results". In: *Measurement* 126 (2018), pp. 252–258. ISSN: 0263-2241. DOI: https://doi.org/10.1016/j.measurement.2018.05.068. URL: http://www.sciencedirect.com/science/article/pii/S0263224118304585.